UNIVERSITÀ DI PISA

INGEGNERIA DELLE TELECOMUNICAZIONI

Prompt-particle-events in ESA’s Envisat/MERIS and Sentinel-3/OLCI data: observations, analysis and recommendations.

Master Thesis

Francesco D'Amico
30/04/2015

Supervisors

Prof. Giovanni Corsini (University of Pisa)

Prof. Marco Diani (University ofPisa)

Prof. Jens Nieke (ESA/ESTEC)

Table of contents

Chapter 1 Introduction

1.1 Problem

Prompt-particle-events (PPEs) are high-energy particles, such as trapped protons or cosmic rays and may cause undesired noise in the signal read out from the Charge Coupled Device (CCD) in electro-optical instruments used for Earth Observation (EO). These radiation events may occur as noisy spikes during EO instrument testing on ground and during routine observation of the EO instrument in space. Noise spikes in instrument raw data resulting from PPE may therefore result in false signals and subsequently incorrect interpretation of EO data.

PPEs are frequently seen in CCD images and sometimes called in literature “cosmic ray” events. However, energetic particles are ions consisting mostly in high-energy protons and atomic nuclei such as (mainly) hydrogen, some helium, diminishing amount of carbon, oxygen and even a few atoms of iron and of heavier elements [1]. Cosmic rays are mainly originating from outside the solar system and a significant fraction of primary cosmic rays originate from the sun or from the supernovae of massive stars. Further, active galactic nuclei are probably also producing cosmic rays [1].

When referring to cosmic rays, it is important to notice that the term ”ray” is not appropriately describing the physical phenomenon, as cosmic rays were at first and wrongly thought to consist of mostly electromagnetic radiation. In scientific literature [1] high-energy particles with intrinsic mass are known as "cosmic rays”, and photons, which are quanta of electromagnetic radiation (and so have no intrinsic mass) are known by their common names, such as "gamma rays" or "X-rays", depending on the location in the electromagnetic spectrum. Cosmic rays consist of ordinary matter, which had undergone some extraordinary process to gain significantly in energy, such as shock waves expanding from supernovas. Once these particles collide with the Earth’s stratosphere, so-called secondary particles are produced. Secondary rays are comprised of 74% muons, 25% electrons and just 1% protons.

Another typical source of undesired noise events in CCDs are protons hitting similar as cosmic rays the CCD’s surface. In contrast, those protons are generated by the sun or trapped in the Van Allen belts. This kind of radiation is particularly strong over the south of the Atlantic sea, off the coast of Brazil. The area is known as the South Atlantic Anomaly

(SAA) and it is particularly rich in trapped energetic protons due to the Earth's inner Van Allen radiation belt coming closest to the Earth's surface.

The number of cosmic rays hitting the surface of a CCD varies with altitude, as observed from astronomers working at different observatories and altitudes [1]. As an example, Figure 1.1.1 shows the dark signal generated by the OMI (Ozone Monitoring Instrument) [2] CCD over the SAA with an exposure time of 136 seconds and a gain factor of 40. OMI is on board the NASA Aura satellite in a 709 km sun-synchronous orbit.

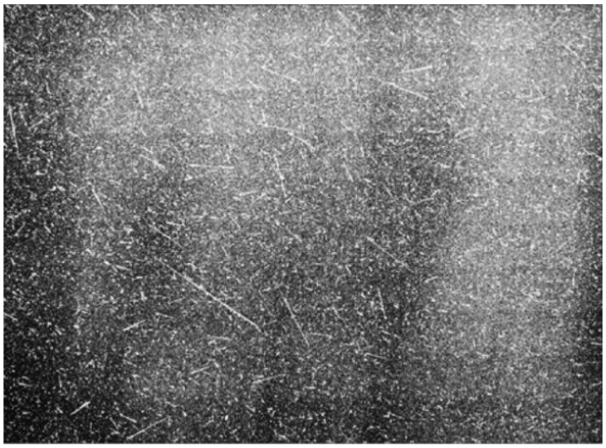

Figure 1.1.1. Dark signal measurements acquired by OMI CCD in the South Atlantic Anomaly [2].

Undesired effects of PPEs have also been observed for MERIS/OLCI type EO instruments. The Medium Resolution Imaging Spectrometer (MERIS) is a space-borne sensor primarily dedicated to observing oceanic biology and marine water quality through observations of water color, but also to atmospheric and land surface related processes [3]. MERIS flew from 2002 until 2012 on the ESA’s ENVISAT satellite (see Figure 1.1.2) in a sun-synchronous polar orbit of about 800 km altitude. The follow-up of MERIS is the Ocean and Land Color Imager (OLCI) to be flown on the ESA’s Sentinel-3 (S3) satellite and scheduled for launch in 2015.

Both imaging spectrometers are similar in design and making use of Charge-Coupled Devices (CCD) specifically developed for MERIS and re-manufactured for OLCI.

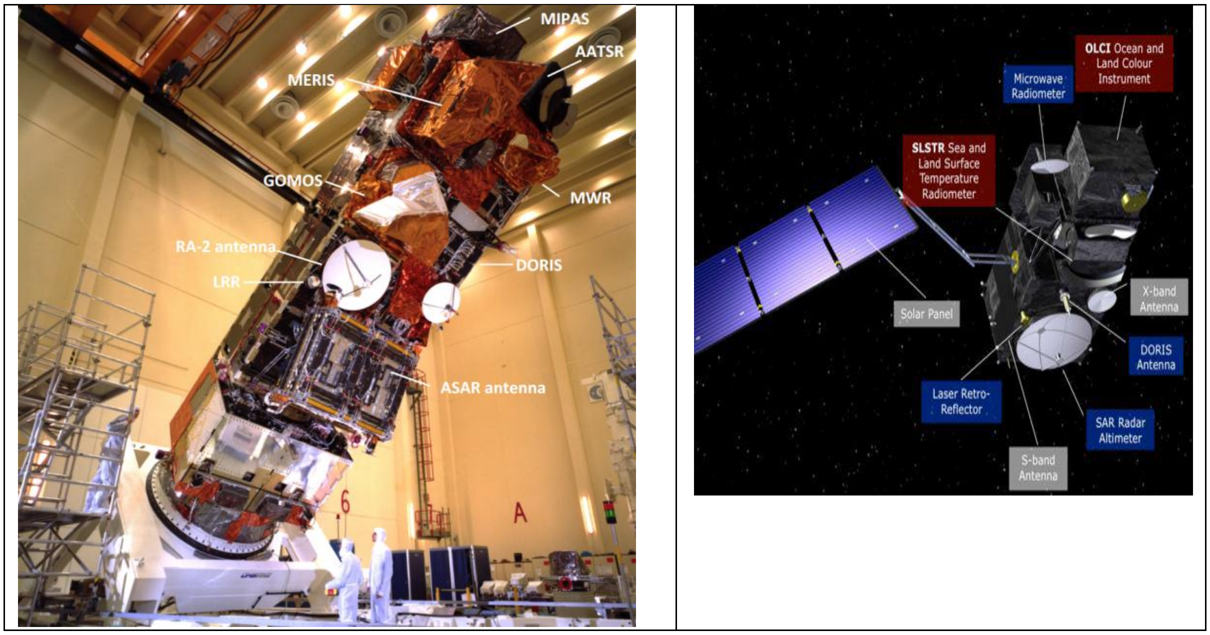

Figure 1.1.2. Left: ENVISAT Flight Model in test configuration at ESA-ESTEC. MERIS is accommodated on the upper panel of the satellite; right: artist's impression of Sentinel-3 spacecraft with optical payloads SLSTR and OLCI (red) and the topography package (blue).

During on-ground testing of MERIS and OLCI space instrumentation and during in-orbit operations of MERIS the occurrence of PPEs was observed. In the following, two significant cases are briefly described and will serve as introduction to the thesis to demonstrate how PPEs are affecting product quality and test results:

Example 1) One of the ENVISAT/MERIS algorithm serves to retrieve the MERIS maximum chlorophyll index (MCI). The algorithm makes use of the top-of-atmosphere (TOA) radiance peak at 709nm in water-leaving radiance and retrieves aquatic events such as 'red tides', i.e., spatial phenomena on the sea surface where large amount of aquatic vegetation is present forming an intense, visible, plankton bloom on the surface of the

Earth's ocean surface. Global MCI composite images, at a spatial resolution of 5 km, are produced daily from MERIS (daylight) passes of reduced resolution (RR) data. When looking at global composites and plankton bloom events it was found by Gower et al. [4] that specifically the Ocean areas collocated with the South Atlantic anomaly (SAA) were experiencing larger amounts of blooms (see Figure 1.1.3). Since these phenomena could not be validated with in-situ data Gower et al came to the sound assumption that cosmic rays may generate noise in MERIS CCDs.

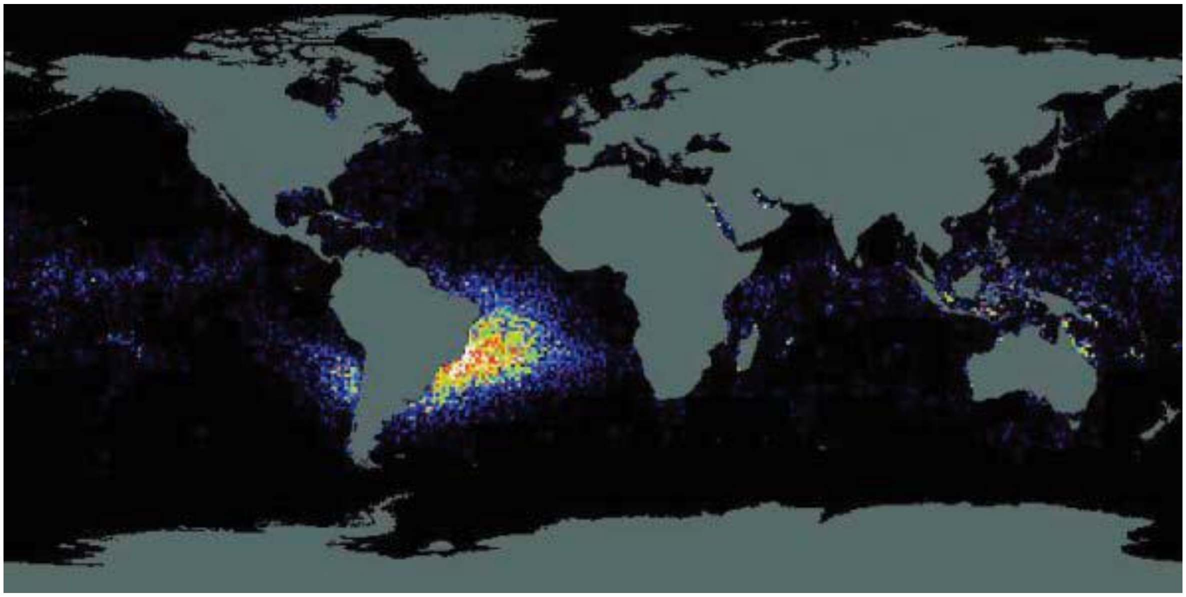

Figure 1.1.3. Global occurrence of false alarms observed with MERIS data applying the MCI algorithm showing peak values over the South Atlantic Anomaly [4].

Example 2) During ground darkness tests [5] of Sentinel-3/OLCI (Ocean and Land Color Instrument) at Thales Alenia Space France (TAS-F) the occurrence of some noise spikes (see Figure 1.1.3) was found. It was observed that these occurrences were neither time nor band correlated. Any influence from the Electronic Ground Support Equipment (EGSE), the Video Acquisition Module (VAM) and the Focal Plane Assembly (FPA) was excluded, as spikes were present directly at the CCD output. Hence, these occurrences were assumed to be related to cosmic rays hitting certain areas of the 2-dimensional CCD chip.

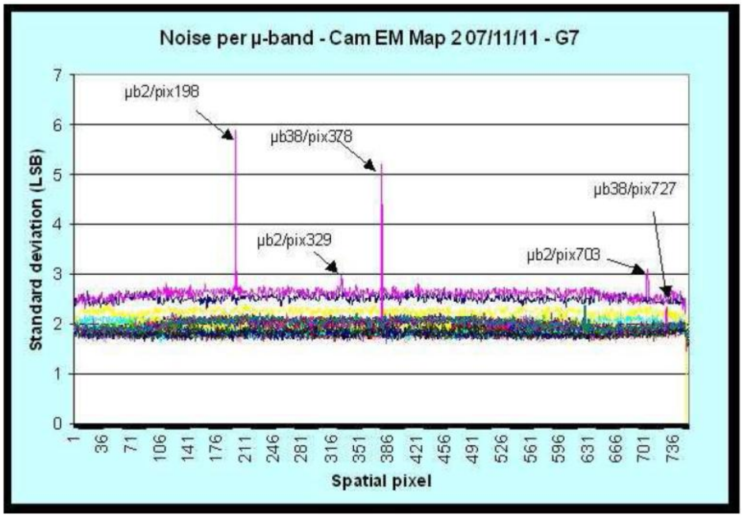

Figure 1.1.3. Spikes appearing in the FPA + VAM EM output dark signal affecting different µbands under test [5].

These two examples demonstrate very well, how prompt-particle-events (PPE) may generate noise in OLCI/MERIS type instruments. It is evident that the effect needs further assessment and in order to allow to quantify the risk of misinterpretation of end-user product.

In the scope of the thesis detailed observations and analyses of the occurrence of specific PPE-induced noise are performed by assessing quantitatively and qualitatively effected ENVISAT/MERIS Earth observation data and/or S3/OLCI on-ground test data. The thesis will also provide recommendations on further assessments and potential removal of the noise via post-processing of acquired data.

On the other side, it needs to be clarified that the thesis shall not be regarded as “astrophysical research”, e.g., to conclude of specific behavior or observations of cosmic rays with MERIS/OLCI. In the thesis, primary / secondary cosmic rays and trapped protons will be referred as ‘’prompt-particle events’’ (PPEs), “high energy particles” or simply ''cosmic rays''. A distinction between those events is not foreseen, since the result of these event result in all cases in the occurrence of specific noise, which needed to by assessed quantitatively and qualitatively for the improved use of Earth observation data.

1.2 Objectives

PPE-induced noise cause undesired spikes in the signal read out from the ENIVISAT MERIS CCD. Sentinel-3 instruments are likely to experience a similar noise since the same kind of CCD (supplier: E2V, Chelmsford, UK) is used in the OLCI detection chain[1].

The thesis is motivated by the following general research questions:

1) Would Sentinel-3 OLCI be more effected by PPE-induced noise because of its higher spatial resolution (Full Resolution also over ocean) and dynamic range (12 to 14 bits)?
2) What is a good method to detect the occurrences of PPE-induced noise in orbit?
3) What are the mitigation possibilities to reduce the PPE-induced noise in the data?

In order to find some answers to those research questions and, subsequently, studying the effect of PPE-induced noise, the following MERIS and OLCI data was made available by ESA:

- ENVISAT/MERIS data from the years 2003-2009 at three different processing levels, i.e., raw Level 0 (L0 RR) data, calibrated Level 1B (RR L1B) data and higher-level (Level 2, L2) data;
- Sentinel-3/OLCI Engineering and Flight Model test data from the year 2013 and 2014.

With the above research questions and the availability of specific data sets, it became necessary to first understand the working principle of the MERIS and OLCI instruments in a way to allow the development of dedicated routines for the data analysis.

---

[1] Whereas the E2V CCD25-20 was used for MERIS, OLCI instruments will make use of a slightly modified type of the 20er series, now called CCD55-20. For the analysis of PPE-induced noise the two CCD can be regarded as equal.

The overview about MERIS and OLCI working principle is provided in Chapter 2: "The space instrumentation".

In a first investigation, MERIS L0 RR data from Envisat commissioning phase (acquired when the shutter of the instrument was closed) were used to analyze the behavior of the dark signal and the impact that PPEs may have on it along one entire specific orbit. The occurrence probability of a PPE was investigated. This was carried out in two significant regions of the orbit: one located outside and the other inside the South Atlantic Anomaly (SAA).

The analysis approach and the results are documented in Chapter 3: "PPE-induced noise in ENVISAT-MERIS L0 data".

L0 RR data collected by MERIS over the SAA were analyzed to understand the potential worst-case impact on the CCD of energetic particles. In the SAA the cosmic radiation is stronger due to the weaker Earth's magnetic field (Figure 1.2.1), the CCD is exposed to a higher degree of noise and the prompt-particle events (PPEs) increase significantly [6].

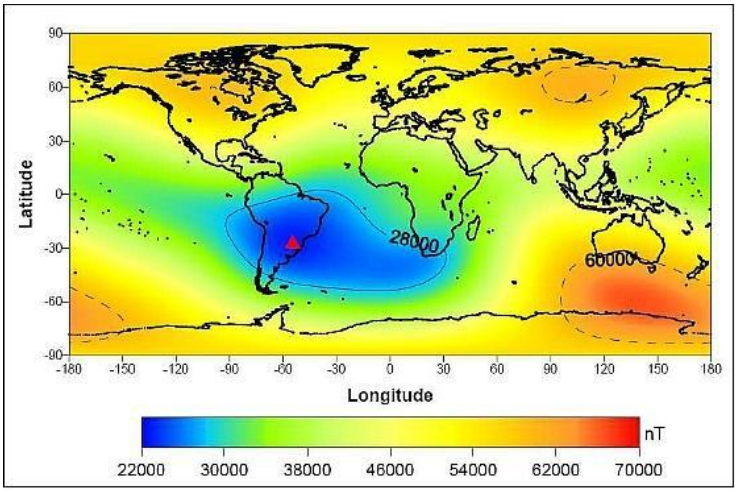

Figure 1.2.1. Earth's magnetic field measured in nano Tesla revealing its minimum in the south of the Atlantic Sea [7].

It was demonstrated how the occurrence of spikes are affecting the dark value of the CCD’s pixels of all MERIS spectral bands and the probability of such occurrence was estimated inside and outside the SAA.

Further, pixels located next to a corrupted pixel were investigated in order to understand if one strike on the CCD could affect also other consecutive pixels located around the impact location.

The effect of cosmic rays impact was also studied to determine how sensitive MERIS was and OLCI will be in terms of digital units: the difference between the mean value of corrupted pixels and the mean value of the dark signal was computed for two different data sets, one outside and the other inside the SAA. A model of probability density function approximating the occurrence LSB amplitude was searched.

Further, MERIS L0 data acquired when the instrument was set on operational mode were analyzed to determine an opportune algorithm through which detect noisy spikes due to cosmic rays in the smear band signal. In this way, it could be possible to study the trend of such perturbation over the duration of seven years.

The analysis approach and the results are documented in Chapter 4: “Detection of PPEs in the smear band during MERIS operational phase.”

Another objective was to investigate the effect of PPEs on one particular EO product. This was done by processing MERIS Top-Of-the-Atmosphere (TOA) radiance signal, i.e. L1B data, to obtain a Maximum Chlorophyll Index image of the selected swath. PPE noise may result in false alarms in retrieving chlorophyll (Figure 1.1.2) [8]. An opportune algorithm was tested to understand if some significantly anomalous pixels can be present and if there is a way to correct them.

The analysis approach and the results are documented in Chapter 5: “PPEs detection in Maximum Chlorophyll Index images.”

Finally, recent Sentinel-3/OLCI ground test data were inspected. The data were retrieved as dark signal for the five cameras and for three different gains used in the acquisition chain and to detect and quantify once more those pixels affected by spike noise on ground. Then, making use of a simplified performance model, the results from MERIS data in flight and OLCI on-ground test were used to predict the mean radiance error due to PPEs measured by Sentinel-3 OLCI.

The analysis approach and the results are documented in Chapter 6: "Assessment of PPEs during OLCI preflight testing and prediction of OLCI in-flight sensitivity".

All the results of the study and the recommendations for Sentinel-3/OLCI will be summarized in chapter 7*: "Conclusions".*

Chapter 2 The space instrumentation

2.1 MERIS and OLCI instrument concepts

OLCI and MERIS are both imaging spectrometers operating in the Visibile and Near Infrared regions of the electromagnetic spectrum. MERIS was one of the key instruments on board of ESA's Envisat satellite [9] while OLCI will be a key payload instrument of ESA's Sentinel-3 mission [10], as part of the European Commission's Copernicus programme [11]. Their goal is to provide a long-term collection and delivery of high-quality measurements of ocean color, both in open ocean and in coastal zones for retrieving geophysical parameters such as chlorophyll, dissolved organic matter and suspended solid matter concentrations. Other parameters of interest are indices that characterize the vegetation over land and some atmospheric parameters such as top pressure, aerosol optical thickness and water vapor columns contents.

Even though the physical structure and the functional block diagrams are very similar for both sensors, OLCI incorporates some important improvements to be mentioned. Thus, MERIS first and then OLCI will be separately described in the following.

2.1.1 MERIS

MERIS is the Medium spectral Resolution Imaging Spectrometer [12] operating in the solar reflective spectral range, from the Visible (VIS) up to the Near Infrared (NIR) spectrum. The instrument scanned the Earth's surface by the "push-broom" method using five identical cameras arranged in a fan shape configuration allowing a Field Of View (FOV) of 68.5 degrees (with 0.4º overlap between adjacent cameras) covering a swath of 1150 km (across track).

The linear frame-transfer CCDs provide spatial sampling in the across-track direction, while the satellite motion provides scanning in the along-track direction, see Figure 2.1.1.

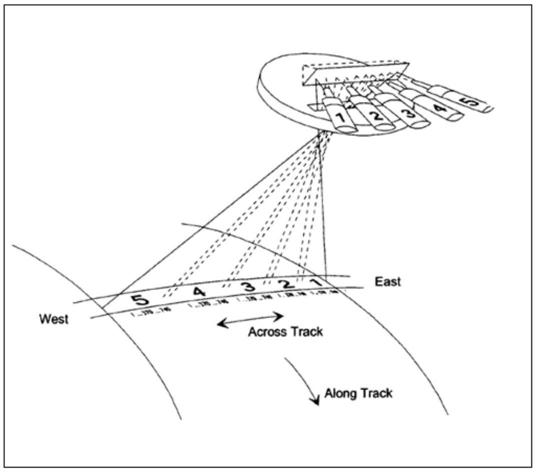

Figure 2.1.1. Swath subtended by the five cameras.

The scene is imaged simultaneously across the entire spectral range through a dispersion system, onto the CCD (Charged Coupled Device) array, as depicted in Figure 2.1.2.

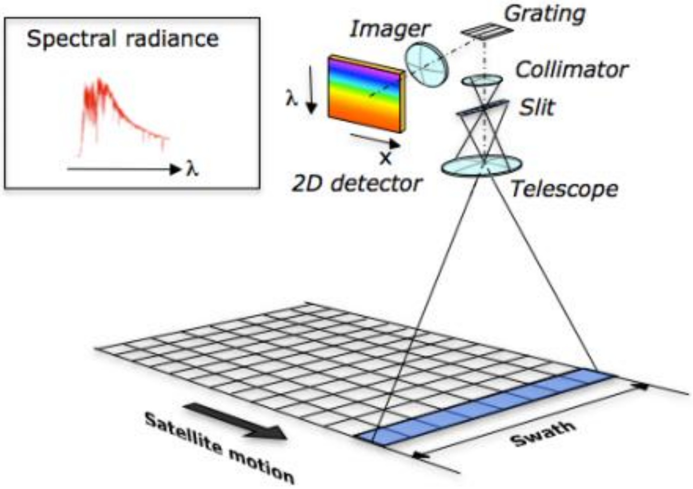

Figure 2.1.2. MERIS push-broom imaging spectrometer principle.

Of particular interest is the ability to automatically programme the position, width and gain of the 15 spectral bands in flight (see Figure 2.1.3), in the range from 390 nm up to 1040 nm.

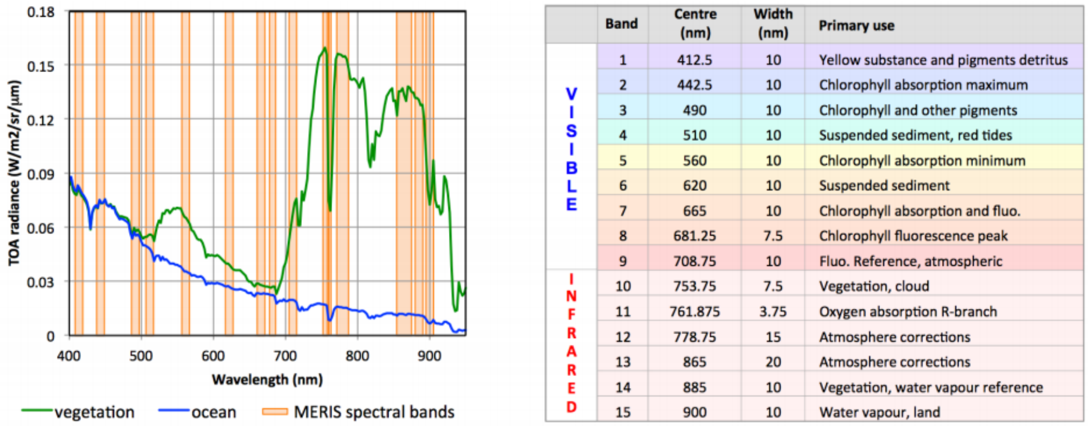

	Band	Centre (nm)	Width (nm)	Primary use
VISIBLE	1	412.5	10	Yellow substance and pigments detritus
	2	442.5	10	Chlorophyll absorption maximum
	3	490	10	Chlorophyll and other pigments
	4	510	10	Suspended sediment, red tides
	5	560	10	Chlorophyll absorption minimum
	6	620	10	Suspended sediment
	7	665	10	Chlorophyll absorption and fluo.
	8	681.25	7.5	Chlorophyll fluorescence peak
	9	708.75	10	Fluo. Reference, atmospheric
INFRARED	10	753.75	7.5	Vegetation, cloud
	11	761.875	3.75	Oxygen absorption R-branch
	12	778.75	15	Atmosphere corrections
	13	865	20	Atmosphere corrections
	14	885	10	Vegetation, water vapour reference
	15	900	10	Water vapour, land

Figure 2.1.3. The MERIS 15 nominal spectral bands overlaid on typical vegetation and ocean spectral TOA radiance.

MERIS is designed to acquire data whenever illumination conditions are suitable. Instrument operation is restricted to the day zone of the orbit, where the Sun's incidence angle is less than 80° at the sub-satellite point. Calibration is carried out, on average, once every two weeks, when the spacecraft flies over the south orbital pole and the Sun illuminates the instrument's on board calibration device. For the rest of the orbit, MERIS is in non-observation mode.

The Full Spatial Resolution (FR) is 300 m (at nadir), while this resolution is reduced to 1200 m (Reduced Resolution, RR). A RR pixel is generated by the combination of four adjacent samples across-track over four successive lines, as it was selected for all images taken over over open oceans, where a higher spatial resolution is not required.

The instrument is 1 m^3 in size, weights a little more than 200 kg and draws on average around 200 W. Figure 2.1.4 gives a representation of the instrument mechanical layout. The cameras view the Earth through five depolarizing windows. The modular design ensures high optical image quality over the large field of view. The output of each camera is processed separately in an analogue and digital processing unit.

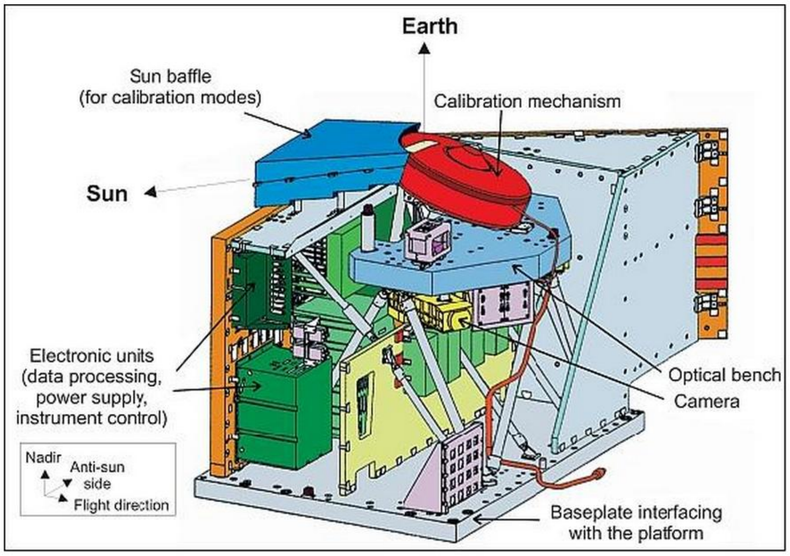

Figure 2.1.4. MERIS instrument mechanical layout.

The main instrument subsystems, see Figure 2.1.5, are:

- Calibration Mechanism (CM);
- Scrambling Window SubAssembly (SWSA);
- Camera Optics Subassembly (COSA);
- Focal Plane Assembly (FPA);
- Video Electronic Unit (VEU);
- Science Data Processing Subsystem (SDPSS);
- Instrument Control Unit (ICU);
- Power Distribution Unit (PDU);
- Digital Bus Unit (DBU);
- Thermal Control.

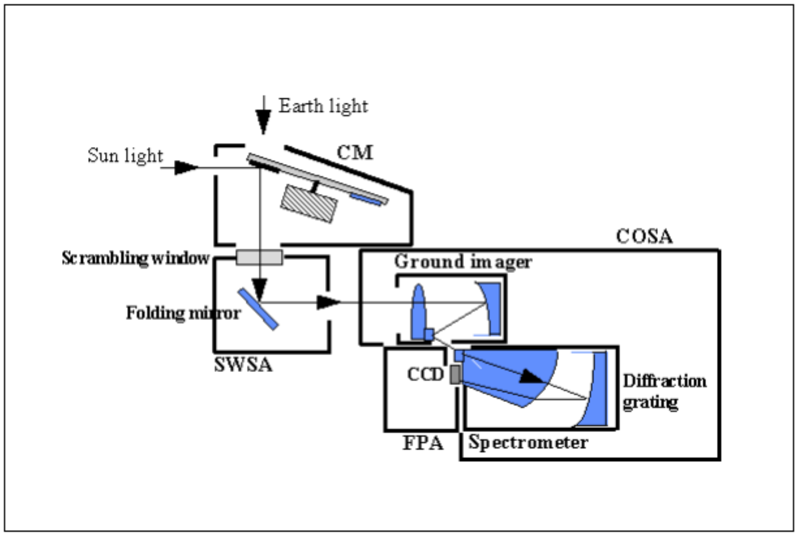

Figure 2.1.5. MERIS design configuration overview.

The optical bench supports the five COSA, the FPA, the SWA, five VAM containing the whole analogue imaging chain down to the ADC (Analogue to Digital Converter), the VEU managing all the instrument functions, the calibration assembly and the FPA.

The optical system assembly consists of five identical cameras mounted on a temperature controlled (20 ±1 C) optical bench. An off-axis catadioptric telescope images the Earth on the entrance slit of the spectrometer, which includes an off-axis concave holographic diffraction grating and a co-centric refractive corrector block. A second order absorption wedge filter is coated on the CCD window thickness across the device to match the wavelength diffracted by the spectrometer and to locally meet the condition of minimum reflection (thickness $\lambda/4$). This enabled to mitigate the optical ghosts generated by reflection between the CCD and its window over the entire spectral range (390 nm – 1040 nm).

Signals read out from the CCD pass through several on-board processing steps (see Figure 2.1.6) in order to achieve the required image quality. Analogue electronics perform pre-amplification of the signal, correlated double sampling and gain adjustment before digitization of the video signal on 12 bits. The signal amplification is done by selecting one of the 12 fixed gains defined in the range 1 to 3.75. The amplification gain is selected separately for each spectral band to minimize the noise contribution of the processing chain. Thus, the saturation level of any band can be optimized for the purposes of that band. For instance, a spectral band used only for ocean applications can saturate over clouds, leaving the full 12-bit digitization for the useful dynamic range of the oceanic signal. To ensure the stringent signal stability required along the orbit and between calibrations an offset control loop (OCL) has been implemented in the Video Electronic Unit (VEU). The OCL sets the output DN level for the first five dark pixel of every micro-band to the transition 9-10. This offset voltage is then clamped for all remaining pixels in this microband. It is possible to enable or to inhibit this offset. The VEU includes 6 video chains (5 nominal plus one in cold redundancy): 5 video chains are active at a given time, with one video chain associated to each CCD. These video chains are controlled by a sequencer (either nominal or redundant).

The digital output of the VEU is subsequently processed by the Digital Processing Unit (DPU) in three major steps: completion of spectral relaxation up to the required bandwidth, subtraction of the offset and correction for gain non-uniformity and reduction of the spatial resolution of the data to 1200 m for the global mission summation of four adjacent pixels across-track over four consecutive frames.

The DPU includes 6 digital processing chains, consisting of 5 nominal and one in cold redundancy, each being definitely connected to a VEU video chain. The offset and gain corrections are based on coefficients computed during the calibration sequences. These coefficients are stored on-board as well as being sent to the ground. The instrument design offers the flexibility to have these corrections applied either on board or on the ground. In the latter case, offset and gain correction are bypassed in the on board processing flow and performed on the ground. This latter solution has been selected for MERIS operations.

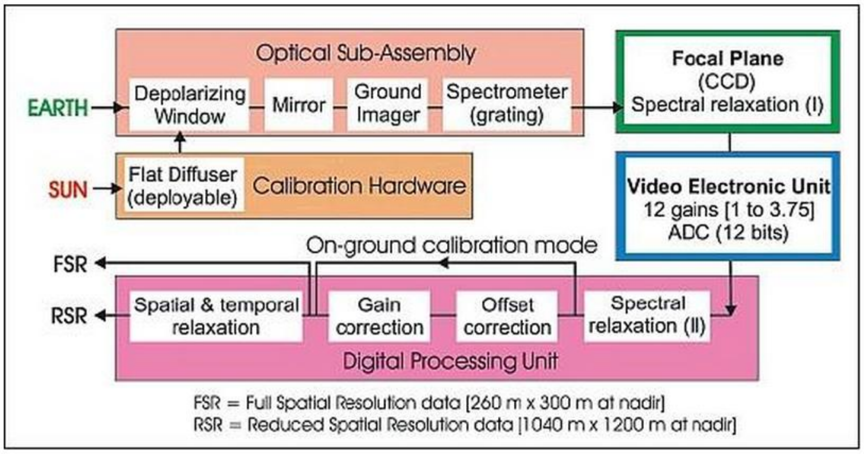

Figure 2.1.6. MERIS on-board signal processing flow block diagram.

2.1.2 OLCI

Sentinel-3/OLCI is a visible-near-infrared imaging spectrometer [13] that will provide climatological and environmental data continuity with previous ESA's Envisat/MERIS electro-optic sensor, after Envisat mission was formally declared ended by ESA on May 2012. The OLCI instrument is based on the opto-mechanical and imaging design of ENVISAT-MERIS.

In contrast to the MERIS instrument, OLCI employs an asymmetric swath with respect to the satellite ground-track in order to avoid direct solar reflection at sea surface (sun-glint). The amount of tilt is defined by the need to minimize the maximum Observation Zenith Angle (OZA) at the outer border of the swath and at the same time guaranteeing global coverage. Figure 6 shows the across-track tilt of the overall field of view of 12.6°, resulting in a maximum OZA slightly above 55 deg, see Figure 2.1.7.

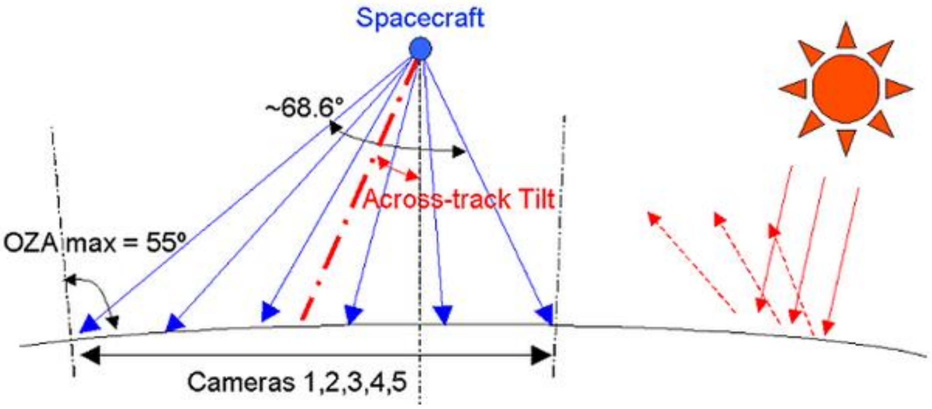

Figure 2.1.7. OLCI's 5 camera modules arranged in asymmetrical viewing geometry.

OLCI will observe the Earth with a Field of View (FOV) of more than 1200 km and an Instantaneous Field of View (IFOV) of 300 m over all earth surfaces that are illuminated by the sun. The data will be delivered in 21 spectral bands with a high Signal-to-Noise Ratio (SNR) to provide continuity to data products generated by the 15 MERIS spectral bands (see Table 2.1.1). Six additional spectral bands in the spectral range between 390 and 1040 nm provide the means for improved water constituent retrieval (@ 400 and 673.75 nm), atmospheric correction (@ 1020 nm) and improved parameter retrieval in the O2A-band (@ 760-775 nm).

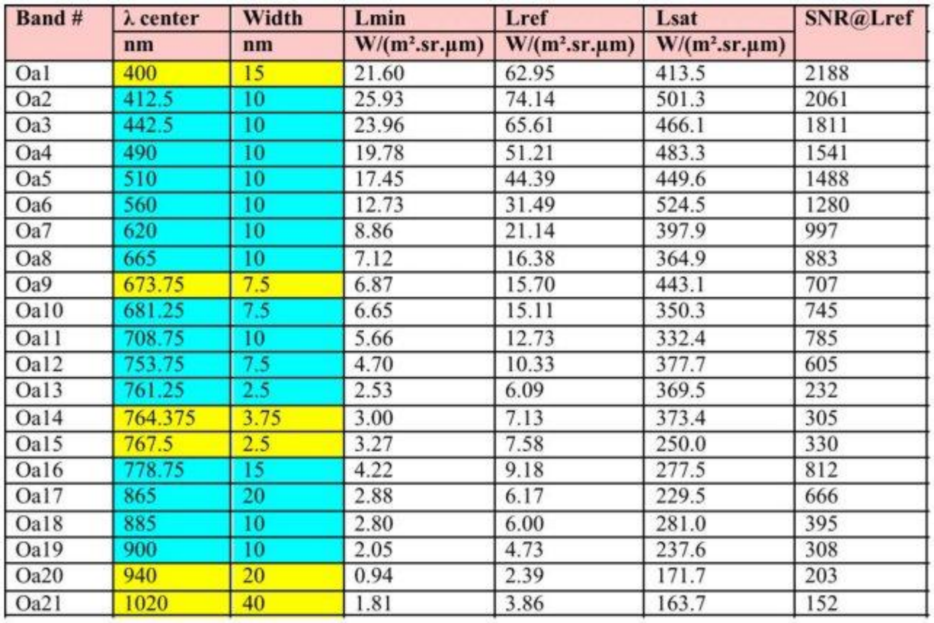

Band #	λ center	Width	Lmin	Lref	Lsat	SNR@Lref
	nm	nm	W/(m².sr.µm)	W/(m².sr.µm)	W/(m².sr.µm)	
Oa1	400	15	21.60	62.95	413.5	2188
Oa2	412.5	10	25.93	74.14	501.3	2061
Oa3	442.5	10	23.96	65.61	466.1	1811
Oa4	490	10	19.78	51.21	483.3	1541
Oa5	510	10	17.45	44.39	449.6	1488
Oa6	560	10	12.73	31.49	524.5	1280
Oa7	620	10	8.86	21.14	397.9	997
Oa8	665	10	7.12	16.38	364.9	883
Oa9	673.75	7.5	6.87	15.70	443.1	707
Oa10	681.25	7.5	6.65	15.11	350.3	745
Oa11	708.75	10	5.66	12.73	332.4	785
Oa12	753.75	7.5	4.70	10.33	377.7	605
Oa13	761.25	2.5	2.53	6.09	369.5	232
Oa14	764.375	3.75	3.00	7.13	373.4	305
Oa15	767.5	2.5	3.27	7.58	250.0	330
Oa16	778.75	15	4.22	9.18	277.5	812
Oa17	865	20	2.88	6.17	229.5	666
Oa18	885	10	2.80	6.00	281.0	395
Oa19	900	10	2.05	4.73	237.6	308
Oa20	940	20	0.94	2.39	171.7	203
Oa21	1020	40	1.81	3.86	163.7	152

Table 2.1.1. The 21 bands designed for OLCI. In blue, the bands shared by OLCI and MERIS.

Sentinel-3/OLCI incorporates the following significant improvements in respect to MERIS:

- more spectral bands (from 15 to 21);
- improved SNR through a 14-bit ADC;
- improved long-term radiometric stability with the extended diffuser calibration;
- mitigation of the sun-glint effect by tilting the cameras in westerly direction;
- Full Resolution for both land and ocean;
- improved instrument characterization including stray-light, camera overlap and calibration diffusers;
- improved coverage global ocean by 4 days, land by 3 days (15 days for MERIS);
- improved data delivery timeliness: 3 hours for L1B and L2 products;
- 100% overlap with the Sea and Land Surface Temperature Radiometer (SLSTR) swath, allowing the use of OLCI and SLSTR in synergy.

The basic configuration of the OLCI instrument includes an optical bench supporting the following components :

- five fan-arranged Camera Optical Sub Assemblies (COSA);
- five Focal Plane Assemblies (FPA), a Scrambling Window Assembly (SWA);
- five Video Acquisition Modules (VAM) containing the whole analogue imaging chain down to the digital conversion;
- OLCI Electronic Unit (OEU) managing all the instrument functions;
- calibration assembly allowing a radiometric and spectral calibration;
- heat pipe networks insuring the thermal control of the VAM;
- FPA and detector.

The optical layout of OLCI is sketched in Figure 2.1.8.

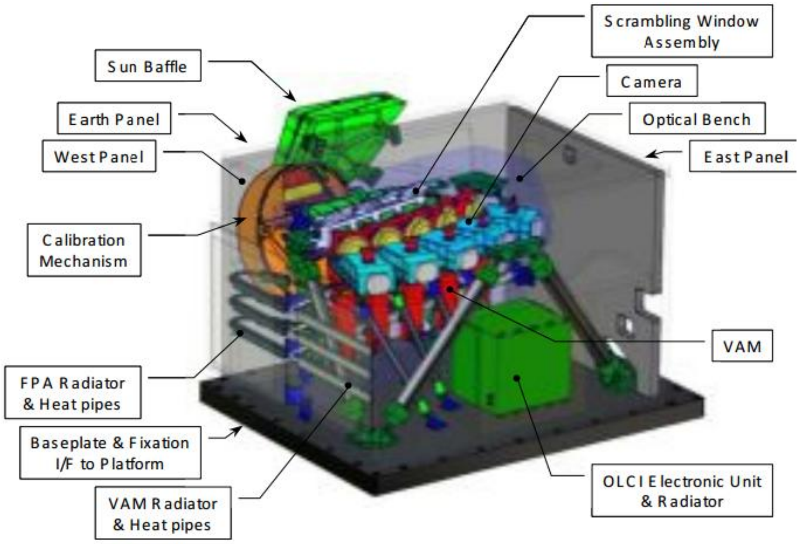

Figure 2.1.8. OLCI mechanical layout.

The Ground imager (housed within the COSA box) collects the light through the calibration mechanism (either from the Earth or the sun-illuminated diffusers) and the scrambling window. The collected light is focused onto the spectrometer entrance slit. The calibration mechanism allows a view of the earth surface or one of several on-board calibration targets through a slit window by rotating each target mounted on a calibration wheel into the instrument FoV. Then the spectrometer generates a dispersed image of the slit on a 2-dimensional Charged Coupled device (CCD) array: one dimension of the array is the spatial extension of the slit, and the other dimension the spectral dispersion of the slit image in the range between 390 and 1040 nm. The OLCI design configuration is shown in Figure 2.1.9.

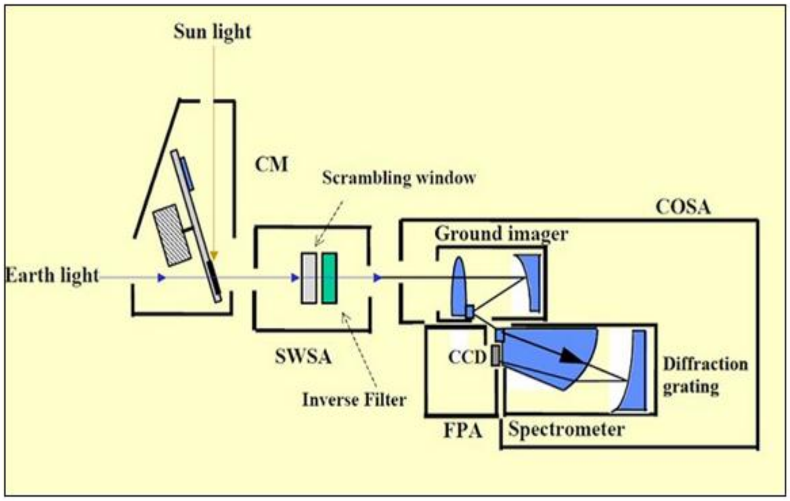

Figure 2.1.9. OLCI design configuration overview.

The imaging and calibration principles of OLCI can be depicted by the instrument functional block diagram as shown in Figure 2.1.10. The light coming from the Earth or the Sun enters the instrument through the Calibration Assembly (CA). The CA has several functional positions, either for calibration purposes (calibration hardware), e.g., with the sun, or for earth imaging through the earth diaphragm. Behind the CA, the 5 cameras are located covering the FOV in a fan shape configuration. Each camera consists of a SWU (Scrambling window units), a COSA, a FPA, a CCD and a respective VAM. The acquired data are then collected in the OEU always in High Resolution (HR) mode.

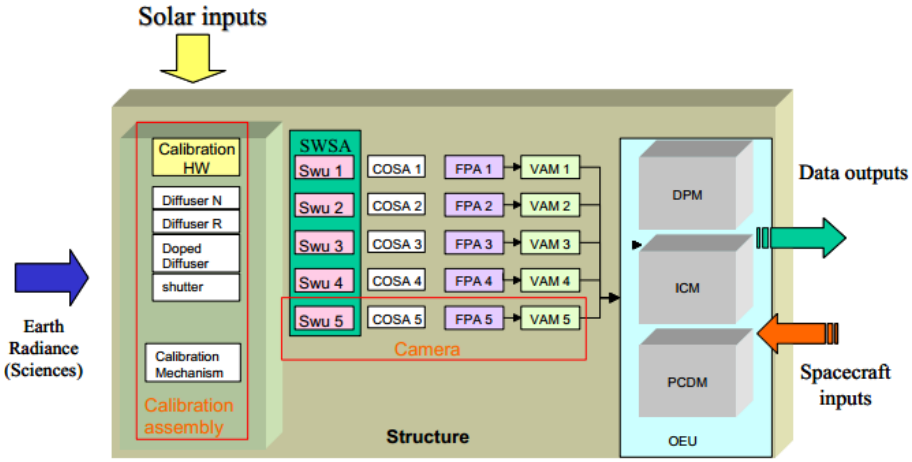

Figure 2.1.10. OLCI functional block diagram.

The OEU delivers 46 µbands (including a smear band collecting data during each frame transfer) in Raw Mode or 22 bands (including one smear band) in Imaging Mode (see Figure 2.1.11). The Raw Mode (46 µbands incl. smear band) will be used primarily during calibration phases, i.e., for both, via earth imaging or solar calibration. Since this mode needs to be managed with the satellite data resources, the mode will be operated only during specific calibration campaigns. The Nominal Mode, where 22 bands (incl. smear band) are transmitted after the spectral relaxation is enabled through the OEU combining 46 bands to 22.

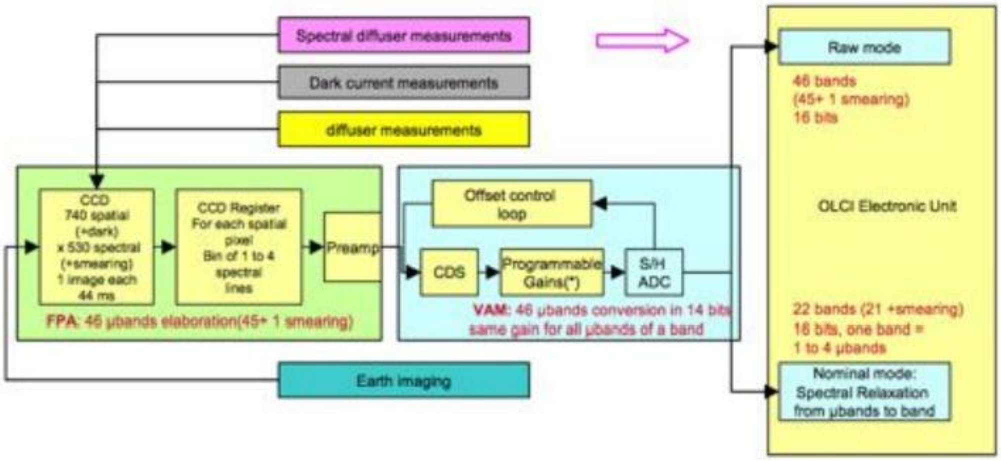

Figure 2.1.11. OLCI data processing block diagram.

2.2 MERIS and OLCI CCDs

Sentinel-3/OLCI and Envisat/MERIS detectors are frame-transfer charge coupled devices. They are all produced by the same company (E2V, Chelmsford, UK). OLCI's CCD (55-20) is a slightly updated version of MERIS CCD (25-20). Since both CCDs are of similar structure and operating principles and therefore equally effected by PPEs, the following paragraph will describe in detail just the MERIS CCDs.

The selected E2V CCD 25-20 [14] is thinned and back illuminated to avoid the absorption and reflection (mainly in the blue part of the spectrum) by the electrode structure located at the front face of the device and offer the required high responsivity in the blue region of the spectral range (see Figure 2.2.1). The CCD is composed of 780 (H) x 576 (V) x 2 elements, but only 740 x 520 elements are used as imaging area for the MERIS images. The detectors are thinned to 17 µm for improved detection efficiency at shorter wavelengths. An anti-reflective coating is applied along the spectral dimension to reduce the ghost images and improve the detection efficiency. The window, outside the Imaging Zone, is gold coated to optimize the thermal interfaces with the surrounding optics. The device is thermally controlled to better than 10 mC at a temperature of -22.5 C using Peltier coolers.

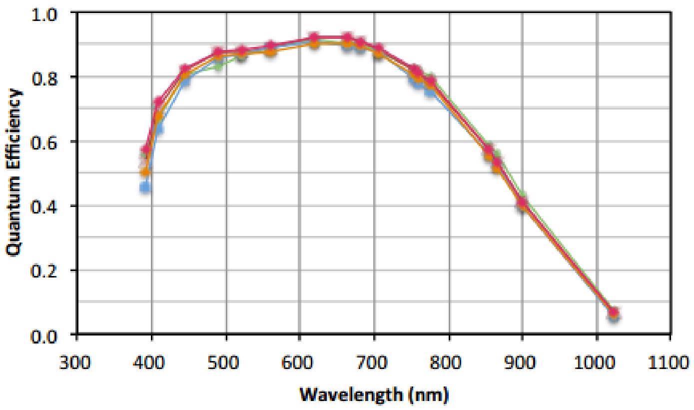

Figure 2.2.1. Quantum efficiency for the five MERIS CCDs.

Each detector element has a size of 22.5 µm x 22.5 µm corresponding to one pixel in the image data. Each line composed of 740 pixels corresponds to the spatial image of the entrance pupil at a given wavelength. Each column of 520 detector elements corresponds to the spectral image of a pixel at all wavelengths in the 390 nm to 1040 nm range (Figure 2.2.2). Consequently, each pixel in the image represents 260 m (spatial image) x 1.25 nm (spectral image).

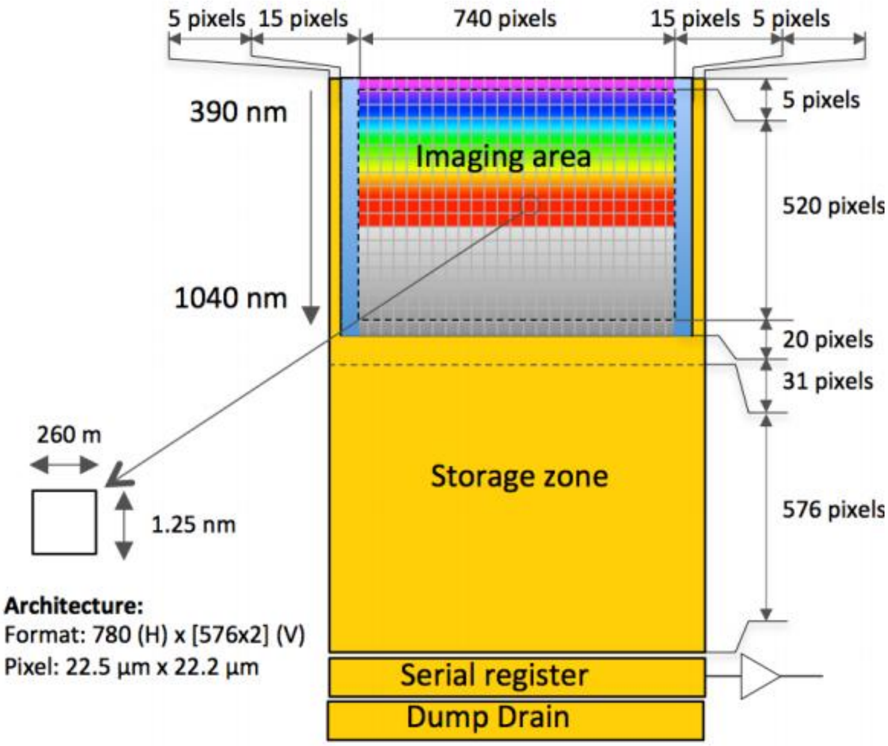

Figure 2.2.2. MERIS CCD structure.

The remaining detector elements of the CCD surrounding the image area are placed in the left and right sides and on top and bottom.

Ten transition pixels are placed on both sides for considering the possible misalignment with the mask which limits the imaging zone. Five more (shielded) pixels are located also on both sides are used to protect the dark pixel against charge contamination.

Five elementary spectral not shielded lines are located on the top and on the bottom of the imaging zone as a margin for possible shift of the spectrum with respect to the CCD. Ten spectral lines on the bottom of the imaging zone for possible misalignment with the mask limiting the imaging zone. Five additional spectral lines used to protect the smear band against charge contamination. Just under the imaging zone, 31 elementary spectral lines are reserved for the smear band, which is used to correct the smear effect (see Chapter 4).

The storage zone has a size of 576 x 780 pixels, to copy all previously described pixels.

The next Figure 2.2.3 explains the relations between elementary spectral lines, microbands and spectral bands. The constitution of spectral bands combining microbands is called spectral relaxation or spectral binning.

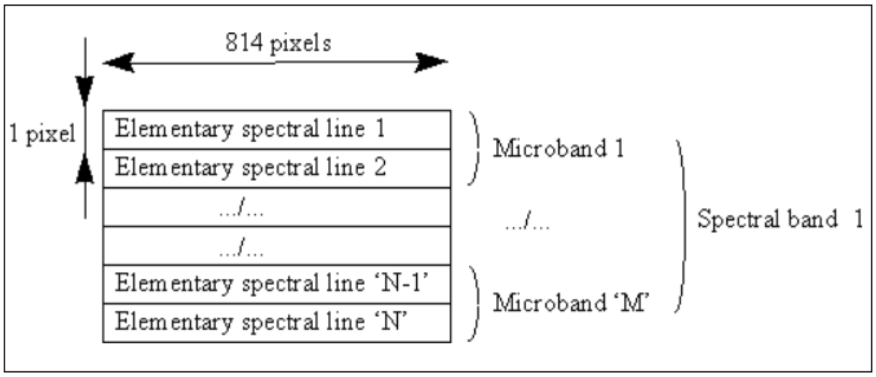

Figure 2.2.3. Example of spectral band formation.

The default values for MERIS spectral bands (the number of the last line in the spectral band, between 0 and 520), number of microbands in the spectral band, and number of elementary spectral lines per microband and the associated VEU (Video Electronic Unit) gains are given in Table 2.2.1. The smear band (16th spectral band) is not identified by any wavelength because it is not an observation band. The spectral band position is given by the number of the last elementary line in the band.

The CCD acquires data with an integration time of 42.7 ms during which each detector element collects a certain amount of electrical charge. Then the electrical charges are shifted within 1.3 ms to the storage zone, where they are protected from the incoming light by a shield. Then, depending on the choice of observation spectral band and alignment parameters, the shift register decides which elementary spectral lines have to be kept and which will be eliminated.

Every 44 ms, for each spectral band, an entire spatial line of the on ground swath is acquired and this process allows the formation of the image taking advantage of the motion of Envisat space craft over which the sensor is located.

MERIS BAND NUMBER	VEU GAIN	NUMBER OF MICROBANDS	NUMBER OF LINES PER MICROBAND	TOTAL NUMBER OF SPECTRAL LINES	NUMBER OF LAST LINE IN THE BAND
1	1.25	2	4	8	22
2	1	2	4	8	46
3	1	2	4	8	84
4	1	2	4	8	100
5	1.75	4	2	8	140
6	1.5	4	2	8	188
7	1.5	4	2	8	224
8	1	2	3	6	236
9	1.75	4	2	8	256
10	1.25	2	3	6	294
11	1.25	1	3	3	297
12	1	3	4	12	314
13	1.75	4	4	16	384
14	1.75	1	8	8	404
15	1	1	8	8	412
16 (Smear)	3.75	1	31	31	520

Table 2.2.1. Spectral band default values (during Envisat commissioning phase).

The VEU converts the analogue signal into a 12 bit digital signal (in normal operations MERIS transmits the data to ground on 16 bits) using a sample-and-hold circuit with 12 gain levels selectable per microband. Each camera has a dedicated image processing board and the gain settings may not be the same across all boards. At each frame, bands are computed by the on-board summation of the appropriate number of microbands (spectral relaxation). The data can be averaged by binning four adjacent spatial pixels (across track) from four consecutive frames (along track) creating a Reduced Resolution (RR) pixel, as it happens when Envisat flies over oceans.

Chapter 3 PPE-induced noise in ENVISAT-MERIS L0 data.

3.1 Data analysis

A direct way to investigate noisy spikes due to cosmic rays is analyzing MERIS Level 0 Reduced Resolution data taken during the Envisat commissioning phase [15].

After the launch of Envisat, a six months commissioning phase was carried out. This first period was dedicated to functional and characterization tests, in-flight calibration of the instruments and to the first validation of Envisat products before releasing the data to the user community.

For one test, the MERIS was programmed in the following way: The see Figure 3.1.1, The rotation disk within the Calibration Mechanism (CM) is rotated so that the shutter is closing the instrument and no light is getting in the instrument. Therefore, the signal red out at the CCD output and after the processing chain should theoretically just be related to the dark current flowing through photosensitive devices even when no photons are hitting the detector. Physically, dark current is due to the random generation of electrons and holes within the junction region of the device that are then swept by the electric field.

The spikes will appear because the dark signal level is very low compared to the noisy peaks and when a cosmic ray hits the photodetectors, this results in a peak in the measured signal.

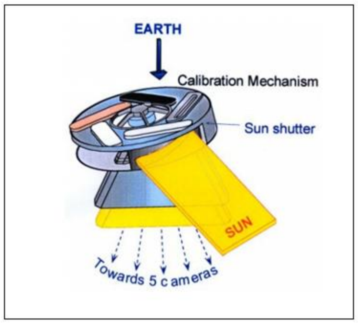

Figure 3.1.1. MERIS Calibration Mechanism with its rotation wheel occupying three calibration targets, the shutter and Earth-view diaphragm.

The phenomenon of noisy spikes (later referred as occurrences) in the signal acquired by the five camera modules was characterized from the statistical point of view along the entire absolute Envisat descendent orbit number 292. The choice of this orbit was done because the satellite flies over the South Atlantic Anomaly (SAA) and MERIS is exposed to a significantly higher degree of cosmic radiation.

The mean LSB value of the dark signal and its standard deviation computed in the first portion of the orbit (outside the SAA) and in the SAA will clearly point out the different impact of cosmic rays on the CCDs in the two considered regions.

The number of occurrences along the orbit will be measured selecting an opportune threshold.

The detected noisy spikes will also indicate the sensitivity of the CCD pixels in terms of LSBs in respect to the radiation.

Afterwards, the effect of the impact on one CCD element was investigated in order to understand if the dark value of adjacent pixels (located along the same CCD line) and/or pixels located in the neighboring bands is also affected.

The data file inspected is the following:

- *MER_RR__0PNPDK20020321_113429_000026211002_02698_00292_0044.N1*.

The file refers to Envisat descendent absolute orbit number 292 (see Figure 3.1.2); sensing start: 21st March 2002, 11:34:29.538938; sensing stop: 21st March 2002, 12:18:10.679412; start latitude: +79.635303 deg; start longitude: +31.304158 deg; stop latitude: -70.433999 deg; stop longitude: -59.464911 deg.

The L0 data file contains Reduced Resolution Level 0 data for all the 5 cameras and 16 bands (15 observation bands plus the smear one). One pixel corresponds to a ground surface of 1.040 km (H) × 1.160 km (V). Each line is made of 185 RR pixels per camera. Camera number 1 images the eastern part of the on-ground swath and pixel number 1 is on the western side of the on-ground track. The total number of lines over the entire descendent orbit is 14809.

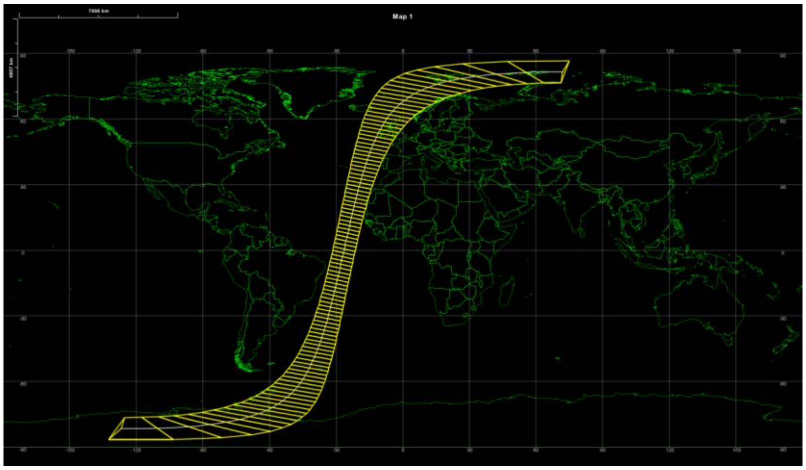

Figure 3.1.2. Descending absolute orbit number 292 reproduced using Esov software showing MERIS swath.

The boundaries of the SAA vary with altitude above the Earth. At an altitude of 500 km, the SAA ranges between -90 and +40 degrees in longitude and -50 to 0 degrees in latitude [10], see Figure 3.1.3. In this region, the extent of the SAA increases with increasing altitude (Envisat and Sentinel-3 altitude is around 800 km). The central latitude of the SAA is approximately at -25 degrees of latitude corresponding roughly to line number 10000 of the selected orbit.

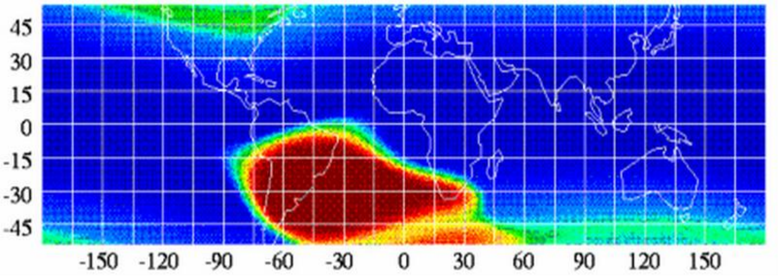

Figure 3.1.3. Map of the SAA at an altitude of ~ 560 km. The map was produced by ROSAT by monitoring the presence of charged particles. The dark red area shows the extent of the SAA. The green to yellow to orange areas show Earth's particle belts [7].

3.2 Dark signal first order statistics

The behavior of the dark signal for two different MERIS bands (band number 2 and smear band) is shown, as an example , in Figures 3.2.1 and 3.2.2 for the first spatial pixel of camera 5 (the one imaging the western part of the swath) for two different parts of the orbit (the first part goes from line 1 to line 4000 and the second one from 8000 to 12000, over the SAA).

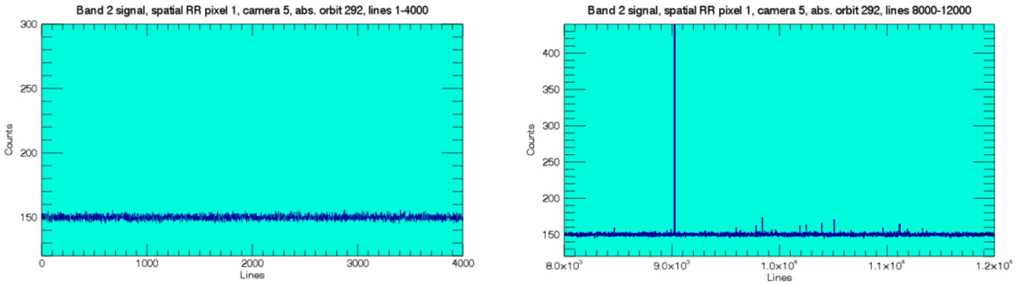

Figure 3.2.1*. RR dark signal acquired along absolute orbit 292 by the first spatial pixel of camera 5, spectral band 2, lines 1-4000 (on the left) and over the SAA, lines 8000-12000*.

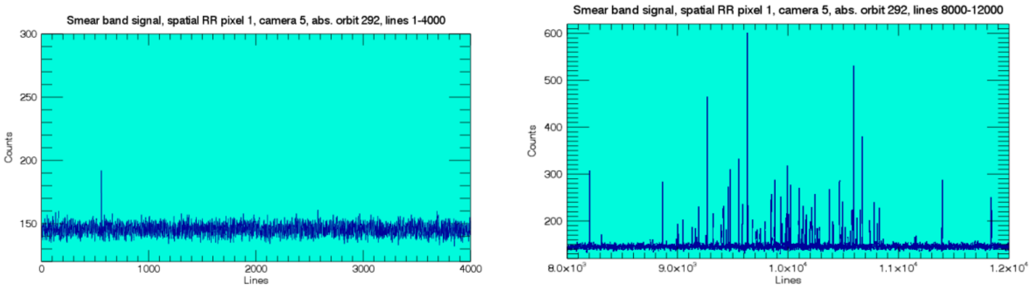

Figure 3.2.2*. RR dark signal acquired along absolute orbit 292 by the first spatial pixel of camera 5, smear band, lines 1-4000 (on the left) and over the SAA, lines 8000-12000*.

In the following pictures 3.2.5-3.2.20, MERIS dark signal is plotted for camera 5 (185 RR across-track pixels) along all the descendent orbit (14809 lines), for the 16 bands, to illustrate how the spike noise occurs mainly and strongly when Envisat flies over the SAA.

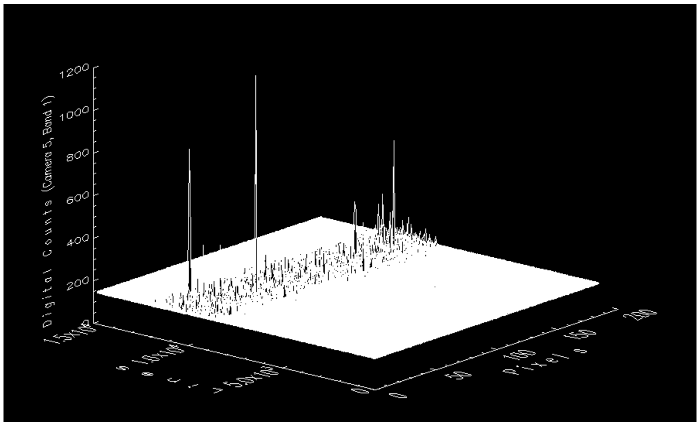

Figure 3.2.3. *MERIS dark signal depicted along all the descendent orbit (14809 lines)*

for camera 5 (185 RR pixels), band 1.

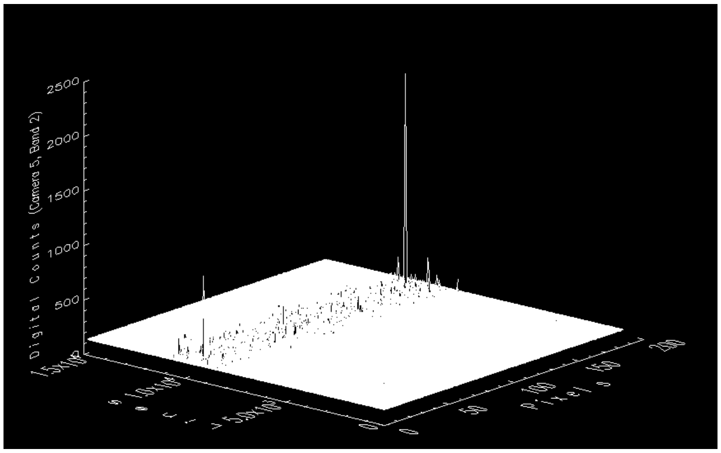

Figure 3.2.4. *MERIS dark signal depicted along all the descendent orbit (14809 lines)*

for camera 5 (185 RR pixels), band 2.

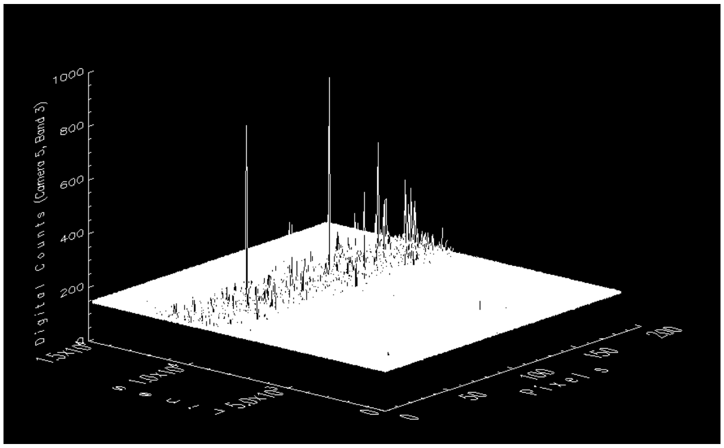

Figure 3.2.5. *MERIS dark signal depicted along all the descendent orbit (14809 lines) for camera 5 (185 RR pixels), band 3.*

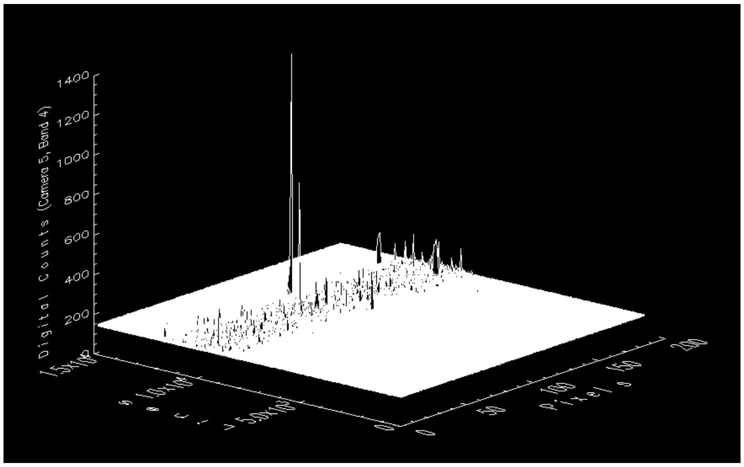

Figure 3.2.6. *MERIS dark signal depicted along all the descendent orbit (14809 lines) for camera 5 (185 RR pixels), band 4.*

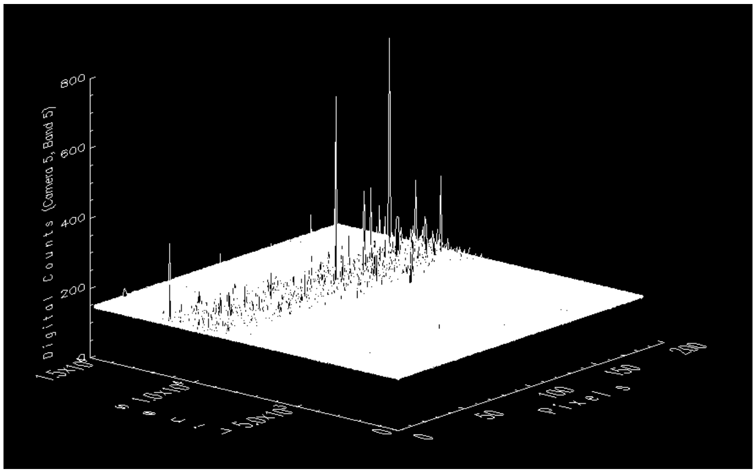

Figure 3.2.7. *MERIS dark signal depicted along all the descendent orbit (14809 lines)*

for camera 5 (185 RR pixels), band 5.

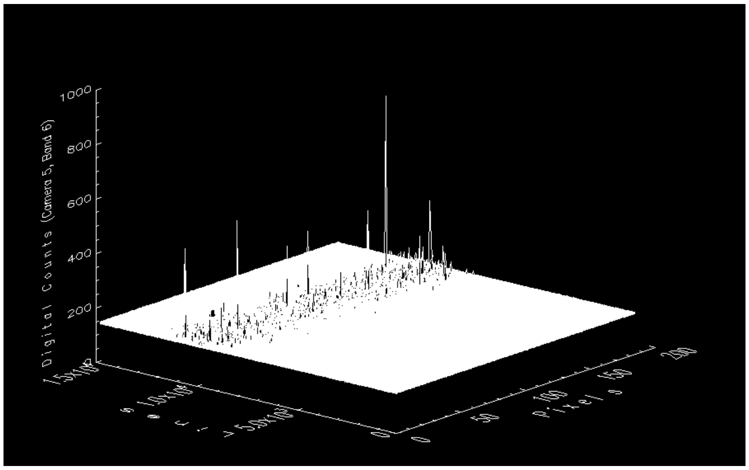

Figure 3.2.8. *MERIS dark signal depicted along all the descendent orbit (14809 lines) for camera 5 (185 RR pixels), band 6.*

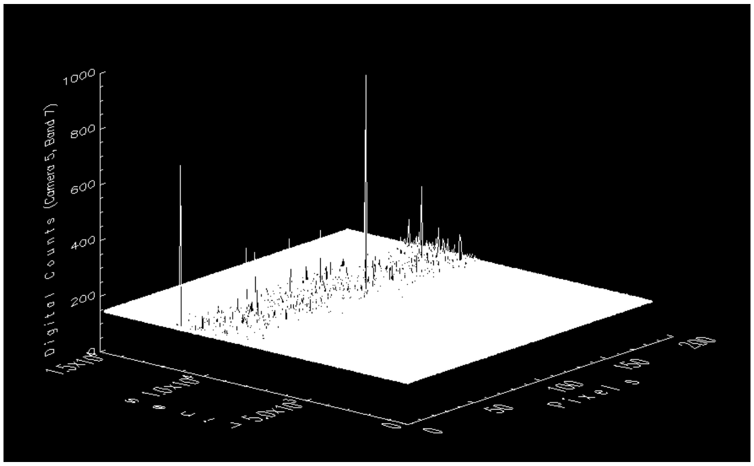

Figure 3.2.9. *MERIS dark signal depicted along all the descendent orbit (14809 lines) for camera 5 (185 RR pixels), band 7.*

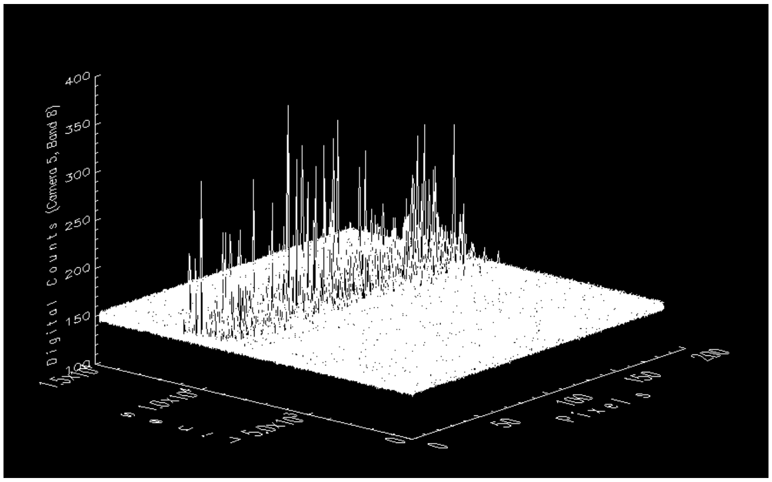

Figure 3.2.10. *MERIS dark signal depicted along all the descendent orbit (14809 lines) for camera 5 (185 RR pixels), band 8.*

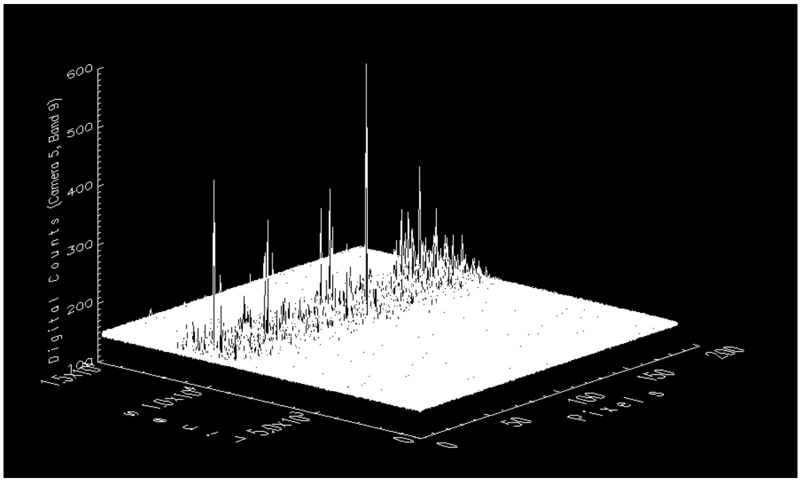

Figure 3.2.11*. MERIS dark signal depicted along all the descendent orbit (14809 lines) for camera 5 (185 RR pixels), band 9.*

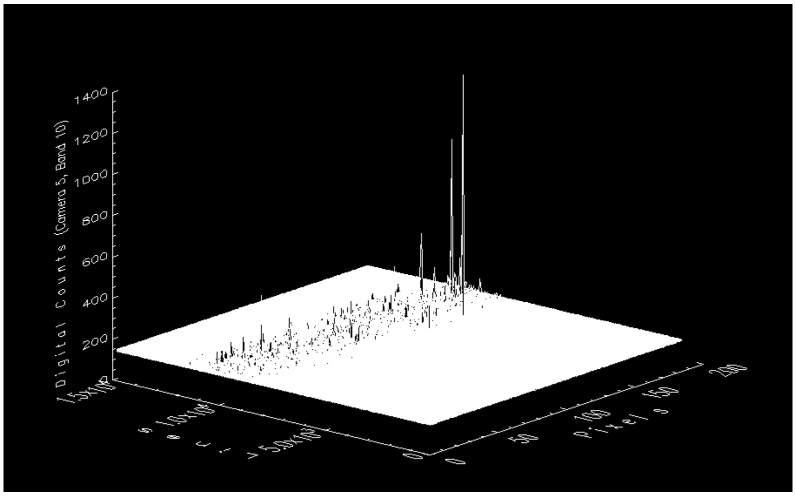

Figure 3.2.12*. MERIS dark signal depicted along all the descendent orbit (14809 lines) for camera 5 (185 RR pixels), band 10.*

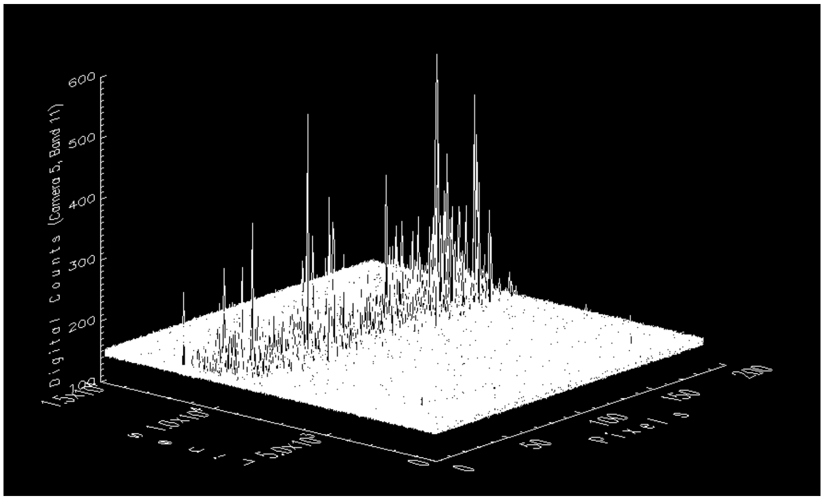

Figure 3.2.13. *MERIS dark signal depicted along all the descendent orbit (14809 lines) for camera 5 (185 RR pixels), band 11.*

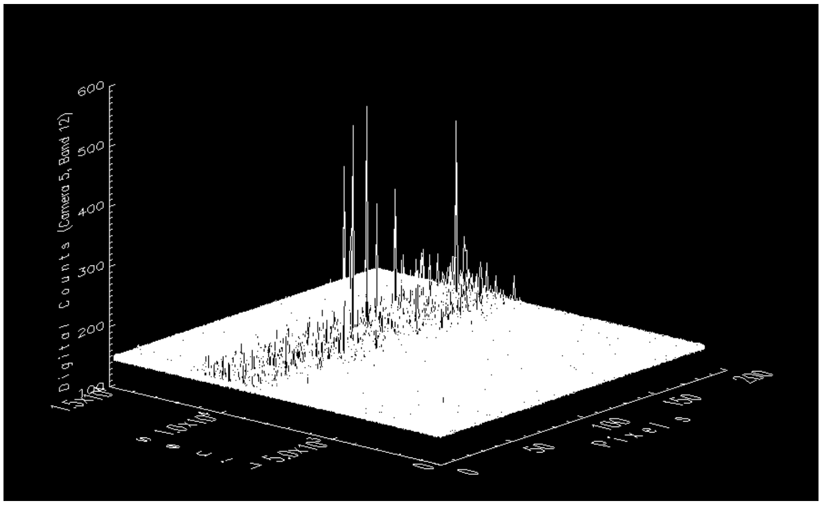

Figure 3.2.14. *MERIS dark signal depicted along all the descendent orbit (14809 lines) for camera 5 (185 RR pixels), band 12.*

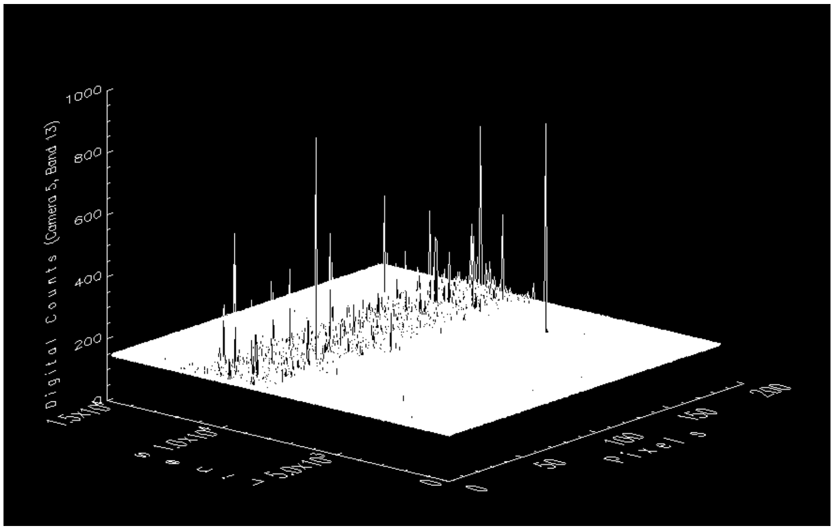

Figure 3.2.15. *MERIS dark signal depicted along all the descendent orbit (14809 lines) for camera 5 (185 RR pixels), band 13.*

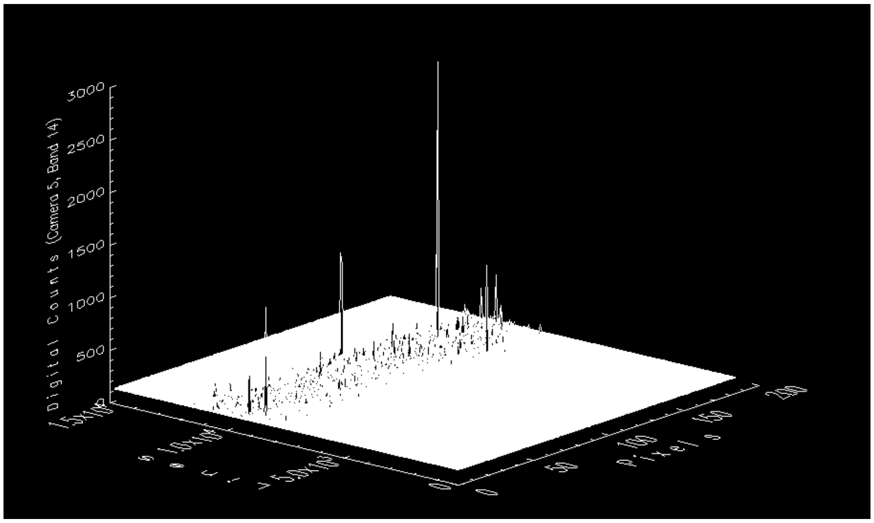

Figure 3.2.16. *MERIS dark signal depicted along all the descendent orbit (14809 lines) for camera 5 (185 RR pixels), band 14.*

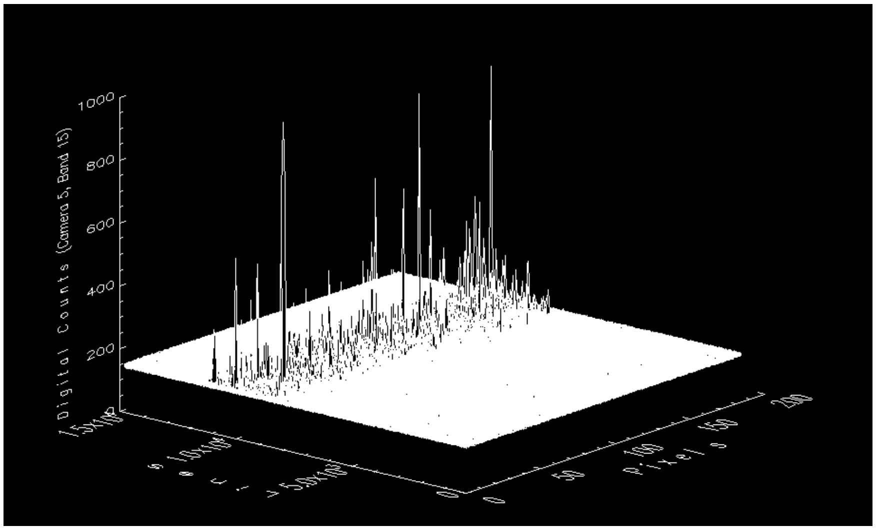

Figure 3.2.17. *MERIS dark signal depicted along all the descendent orbit (14809 lines) for camera 5 (185 RR pixels), band 15.*

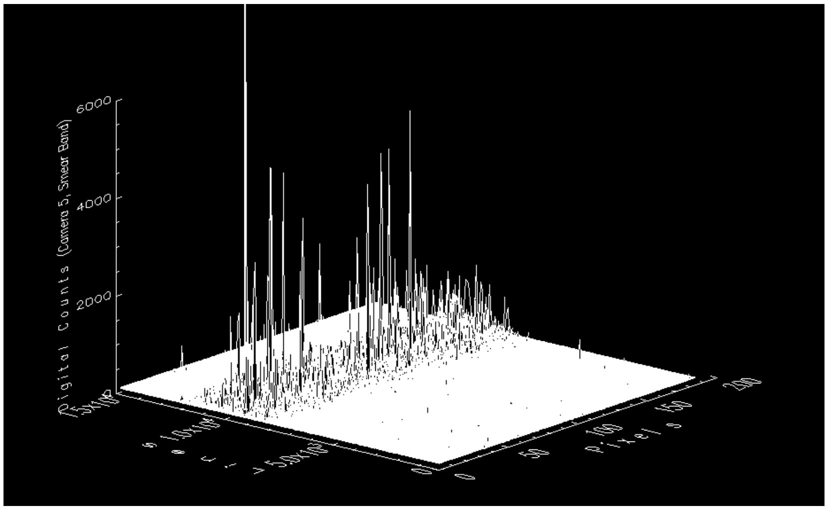

Figure 3.2.18. *MERIS dark signal depicted along all the descendent orbit (14809 lines) for camera 5 (185 RR pixels), smear band.*

From a first rough inspection it is evident that the smear band is the most affected by the noisy radiation and the spikes appear concentrated around line number 1.0 x 10^4 (i.e., the center of the SAA), as expected.

Before computing the statistics for the dark signal, some dedicated features of the CCD pixel must not be taken into account: For example the occurrences of “hot pixels” which are CCD pixels characterized by anomalous higher dark current values. This kind of dark signal non uniformity (DSNU) reveals a “fixed pattern noise” (FPN) which may arise from electronic sources (other than thermal generation of dark current) such as clock breakthrough or offset variations in the amplifiers [16]. The pattern appears along spatial lines (along-track, being MERIS a pushbroom sensor).

In order to verify if a pixel was affected by this defect, for all bands and for all cameras, the mean values and the standard deviations were computed for all the 185 pixels over their respective lines. Pixels with a mean value along the all line greater than 155 (the average of 15 mean values of the observation bands is approximately 152 outside the SAA, as later illustrated) and with a standard deviation smaller than 2 (the average of the 15 standard deviations is approx. 2.7, outside the SAA) were considered pixels with defects due to FPN. The choice of a smaller standard deviation can be explained thinking about an almost constant defective value that the pixel shows all along the lines.

In the case of MERIS, only one *hot pixel* was detected. This is the 93rd pixel of camera number 3, band 8.

A comparison with the pre-launch characterization data validated this observation . The document [17] refers to on ground MERIS tests and regards Full Resolution pixels. Six FR pixels were considered defective. After the FR-to-RR on board processing, the three pixels with defect (pix. 757 @ 927.5 nm, pix. 965 @ 592.5 nm and pix. 3199 @ 537.5 nm) are not detectable any more, while the other three pixels (pix. 1850 @ 677.5 nm, pix. 1850 @ 682.5 nm and pix. 1851 @ 682.5 nm) together combined (in pix. 93, camera 3, band 8) are still detectable.

The behavior of the pixel in question is illustrated in the next Figures 3.2.19 and 3.2.20 (the first figure displays the dark signal image over the entire orbit and the second displays a surface plot to get the feeling of the values assumed by all the 185 pixels of camera 3 over the first 1000 lines of the orbit) .

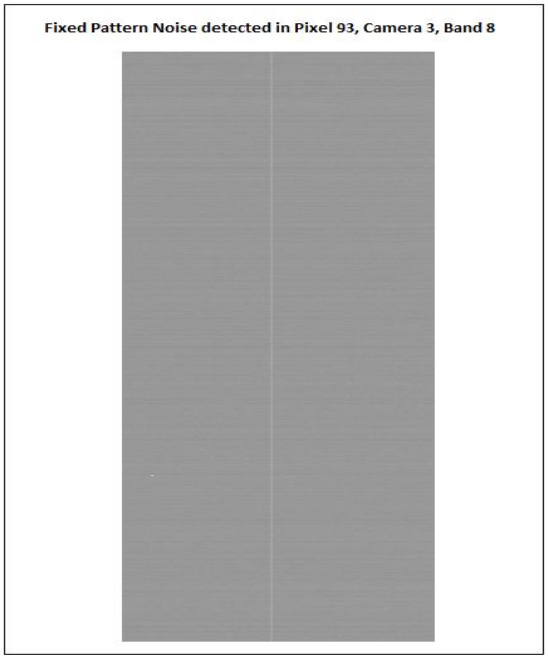

Figure 3.2.19. Dark signal grey-scale image of the entire descendent orbit # 292 (14809 lines) showing the Fixed Pattern Noise detected for pixel 93, camera 3, band 8.

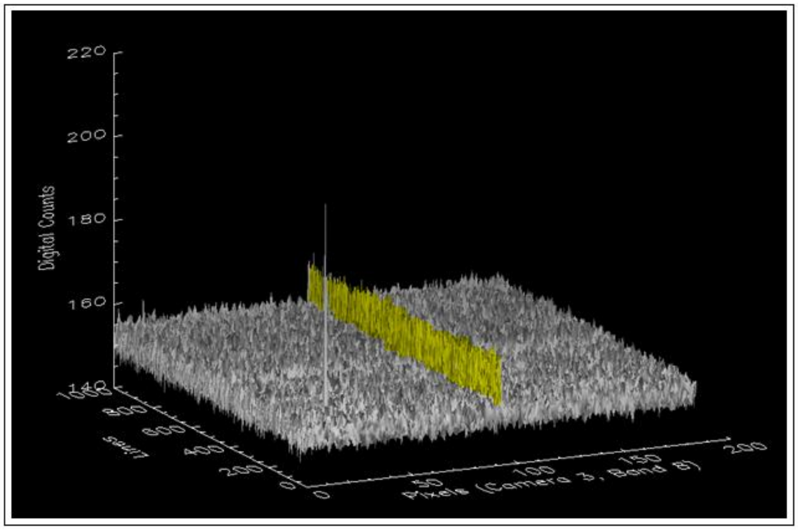

Figure 3.2.20. Dark signal related to the first 1000 lines of absolute orbit 292, revealing the defect (in yellow) affecting pixel 93, Camera 3, Band 8. In the forefront on the left side a cosmic ray is clearly distinguishable.

In order to define what an occurrence is, the first order statistical parameters were calculated per each band, excluding the hot pixel previously detected. making use of the pixel values from the first 7000 lines of the descending orbit. In this way, the data are not strongly affected by the noisy radiation belonging to cosmic rays

The following Tables 3.2.1-3.2.2 present the mean values and the standard deviations computed for the 16 MERIS bands, taking into account those pixel values from the first 7000 across-track lines of the descendent orbit, all located in the northern hemisphere to avoid the influence of the SAA. The pixel digital samples analyzed for this region are 6475000 per band (185 pixels X 5 cameras X 7000 lines).

Dark signal mean values Outside the SAA					
MERIS Band	Cam 1	Came 2	Cam 3	Cam 4	Cam 5
1	150.7	156.6	151.9	151.8	151.2
2	150.6	156.9	152.0	152.0	151.2
3	150.7	157.0	152.0	152.1	151.3
4	151.0	157.1	152.4	152.5	151.5
5	150.8	156.1	151.9	151.4	151.1
6	150.6	156.2	152.0	151.4	151.1
7	150.5	156.1	151.8	151.3	150.9
8	150.9	157.0	152.2	152.3	151.5
9	150.6	155.9	151.6	151.2	151.0
10	150.6	156.5	151.9	151.8	151.3
11	150.3	156.4	151.6	151.5	151.1
12	150.4	156.5	151.7	151.7	150.9
13	151.0	156.1	151.8	151.7	151.5
14	150.5	155.8	151.3	151.2	151.1
15	151.3	157.5	152.7	152.4	151.3
Smear	148.1	146.1	147.5	153.1	147.6

Table 3.2.1. Dark signal mean values for all bands,

outside the SAA.

Dark Standard Deviations Outside the SAA					
MERIS Band	Cam 1	Came 2	Cam 3	Cam 4	Cam 5
1	1.8	1.5	1.9	1.8	1.8
2	1.8	1.4	1.8	1.8	1.8
3	1.8	1.4	1.8	1.8	1.8
4	1.8	1.3	1.8	1.8	1.8
5	1.4	1.3	1.4	1.4	1.4
6	1.3	1.2	1.4	1.3	1.3
7	1.3	1.2	1.4	1.4	1.3
8	1.8	1.4	2.0	1.8	1.8
9	1.4	1.3	1.4	1.4	1.4
10	1.8	1.5	1.9	1.8	1.8
11	2.5	2.1	2.6	2.5	2.5
12	1.5	1.1	1.5	1.5	1.5
13	1.4	1.3	1.4	1.4	1.5
14	1.9	1.8	2.0	2.0	1.9
15	2.5	1.8	2.5	2.5	2.5
Smear	4.4	4.5	4.4	4.2	4.3

Table 3.2.2. Dark signal standard deviations for all bands,

outside the SAA.

Tables 3.2.3-3.2.4 illustrate the same statistics computed using 2000 lines collected by MERIS over the SAA, from line 9001 to line 11000, forming a data set of 1.85 x 10^6 samples per band.

Dark Signal Mean Values inside the SAA					
MERIS Band	Cam 1	Cam 2	Cam 3	Cam 4	Cam 5
1	150.9	156.6	152.1	152.1	151.6
2	150.8	156.9	152.3	152.2	151.4
3	150.8	156.9	152.4	152.3	151.5
4	151.2	157.1	152.7	152.6	151.8
5	150.9	156.0	152.0	151.6	151.4
6	150.8	156.2	152.0	151.7	151.2
7	150.7	156.1	151.9	151.5	151.1
8	151.1	156.9	152.5	152.5	151.7
9	150.8	155.9	151.7	151.4	151.2
10	150.6	156.3	151.9	152.0	151.5
11	150.5	156.3	151.6	151.7	151.2
12	150.5	156.4	152.0	151.9	151.3
13	151.3	156.1	152.0	152.0	151.7
14	150.8	155.8	151.6	151.6	151.4
15	151.6	157.5	153.0	152.8	151.7
Smear	151.3	148.9	149.9	155.2	150.3

Table 3.2.3. Dark signal mean values for all bands,

inside the SAA.

Dark Signal Standard Deviation inside the SAA					
MERIS Band	Cam 1	Cam 2	Cam3	Cam 4	Cam 5
1	4.7	3.6	4.3	4.2	3.4
2	2.9	3.7	2.9	3.0	3.7
3	3.3	2.9	3.2	2.92	3.0
4	3.5	2.5	3.4	2.7	3.1
5	2.6	2.3	2.3	2.3	2.4
6	2.0	2.0	2.0	2.0	2.2
7	2.2	4.6	2.0	2.2	2.2
8	2.6	2.2	2.6	3.7	2.3
9	3.0	2.1	2.3	2.2	2.1
10	3.0	2.5	4.8	3.0	3.1
11	3.8	3.5	3.4	3.9	3.4
12	2.2	2.4	2.2	2.2	2.2
13	2.8	3.0	2.4	3.9	3.0
14	3.5	3.3	3.8	4.0	5.2
15	4.4	4.4	4.0	4.3	4.6
sm	35.3	28.9	28.5	29.5	28.8

Table 3.2.4. Dark signal standard deviations for all bands, inside the SAA.

From this first analysis it comes out that the mean values and the standard deviations are very similar for the 15 observation bands outside the SAA, while the same parameters (principally the standard deviation) are substantially different for the smear band over the same region.

3.3 Occurrence probability

To detect the occurrences, a threshold $Th_b^{(c)}$ was chosen (subscript b=1, 2,…,16 indicates the band and c = 1, …,5 the camera) for each band and camera depending on the respective mean value and standard deviation computed outside the SAA for the first 7000 lines of the orbit. The threshold was defined as follows:

$$Th_b^{(c)} = \mu_b^{(c)} + 5\ \sigma_b^{(c)}\ ,$$

where $\mu_b^{(c)}$ and $\sigma_b^{(c)}$ respectively stand for the mean value and the standard deviation of band b and camera c.

The factor 5 multiplying $\sigma_b^{(c)}$ in the previous equation was chosen to build up a threshold value exceeding the mean (outside the SAA) by a quantity around the 10 percent.

Every dark level sample which exceeds the threshold was considered as occurrence. Not every occurrence may be related to a cosmic ray impact on the related CCD element, because one hit can cause more than one occurrence in the adjacent pixels, as will be later demonstrated.

The next Figures 3.3.1-3.3.8 show the relative frequency of occurrences (i.e. the number of samples exceeding the threshold computed summing the number of noisy spikes occurred over the 925 RR (Reduced Resolution) pixels located in the same line (same frame time), 185 per each camera) along all the 14809 total RR frames forming the descendent orbit from the start latitude and longitude until the stop latitude and longitude.

Considering that every line is acquired and transferred to the storage zone and then to the shift register every 44ms (all the elementary spectral lines constituting a single band are transferred together to the storage zone and then binned), the abscissa axis is equivalently described in terms of ‘Time’ instead than ‘Lines or frames’. The image of the entire orbit is acquired in 14809 RR frames of 0.04*4 s each (approx. 592*4 seconds, where factor 4 is used to take into account the Reduced Resolution). Associating the starting time with ’Time’=0, Envisat flies over the center of the South Atlantic Anomaly (around -25 to -30 degrees of latitude) after approx. 1600 seconds, which correspond to line number 10000.

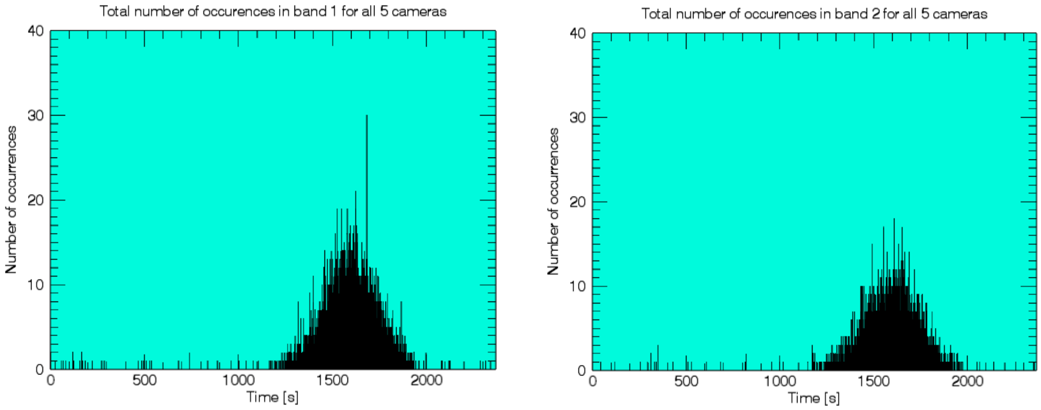

Figure 3.3.1. *Number of occurrences in band number 1 and 2, over the entire descending orbit #292.*

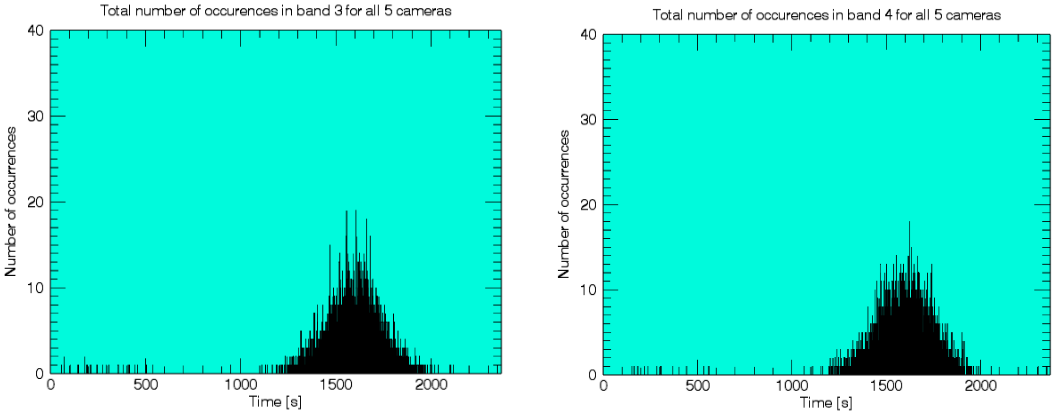

Figure 3.3.2. *Number of occurrences in band number 3 and 4, over the entire descending orbit #292.*

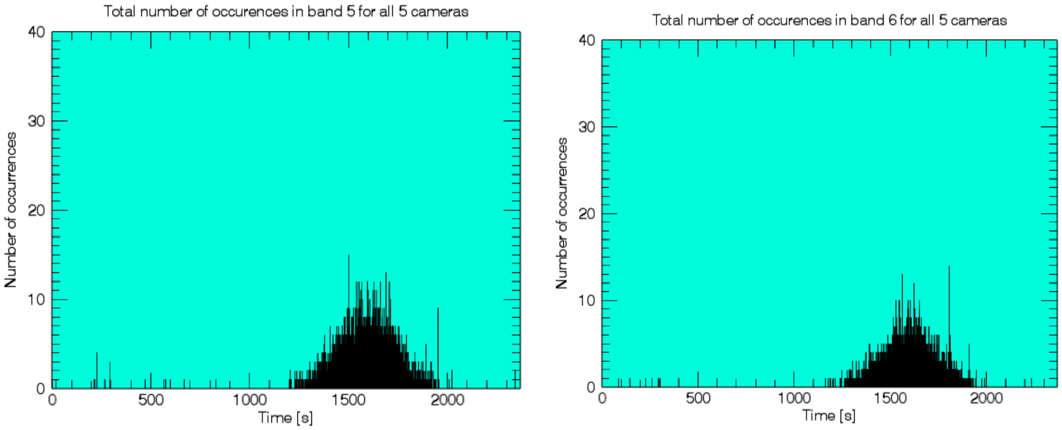

Figure 3.3.3. *Number of occurrences in band number 5 and 6, over the entire descending orbit #292.*

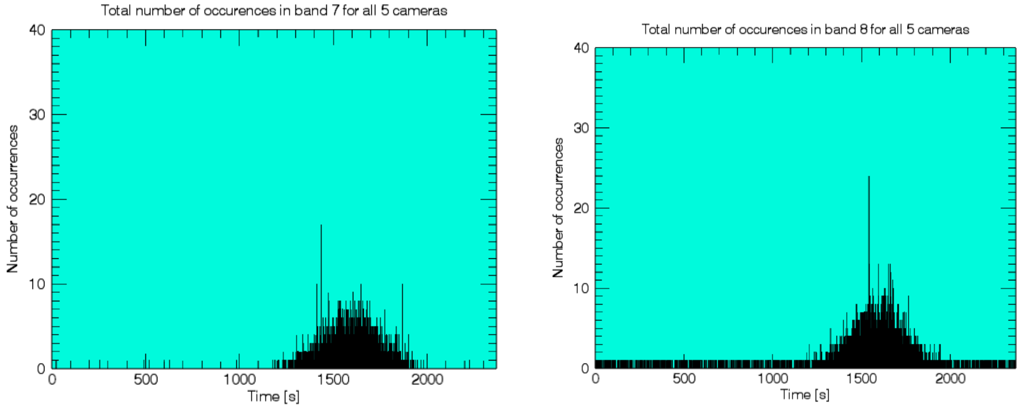

Figure 3.3.4. *Number of occurrences in band number 7 and 8, over the entire descending orbit #292.*

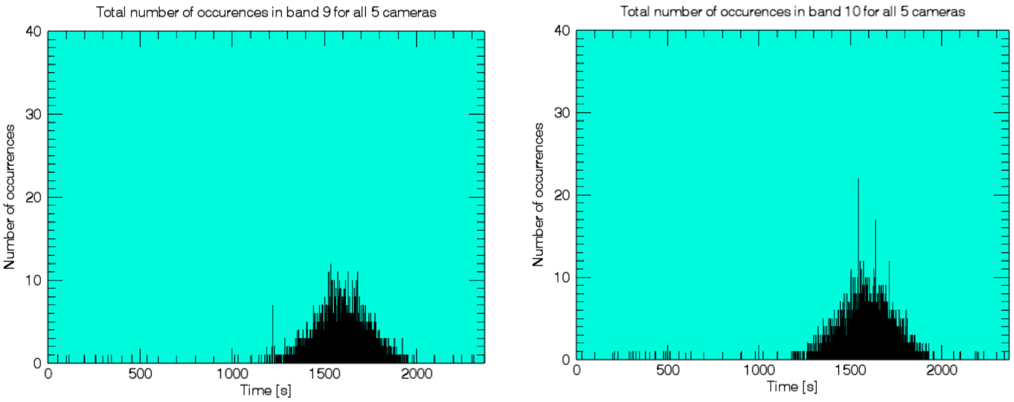

Figure 3.3.5. *Number of occurrences in band number 9 and 10, over the entire descending orbit #292*.

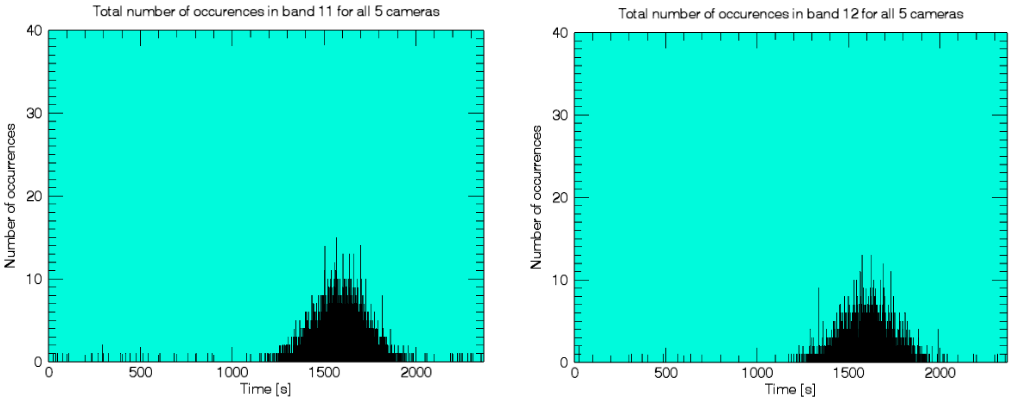

Figure 3.3.6. *Number of occurrences in band number 11 and 12, over the entire descending orbit #292.*

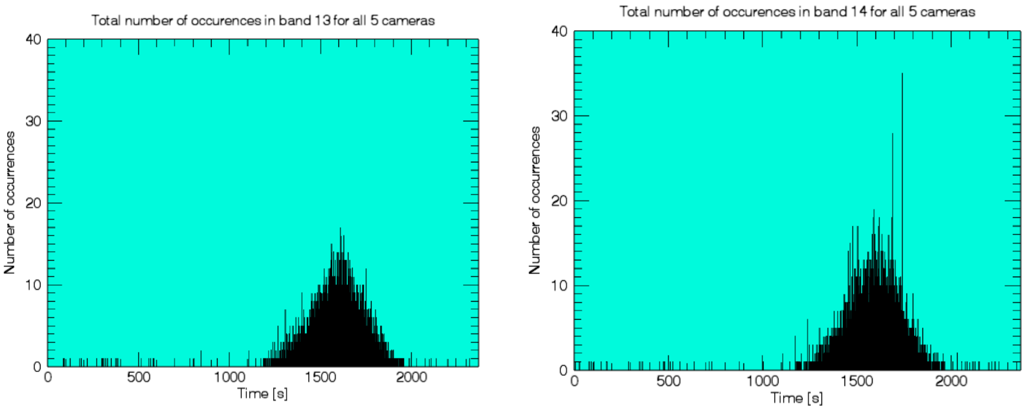

Figure 3.3.7. *Number of occurrences in band number 13 and 14, over the entire descending orbit #292.*

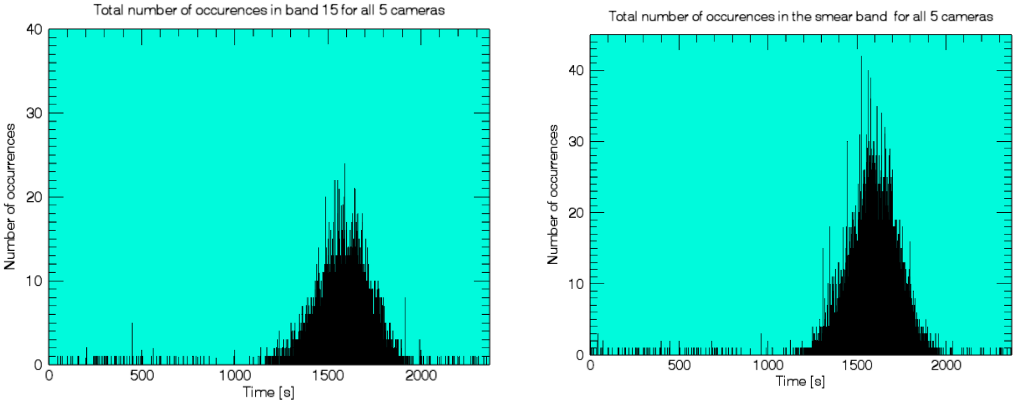

Figure 3.3.8. Number of occurrences in band number 15 and in the smear band, over the entire descending orbit #292.

The average standard deviation value for the smear band is higher than the other bands because the smear band signal is obtained binning 31 elementary spectral lines. Thus, the total surface of MERIS smear band detectors exposed to the noisy radiation is wider compared to other bands (see Table 3.3.1): the surface occupied on the CCD by one smear band RR pixel is equal to 31 x $(22.5\ \mu m)^2$ x 16 corresponding to 251100 μm^2, where 31 is the number of binned spectral lines, $(22.5\ \mu m)^2$ is the surface of the single detector on the CCD and 16 are the number of pixels used for spatial relaxation. In the other bands, the RR pixel surface varies from a minimum of 24300 µm^2 (band 11) to a maximum of 129600 µm^2 (band 13).

MERIS BAND NUMBER	VEU GAIN	NUMBER OF MICROBANDS	NUMBER OF LINES PER MICROBAND	TOTAL NUMBER OF SPECTRAL LINES	NUMBER OF LAST LINE IN THE BAND
1	1.25	2	4	8	22
2	1	2	4	8	46
3	1	2	4	8	84
4	1	2	4	8	100
5	1.75	4	2	8	140
6	1.5	4	2	8	188
7	1.5	4	2	8	224
8	1	2	3	6	236
9	1.75	4	2	8	256
10	1.25	2	3	6	294
11	1.25	1	3	3	297
12	1	3	4	12	314
13	1.75	4	4	16	384
14	1.75	1	8	8	404
15	1	1	8	8	412
16 (Smear)	3.75	1	31	31	520

Table 3.3.1. Band default values (during Envisat commissioning phase).

The probabilities of an occurrence were computed for each band dividing the total number of occurrences for the total number of samples under test and are resumed in Table 3.3.2 for two different regions, one outside and the other inside the SAA. The first, located outside the SAA, includes 6475000 RR pixels per band (7000 lines, 185 RR pixels and 5 camera modules) corresponding to a start sensing latitude of +79.64 deg and a stop sensing latitude of +9.64 deg. The second region under test is located inside the SAA and includes 3700000 RR pixels per band (4000 lines, 185 RR pixels and 5 camera modules) corresponding to a start sensing latitude of -0.26 deg and a stop sensing latitude of -80.26 deg. Here, the occurrence probability is in the order of

10^-3 for all the 15 observation bands. In the case of the smear, an occurrence probability of 3*10^-2 was measured.

Outside the SAA, for all MERIS bands (except the 13th, the 15th and the smear) the occurrence probability is in the order of 10^-6. For the 13th, the 15th and the smear the probability of an occurrence reaches the order of 10^-5. The reason why the 13th band is slightly more affected by cosmic rays may be justified with the wider surface of this band, as it is composed binning 16 elementary spectral lines. The smear band is in general the most affected due to its wider surface and to the effect that the aluminum shield may have on the energetic particles. The proximity to the shield covering the smear band may explain why also the 15th band has a higher occurrence probability. For each band, no significant difference in terms of occurrences was noticed varying the latitude (selecting a different across-track line) and the longitude (selecting a different camera).

Outside the SAA, in the worst (highest) case, the detected occurrences are in number less or equal than 5 over 925 RR pixels (i.e. one across-track line: 185 RR pixels times 5 cameras), depending on the selected band. Inside the SAA, in the worst case, the occurrences may vary from a number of 14 (band 6) up to 42 (smear band). These results are shown in Figure 3.3.9.

OCCURRENCE PROBABILITY *Pr(OCC)* (Envisat MERIS RR L0 data, abs. orbit 292, commissioning phase)		
BAND NUMBER	*Pr(OCC OUTSIDE THE SAA)* (AL-track lines 1-7000, AC-track RR pix 1-925)	*Pr(OCC INSIDE THE SAA)* (AL-track lines 8001-12000, AC-track RR pix 1-925)
1	8,80 E-06	6.6 E-03
2	7,57 E-06	5.3 E-03
3	6,02 E-06	5.1 E-03
4	5,87 E-06	5.3 E-03
5	8,49 E-06	5.8 E-03
6	4,32 E-06	4.8 E-03
7	5,25 E-06	4.5 E-03
8	3,87 E-06	3.2 E-03
9	4,63 E-06	4.7 E-03
10	5,87 E-06	3.7 E-03
11	4,32 E-06	2.5 E-03
12	4,17 E-06	4.1 E-03
13	1,24 E-05	8.0 E-03
14	6,18 E-06	5.5 E-03
15	1,10 E-05	4.9 E-03
Smear	8,39 E-05	3.0 E-02

Table 3.3.2. *Occurrence probabilities inside and outside the SAA*

depending on the MERIS band.

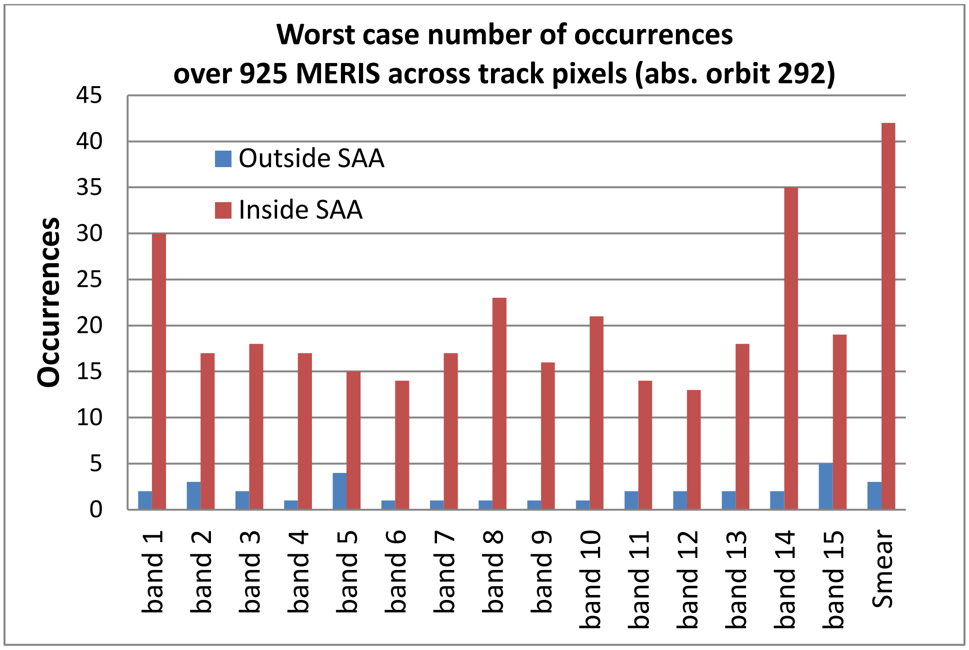

Figure 3.3.9. Worst case number of occurrences over one line (925 MERIS AC-track RR pixels) along Envisat descendent orbit 292.

3.4 MERIS sensitivity to cosmic rays

The LSB value of the pixels affected by energetic particles was taken into account for two different data sets: one, outside the SAA, from line 1 to line 7000 and the other, inside the SAA, from line 8001 to line 12000. For first, the mean value of those corrupted pixels (as "*spike mean*") was computed for each MERIS band and compared to the mean dark signal value at the VAM output (the latter was computed averaging the mean values of the five cameras over lines 1 to 7000, for each band, in order to have a data set less corrupted by the noisy radiation), see Figure 3.4.1.

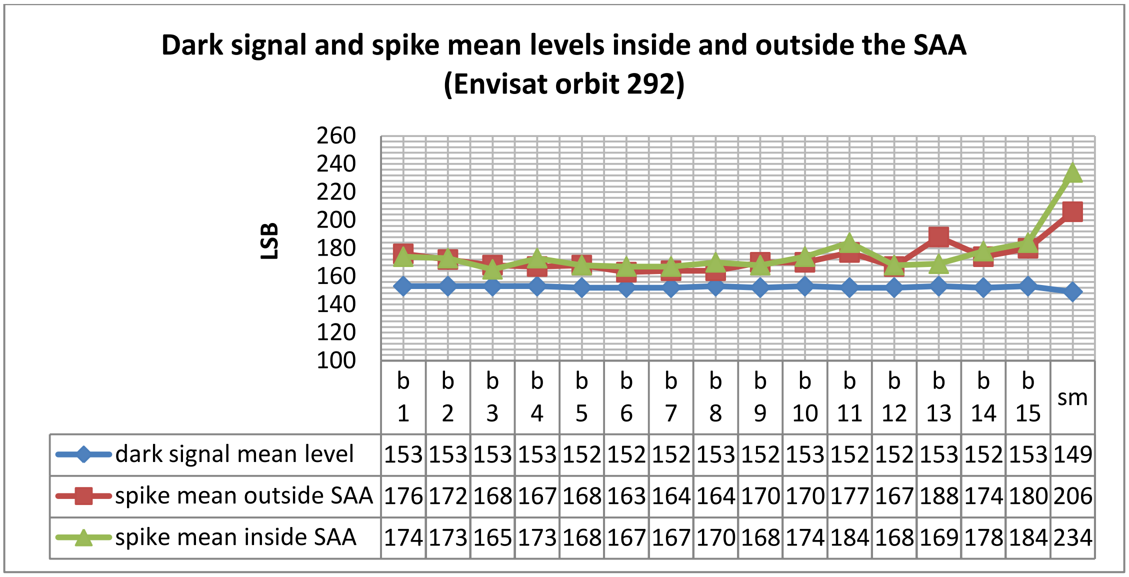

	b 1	b 2	b 3	b 4	b 5	b 6	b 7	b 8	b 9	b 10	b 11	b 12	b 13	b 14	b 15	sm
◆ dark signal mean level	153	153	153	153	152	152	152	153	152	153	152	152	153	152	153	149
■ spike mean outside SAA	176	172	168	167	168	163	164	164	170	170	177	167	188	174	180	206
▲ spike mean inside SAA	174	173	165	173	168	167	167	170	168	174	184	168	169	178	184	234

Figure 3.4.1. MERIS RR dark signal and spike mean levels for Envisat absolute descendent orbit 292.

Afterwards, the impact of high-energy particles in the SAA on the dark signal red out at the VAM output was quantified for two different cases. In the first case, the difference between the mean spike level and the dark signal mean value (obtained as described before) was computed for all the 16 bands. In the second case (the worst case), depending on the band, the dark signal mean value was subtracted from the maximum spike value detected along the entire descendent orbit. The results are reported in Figures 3.4.2-3.4.3.

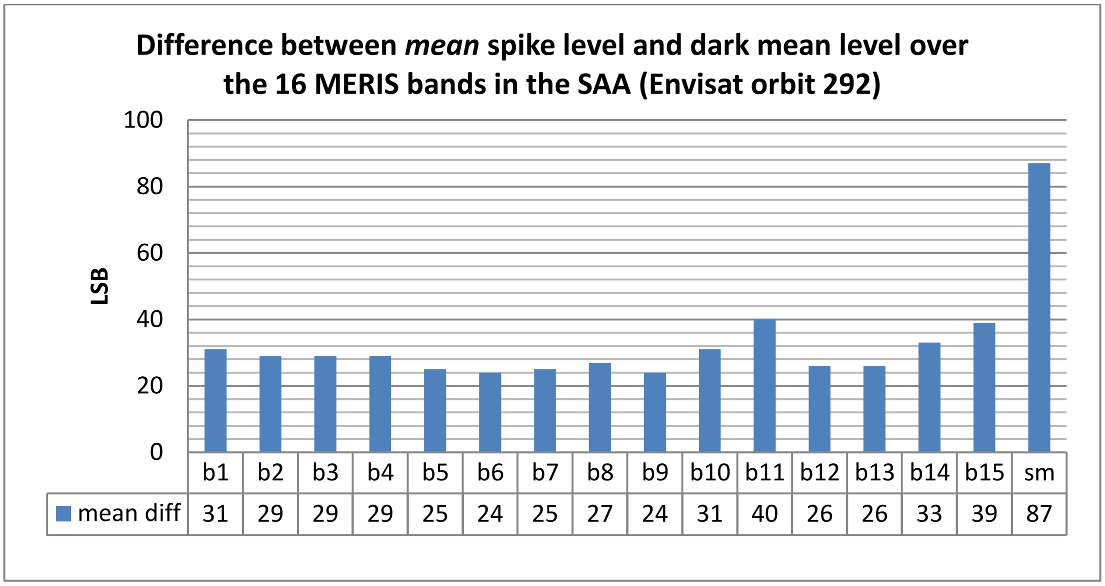

Figure 3.4.2. Difference between mean spike level and dark mean level for all the 16 MERIS bands (Envisat descendent orbit 292).

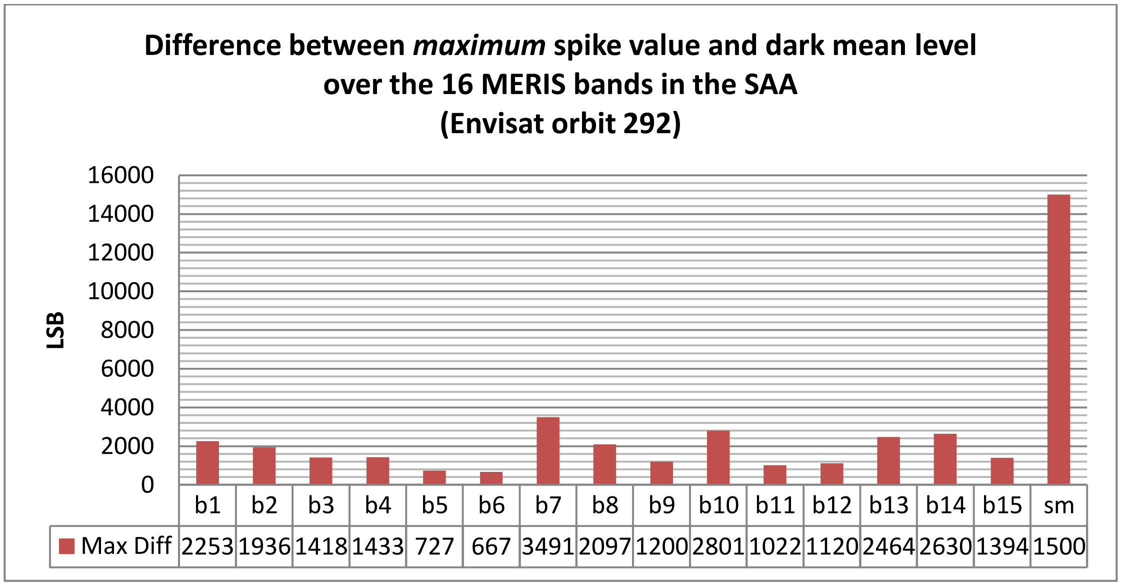

Figure 3.4.3. Difference between maximum spike value and dark mean level for all the 16 MERIS bands (Envisat descendent orbit 292).

For MERIS observation bands, on average, pixels affected by cosmic rays show similar LSB values both inside and outside the SAA. The noisy radiation in the South of the Atlantic, even if more persistent, doesn't seem stronger than in the rest of the orbit. Most of the detected spikes are in the range of 165-175 LSBs. In the case of the smear band, affected pixel values usually exceed 200 LSBs and show higher values in the SAA than outside (approx. 20 LSBs more on average).

The difference between mean spike level and dark mean level in the SAA (except for the smear band, these results are substantially valid for all the observation bands along the entire orbit) is included on average in the range of 24-40 LSBs for the observation bands, while it is higher for the smear (87 LSBs).

Next, the amplitude distribution of the affected pixels was analyzed. For this, the normalized histogram of the corrupted LSB values (see Figures 3.4.4-3.4.6) was retrieved for MERIS band number 1 (10 nm), 8 (7.5 nm), 11 (3.75 nm), 12 (15 nm) and 13 (20 nm), thus covering all the cases of bandwidth for the observation bands. The normalization was done by dividing each value of the histogram for the total number of detected occurrences in all cameras along the entire descendent orbit for that specific band.

Then, a model of probability density function better fitting with the histogram was searched.

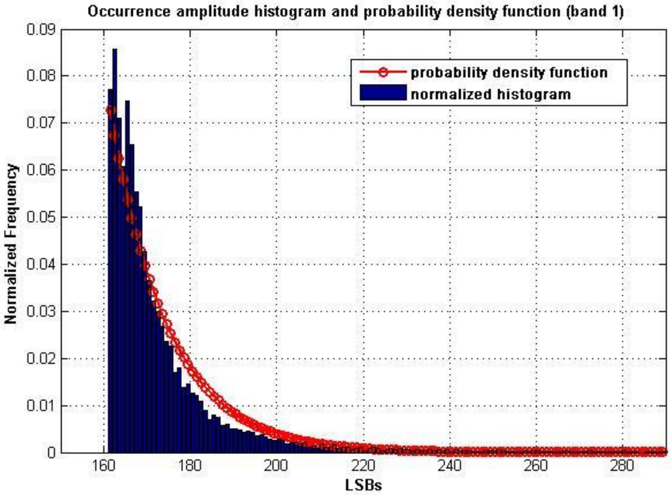

Figure 3.4.4. Occurrence amplitude histogram and probability density function (band 1).

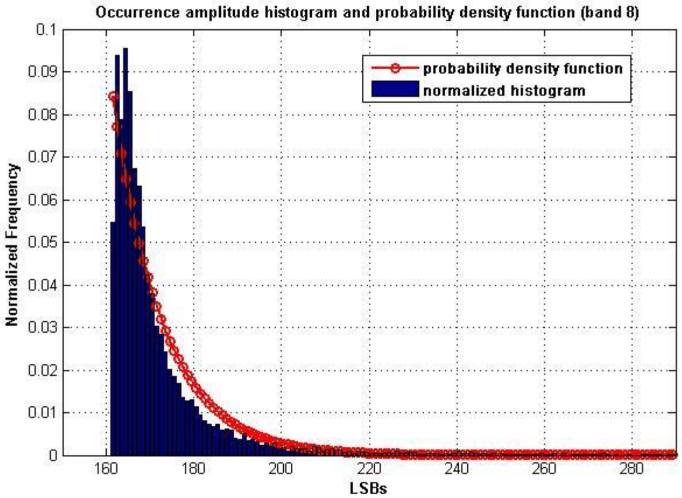

Figure 3.4.5. Occurrence amplitude histogram and probability density function (band 8).

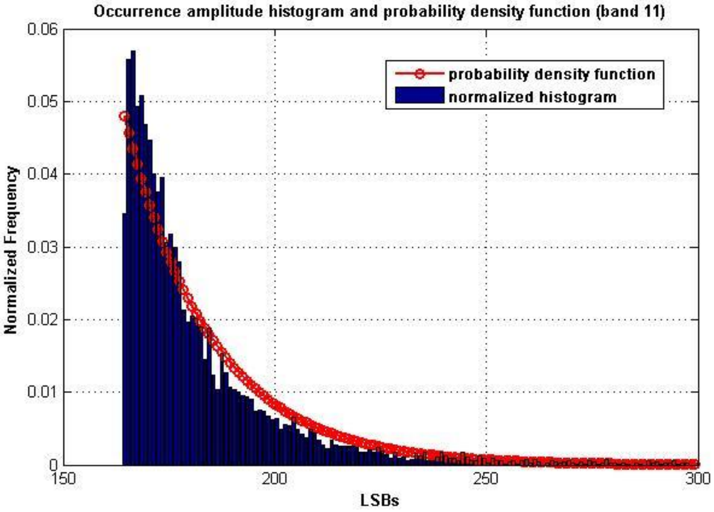

Figure 3.4.6. Occurrence amplitude histogram and probability density function (band 11).

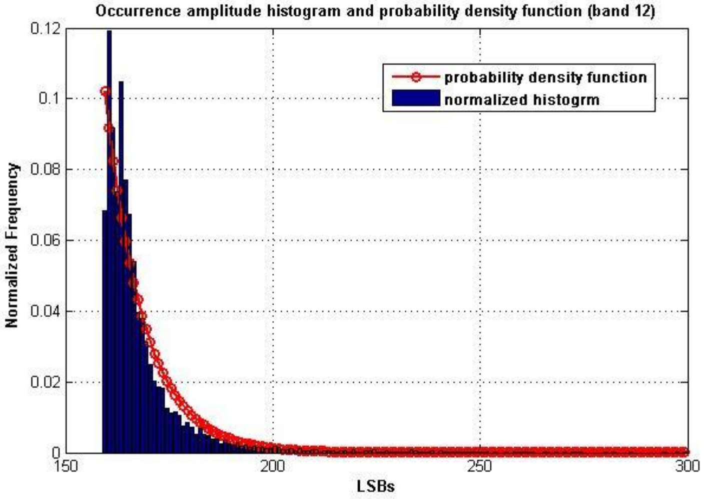

Figure 3.4.7. Occurrence amplitude histogram and probability density function (band 12).

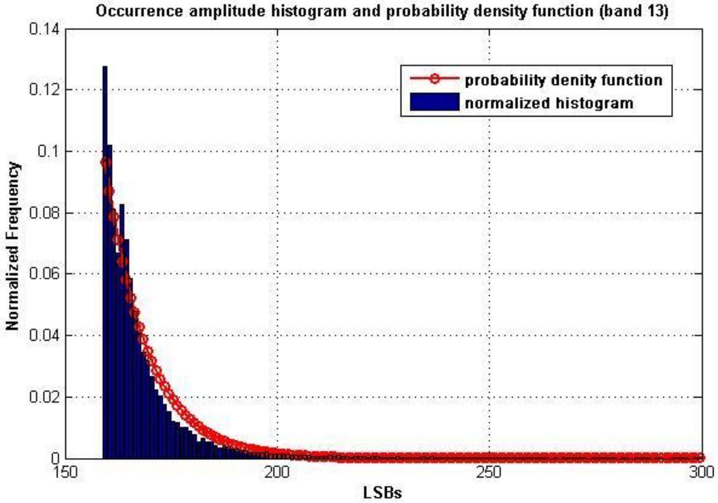

Figure 3.4.8. Occurrence amplitude histogram and probability density function (band 13).

In order to approximate the occurrence amplitude probability density a shifted exponential function was proposed:

$$p(x|corrupt\ pixel) = \lambda \exp[-\lambda\,(x - x_m)]\ u(x - x_m),$$

where λ is the inverse of the difference between the spike mean and the spike minimum value x_m for that precise band and u is the step function.

The previous Figures 3.4.4-3.4.6 and the represented function (red line) show that the chosen function is an acceptable approximation.

3.5 Adjacent affected pixels

The effects of the impact of a cosmic ray on the CCD surface was studied also with the purpose of understanding the influence that the hit may have on the adjacent pixels of the CCD. In fact, the high-energy particle could not affect just one RR pixel. The impact may affect also adjacent pixels located in the same spatial line and even in other adjacent spectral lines, corrupting also adjacent bands.

To find those adjacent RR pixel values corrupted by a cosmic ray, two or more consecutive pixels located in the same across-track line and exceeding the aforementioned threshold $Th_b^{(c)}$ were detected. This was done for all the 16 MERIS bands and for two different data sets, one outside the SAA (from line 1 to line 7000, including all the five camera modules) and the other inside the SAA (from line 7001 to line 12000, including all the five camera modules). As an example, the next Figure 3.5.1-3.5.3 show some significant cases of corrupted consecutive dark pixel values (the first four appearing inside the SAA and the last two outside).

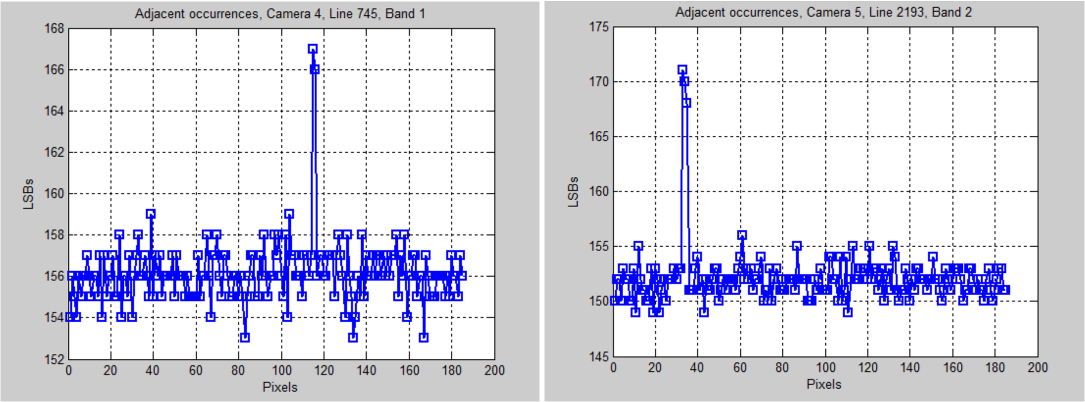

Figure 3.5.1. Adjacent occurrences detected outside the SAA in camera 4, line 745, band 1 (left) and in camera 5, line 2193, band 2 (right).

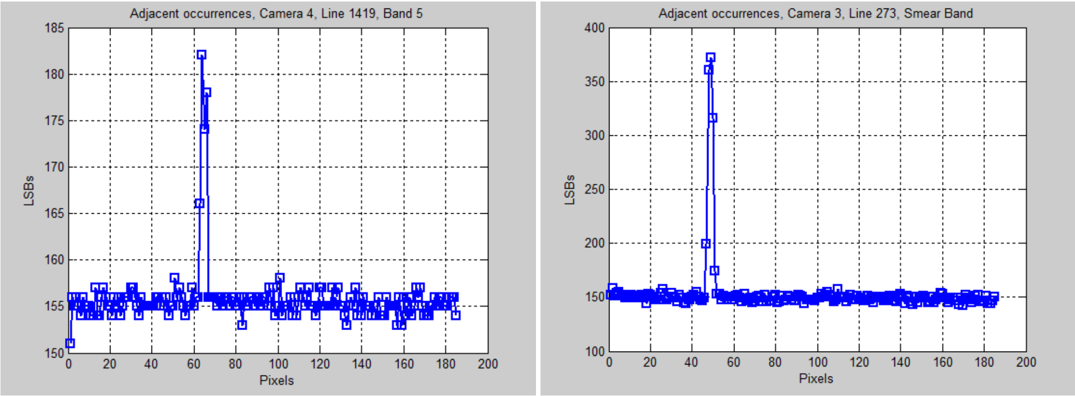

Figure 3.5.2. Adjacent occurrences detected outside the SAA in camera 4, line 1419, band 5 (left) and in camera 3, line 273, smear band (right).

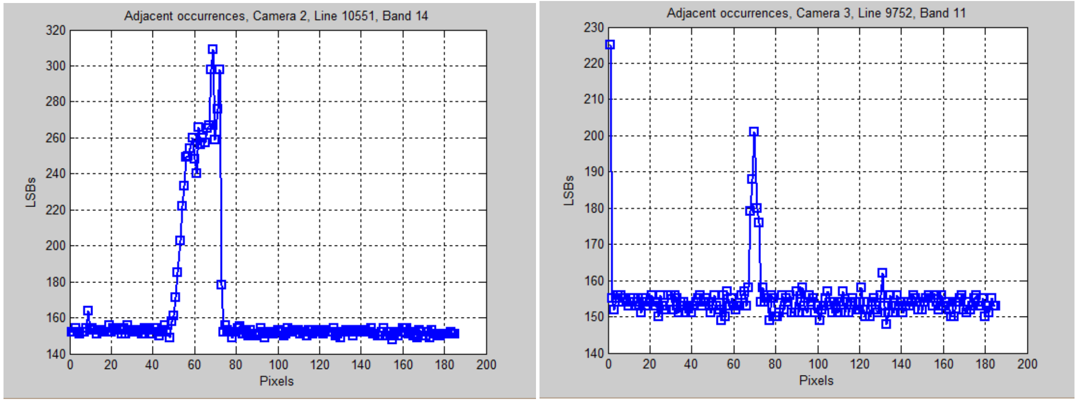

Figure 3.5.3. Adjacent occurrences detected inside the SAA in camera 2, line 10551, band 14 (left) and in camera 3, line 9752, band 11 (right).

The analyze dealt with two main issues. The event "two or more consecutive pixels are affected along the same AC-track line and band" was defined. For first, the number of times the event occurred in the data set was counted (for each band). For second, the maximum number of consecutive affected pixels was determined (for each band). The results for each data set and band are shown in Table 3.5.1.

Number of times two or more consecutive affected pixels occur in the AC-track line and band		
MERIS BAND	OUTSIDE SAA (AL-track lines 1-7000, AC-track RR pix 1-925)	INSIDE SAA (AL-track lines 8001-12000, AC-track RR pix 1-925)
1	4	1734
2	9	1448
3	5	1467
4	0	1490
5	4	1614
6	1	1303
7	0	1196
8	0	845
9	1	1326
10	0	972
11	2	549
12	0	1222
13	4	2544
14	1	1617
15	6	1458
Smear	49	15563

Table 3.5.1. Number of times two or more consecutive affected pixels occur in the AC-track lines, outside and inside the SAA.

Maximum number of consecutive affected pixels in the AC-track lines		
MERIS BAND	OUTSIDE SAA (AL-track lines 1-7000, 925 AC-track RR pix)	INSIDE SAA (AL-track lines 8001-12000, 925 AC-track RR pix)
1	1	7
2	2	7
3	1	9
4	0	5
5	3	6
6	1	5
7	0	15
8	0	12
9	1	7
10	0	9
11	1	4
12	0	6
13	1	8
14	1	23
15	4	6
Smear	4	21

Table 3.5.2. Maximum number of consecutive affected pixels

in the AC-track lines, outside and inside the SAA.

Several cases of consecutive AC-track pixels exceeding the threshold were detected. This may depend on different factors: the intensity of the cosmic ray that hits the semiconductor and its direction which is not always perpendicular to the surface of the CCDs or (in the case of the smear band) on some multiple reflections due to the aluminum shield which covers the 31 smear microbands.

Not all the adjacent pixels over the threshold may be related to a unique hit, especially in the SAA where the radiation is more persistent. Here the probability of two (spatial) consecutive hits at the same time is a lot greater than outside the SAA. This could be the case of Figure 3.5.3 (left plot) where over the corrupted pixels there is more than one relative maximum LSB value.

Afterwards, the analysis focused on those RR pixels exceeding the threshold located in the same position over the across-track line and in consecutive bands. Also in this case, this was done for each band and for two different data sets: one containing dark measurements from outside the SAA (lines 1 to 7000, pix 1 to 925) and the other from inside the SAA (lines 8001 to 12000, pix 1 to 925).

The results are reported in Table 2.5.3 for both data sets. Figures 3.5.4-3.5.5 depict two cases detected in the northern hemisphere.

Number of times of affected consecutive pixels occurring in the same across-track line position and in adjacent bands		
MERIS BANDS	OUTSIDE SAA (lines 1 to 7000, pix 1 to 925)	INSIDE SAA (lines 1 to 7000, pix 1 to 925)
1-2	0	92
2-3	0	62
3-4	0	73
4-5	0	81
5-6	0	67
6-7	0	51
7-8	0	48
8-9	0	52
9-10	0	38
10-11	1	143
11-12	0	30
12-13	0	87
13-14	1	124
14-15	0	83
15-Smear	0	360

Table 3.5.3. Number of times of affected consecutive pixels

occurring in the same across-track line position and in adjacent bands.

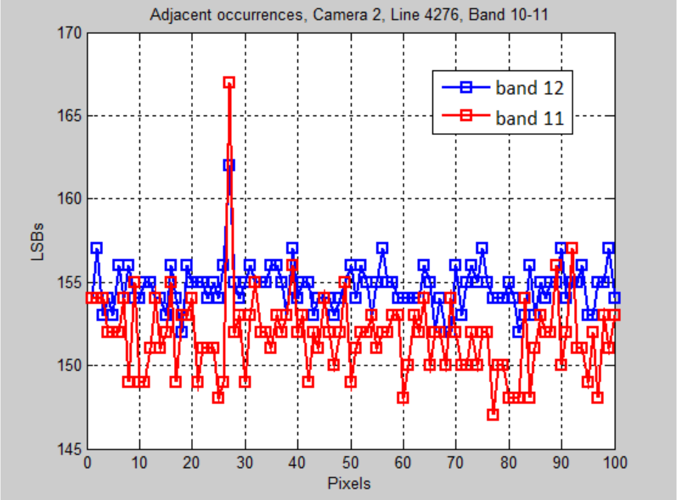

Figure 3.5.4 . Adjacent occurrences, camera 2, Line 4276, MERIS bands 10 and 11.

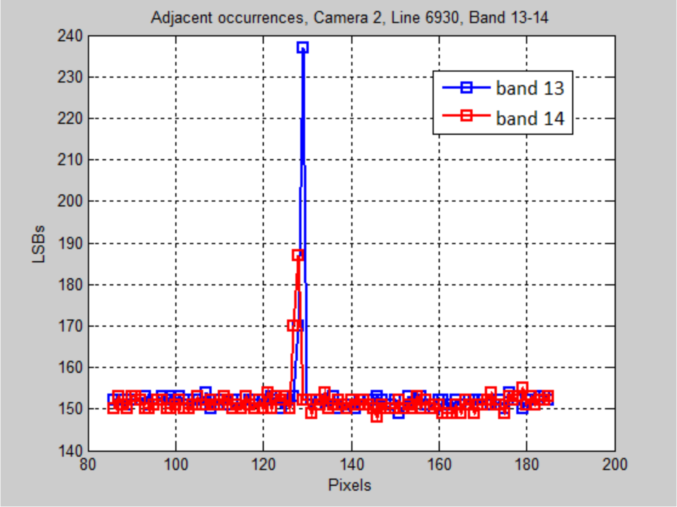

Figure 3.5.5. Adjacent occurrences, camera 2, Line 6930, MERIS bands 13 and 14.

Two cases of corrupted pixels in the same AC-track position and adjacent bands were detected outside the SAA over 97125000 samples under test, corresponding to a probability of

2*10^-8. It can be assumed that these two cases are both related to a single cosmic ray impacting on that CCD area.

Inside the SAA, for all the bands, such event was detected numerous times. Even here, it is hard to say if those adjacent occurrences are related to a single strike or not. If so, it is possible to assert that in the case of the observation bands, the maximum CCD surface interested by one hit of the energetic particle is at least equal to 337.5 μm^2, obtained multiplying $(2.5\ \mu m)^2$ by a factor 54, where the latter represents the number of CCD elements separating the last elementary spectral line of band 12 from the first of band 13.

Chapter 4 Detection of PPEs in the smear band during MERIS operational phase

4.1 The smear signal in the radiometric model

The principles of radiometric calibration and its model are essential to understand how the LSB level (i.e. digital numbers, DN) are generated while MERIS is performing measurements in the nominal Earth observation mode. It will also be necessary to understand the relation between the signal generated related to the incoming top-of-the-atmosphere radiance and the generated smear signal. This will help to develop a strategy to detect pixels affected by cosmic radiation in the smear band and to monitor their occurrence over seven years.

All MERIS data taken into account were acquired using the nominal EO mode. The same mode will be available for OLCI, hence the findings and methodology are directly applicable to OLCI. The design of OLCI and MERIS were already described in the previous chapter 2 and will not be repeated.

The MERIS radiometric model [18], as for OLCI, is expressed as follows :

$$DN_{b,k,m,t} = NL_{b,m}\left[A^0_{b,k,m} \cdot \left(L_{b,k,m,t} + SL_{b,k,m,t}\right) + Sm_{b,k,m,t} + C^0_{b,k,m}\right] + \varepsilon$$

where:

- *DN* is the MERIS raw sample expressed in digital numbers, i.e. LSBs;
- *b*,*k*,*m*,*t* subscripts respectively stand for the spectral band, the spatial pixel, the camera (module) and the acquisition time;
- *NL* is a non-linear function representing the transformation which takes place in the CCD, amplifier and ADC (Analogue to Digital Converter) and it is tabulated from pre-flight characterized camera data scaled to the specific setting of each band;
- *L* is the spectral radiance distribution in front of the sensor (TOA radiance);
- A^0 is the instrument absolute radiometric gain in counts/radiance unit;
- *SL* is the stray-light contribution to the signal; it depends on *L*;
- *Sm* is the smear signal, due to the continuous sensing of light by the instrument during the transfer of the information to the storage zone of the CCD; it depends on *L* and *SL;*
- C^0 is the dark signal;
- ε is a random process related to noise and measurements errors.

The MERIS instrument itself provides a characterization measurement supporting the radiometric processing, that is the smear band. In fact, as MERIS works with frame transfer CCDs, image smear is inevitably caused by the basic operating principle of the device [19] and needs to be corrected.

Right after the integration time (exposure time), the charged packets at row *n* are transferred at a clock rate from the image zone to the storage zone. During the transfer, the imager is not shielded from the incoming light and the generation of charged packets continues; the row is exposed to all wavelengths higher than its nominal one (transfer toward the NIR spectrum) up to 1040 nm. In the same way, before the exposure, the virtual empty row is scrolled down from the top of the CCD toward its nominal position, thus being exposed to all wavelengths shorter than its nominal one, starting from 390 nm. The smear signal is the sum of these two terms, see Figure 4.1.1. The transfer time (1.3 ms) is very short compared to the exposure time (42.7 ms): it is about the 3% of it and the integration of the smear signal could be considered instantaneous.

The smear band is a fully virtual band built to estimate and correct the smear signal contribution. The band integrates 31 rows covered by an aluminum shield (as it happens also in OLCI CCDs) located outside the exposed CCD area, thus integrating only the incoming radiance field during the transfer (Figure 4.1.1 and 4.1.2). The signal is acquired in the same way as for the observation bands and it is transmitted to ground in a separate band (the 16th) to allow correction of the observation bands.

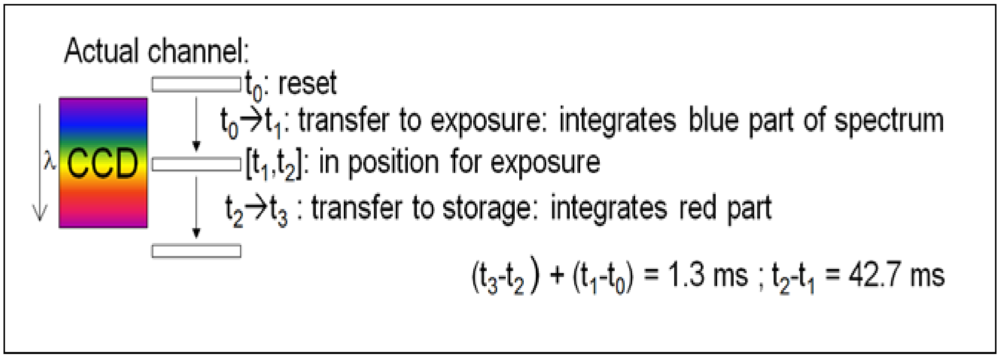

Figure 4.1.1. Smear signal generation for an actual band.

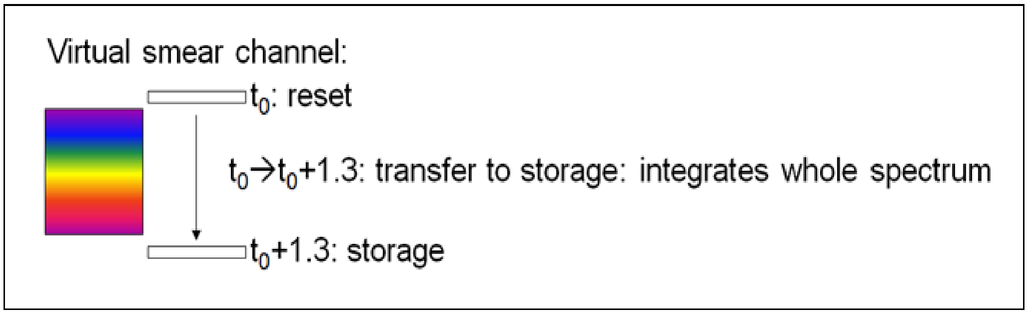

Figure 4.1.2. The virtual smear band generation (quantities expressed in ms).

Every observation band is corrected by a weighted average of smear band values at t_1 and t_2, according to the band wavelength, as follows (the equation is used for the smear correction in L1B processing):

$$Sm\left(b, \frac{t_1 + t_2}{2}\right) = \frac{DN_{sm}(t_1) \cdot (\lambda_b - 390) + DN_{sm}(t_2) \cdot (1040 - \lambda_b)}{1040 - 390}.$$

4.2 PPE detection algorithm in MERIS smear L0 RR data over ocean

The objective of this section is to develop a robust procedure allowing the detection of noise spikes due to PPEs in the smear L0 reduced resolution data over ocean.

The idea makes use of the data from the 15 MERIS observation bands in order to make an estimation of the smear signal ($\hat{S}$). Once the estimated value is retrieved, it was subtracted from the smear counts (*Sm*) as recorded by the sensor summing the signal from 31 shielded spectral lines located outside the exposed CCD area and red out from the inspected file. The problem was analyzed in steps *1)*, *2)*, *3)* and *4) below*. Out of this an algorithm is concluded, which is described below in points *a)*, *b)*, *c)* and *d)*. In general, those pixels exhibiting a value higher than a certain threshold were classified as corrupted by a cosmic ray hitting on the corresponding RR pixel on the CCD surface or on one of the adjacent pixels (over the same elementary spectral line or over other different close lines spectrally binned into another spectral band).

An accurate estimation of the smear signal $\hat{S}$ may be retrieved for all the cloud-free water pixels of those specific swaths of the orbit not too wide (i.e. maximum 1000 lines, 185 pixels). In this way, it may be possible to guarantee a sufficient uniformity of the Sun zenith and azimuth angles and to reduce or avoid the problem of Sun glint to which MERIS is particularly sensitive [20]. The Table 1.2.1 indicates, for each band, the Center Wavelength (CW), the bandwidth (Δλ), the gain (applied after the charges are converted into voltage before the ADC) and the number of elementary spectral lines which are summed together to obtain the full band radiance signal during spectral relaxation.

1) In order to retrieve an estimation of the radiance counts (i.e. Digital Numbers*, DN*) for each elementary spectral line, the values related to each band's read out from the file were divided for the corresponding number of spectral lines and band gain (applied after the charges are converted into voltage before the ADC), according to the values illustrated in Table 4.2.1. This operation was done for all the pixels of the selected swath.

2) These values were used to build up the interpolation curve in order to calculate the digital counts for all the 520 lines (from 390 nm up to 1040 nm, with a sampling interval of 1.25 nm). It was decided to apply a simple linear interpolation. Keeping in mind that MERIS observation bands go from 412 nm up to 900 nm and because of the impossibility of obtaining an accurate behavior of the curve after 900 nm, the interpolation was stopped before 901.25 nm. The value measured at band 15 (900 nm) was assigned for the lines from 901.25 nm up to 1040 nm.

3) The estimated smear signal $\hat{S}$ was approximated summing the 520 digital numbers *DN,* one per each elementary spectral line (before and after the considered one) and weighting the sum by a factor obtained dividing the transfer time T_{trans} per spectral line (2.5 µs) by the integration time T_{int} (42.7 ms), as expressed below:

$$\hat{S}(i) = \frac{T_{trans}}{T_{int}} \sum_{\substack{k=1 \\ k \neq i}}^{520} DN_k \,,$$

where *k* stands for the *k*-th spectral line before and after the considered spectral line *i (i* = 1, 2, …, 520*).*

4) The reconstructed smear signal $\hat{S}$ is subtracted from the smear L0 counts (*Sm*) measured by MERIS and read out from the MERIS RR L0 data file in order to retrieve a difference signal (*D*) proportional to the dark signal:

$$D = Sm - \hat{S}$$

Note that the above outlined procedure represents an approximation: in step *1)* and *2)*, the eventual change of the scene observed by MERIS (from *k<i* to *k>i*) was not taken into account: after the integration time, while the charge is being transferred towards the storage zone, the scene and the related TOA radiance spectrum may change (from a cloud pixel to the adjacent water pixel or vice versa). Thus, the reason why the algorithm works better over water pixels is due to the more homogeneous scene observed by MERIS over ocean compared to a cloudy scene, as it may be observed later from the histogram.

MERIS band	CW [nm]	Bandwidth [nm]	Number of spectral lines	Gain
1	412.5	10	8	1.5
2	442.5	10	8	1.25
3	490	10	8	1
4	510	10	8	1
5	560	10	8	1
6	620	10	8	1
7	665	10	8	1
8	681.25	7.5	6	1.25
9	708.75	10	8	1
10	753.75	7.5	6	1
11	761.75	3.75	3	1
12	778.75	15	12	1.25
13	865	20	16	1.5
14	885	10	8	1
15	900	10	8	1.25
Smear	-	-	31	3.75

Table 4.2.1. Central wavelength, bandwidth, number of lines and gains for the 16 MERIS bands.

The procedure was then transferred to an algorithm to detect pixels which are affected by a cosmic ray impact on the photodetector surface. This is explained in the following steps:

a) Camera module (*m*) and the swath *DN*(*k* to *k*+*N*, *t* to *t*+*NT)* are selected, where *N* is a positive integer and *T* is equal to 44 ms.

b) For that swath, a histogram is computed using the DNs for the red band (*b*=13) and a threshold is selected to create the water mask *DN*(*k* to *k*+*N*, *t* to *t*+*NT)* in order to classify a pixel as water or else (cloud or land).

c) The reconstructed smear dark signal values of pixels classified as water are taken into account. For those pixels the mean value μ and the standard deviation σ are computed.

d) Pixels affected by high energy particles are considered those whose value exceeds the following threshold *th*:

$$th = \mu + 5\sigma.$$

The first step of the algorithm suggests the selection of the data related just to one camera module (limiting the longitude to a maximum of 1000 AL-track lines). The reason, as already underlined, is principally due for the necessity of choosing an almost uniform swath in longitude in respect to the Sun illumination conditions and the presence of Sun glint may be not relevant.

If the first step is not respected and the selected data set refers to more than one camera module, the classification of water pixels will not be correct due to a misinterpret of the histogram which may bring to a wrong choice of the threshold.

The selection of the threshold may depend on the latitude of the selected swath and on the acquisition month, as the Sun illumination angle may vary significantly.

4.3 Data analysis and results

The investigation concerned MERIS L0 data acquired when Envisat was over the South Atlantic Anomaly to understand which is the trend of the worst-case impact of this noisy radiation on the photodetectors over the period of seven years.

Among the four MERIS level 0 products (the Full Resolution L0, the Reduced Resolution L0 (RR L0), the Reduced Field of View L0 and the Calibration Level) [21], the RR L0 Measurement Data

Set (MDS) were analyzed. These consist of time ordered AISPs (acquisition instrument source packets) collected while the instrument is operating in reduced resolution mode. The Instrument Source Packets are data received from the instrument, with a small header attached by the Front End Processor EP [22]. The Level 0 RR Measurement Data Set (MDS) contains values expressed in digital numbers on 12 bits of digitization for all the 15 observation bands plus the additional so-called smear.

The analysis took the following 7 different data sets into account (one per year, from 2003 until 2009):

- *MER_RR__0PPLRA20090124_115150_000026062075_00467_36092_7541.N1*
- *MER_RR__0PPLRA20041009_112743_000026322031_00066_13647_1890.N1*
- *MER_RR__0PPLRA20050103_113006_000026162033_00295_14878_3547.N1;*
- *MER_RR__0PPLRA20060425_112704_000026342047_00109_21706_0924.N1;*
- *MER_RR__0PPLRA20070115_110909_000026302054_00395_25499_7768.N1;*
- *MER_RR__0PPLRA20080416_113629_000026302067_00424_32041_3036.N1;*
- *MER_RR__0PPLRA20090124_115150_000026062075_00467_36092_7541.N1.*

To demonstrate how the analysis is performed it is demonstrated step by step making use of the following file of the previous list:

- *MER_RR__0PPLRA20090124_115150_000026062075_00467_36092_7541.N1*.

The file refers to Envisat descendent absolute orbit number 36092 as shown in Figure 4.3.1. The total lines acquired along track are 14809. The number of spatial reduced resolution pixel across-track are 925 (185 RR pixels per camera). Camera number 5 images the western part of the orbit. Each line corresponds to 1.2 Km (AL-track) on ground. The space craft flies over the South Atlantic Anomaly approximately after line 8000 until line 12000.

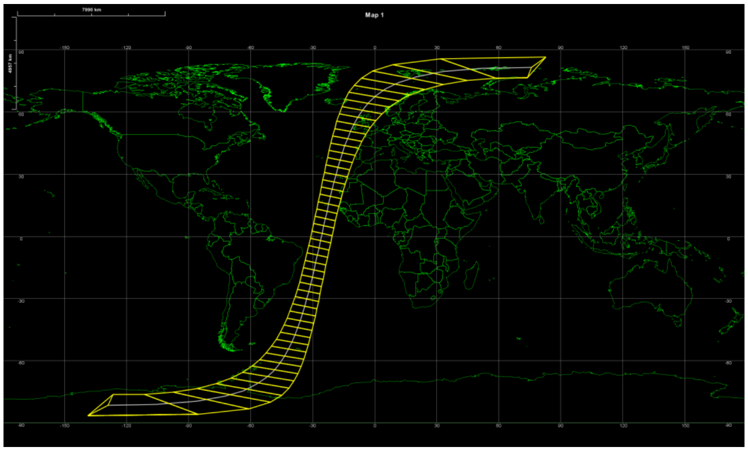

Figure 4.3.1. Envisat descendent absolute orbit 36092 reproduced with ESOV software and showing MERIS swath.

The signal acquired by the 31 spectral lines constituting the smear band is shown as an example in Figures 4.3.2-4.3.4, for the first spatial pixel of each camera (the one imaging the western part of the relative swath), from line 4000 up to line 1200.

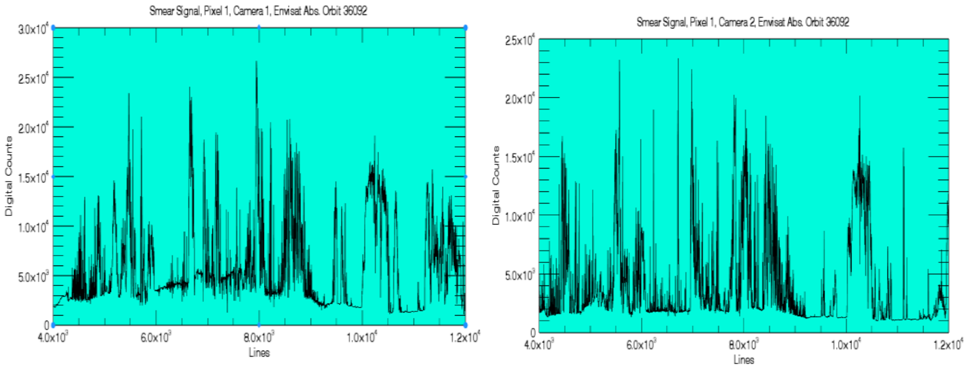

Figure 4.3.2. Smear band signal level for the first spatial pixel,

camera 1 (left) and 2 (right), lines 8500-9500, orbit 36096.

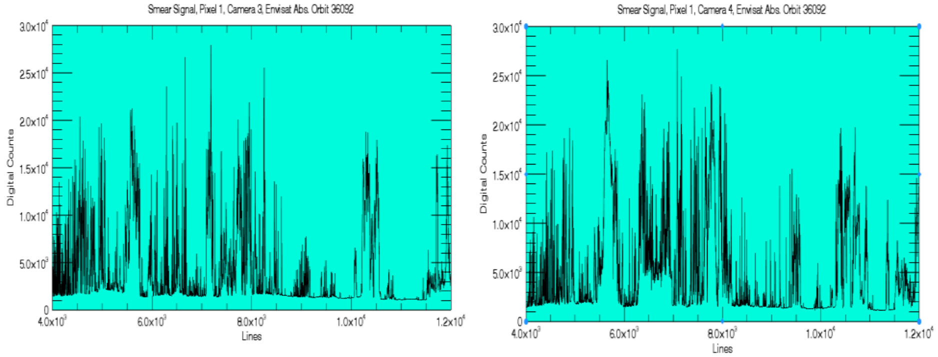

Figure 4.3.3. Smear band signal level for the first spatial pixel,

camera 3 (left) and 4 (right), lines 8500-9500, orbit 36096.

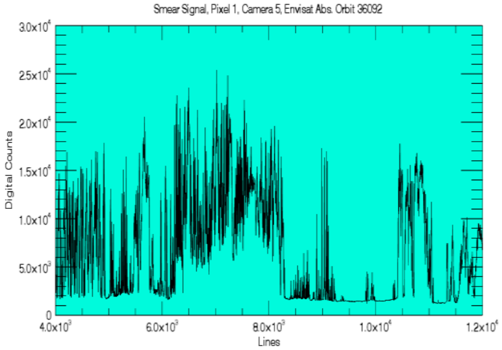

Figure 4.3.4. Smear band signal level for the first spatial pixel, camera 5,

lines 8500-9500, orbit 36096.

The analysis of the data reveals that the behaviour of the smear signal changes along the orbit. The smear dynamic range for Envisat absolute orbit number 36092 goes from a minimum of 533 up to a maximum of 36080 counts over 12 bits of digitization (considering all cameras).

The smear signal level is strongly influenced by the scene observed by MERIS even though the 31 elementary spectral lines are shielded by an aluminum layer. This is clear after imaging the smear signal: the scene represented matches with the same scene imaged with the RGB color model using MERIS bands number 13 (Red), 4 (Green) and 2 (Blue), see Figure 4.3.5 and Figure 4.3.6.

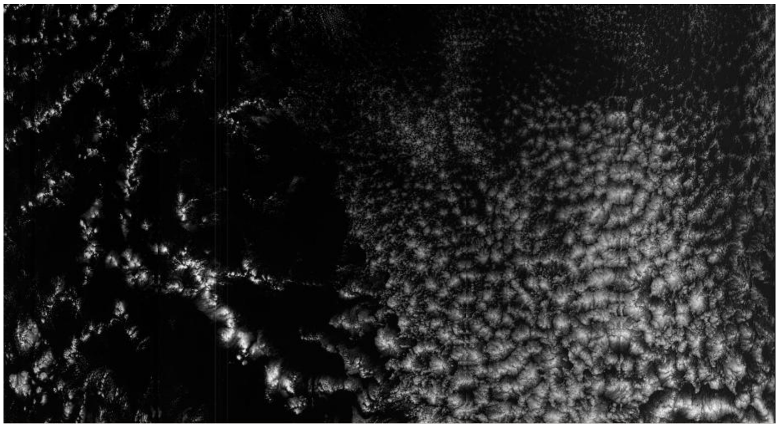

Figure 4.3.5. 925 x 501 RR pixels Smear greyscale image

(Lines 8500-9000, Abs. Orbit 36092).

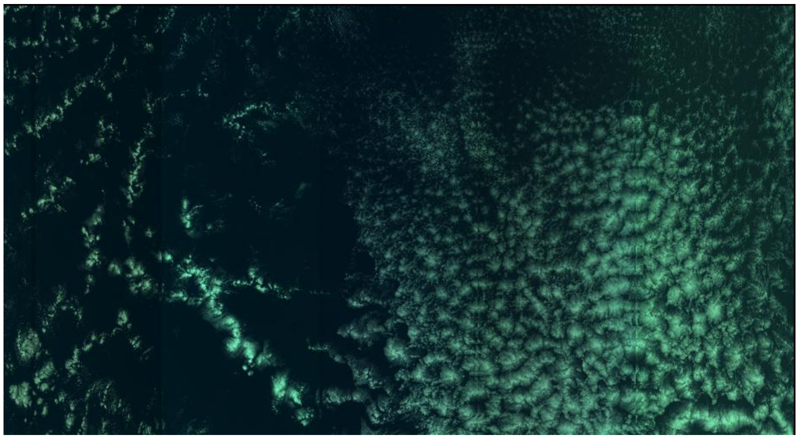

Figure 4.3.6. 925 x 501 RR pixels RGB image

(Lines 8500-9000, Abs. Orbit 36092).

Steps *1)*, *2)* and *3)* previously described were executed for all the pixels of the entire descendent orbit 36092 and in this way it was possible to retrieve an estimation of the smear band normalized signal. This is shown in Figure 4.3.7, where the upper curve (in blue) represents the smear signal acquired by the 31 shielded spectral lines located in between the image zone and the storage zone as red out from the level 0 RR data file and the lower one (in red) represents the reconstructed smear signal according to steps *1) – 3).*

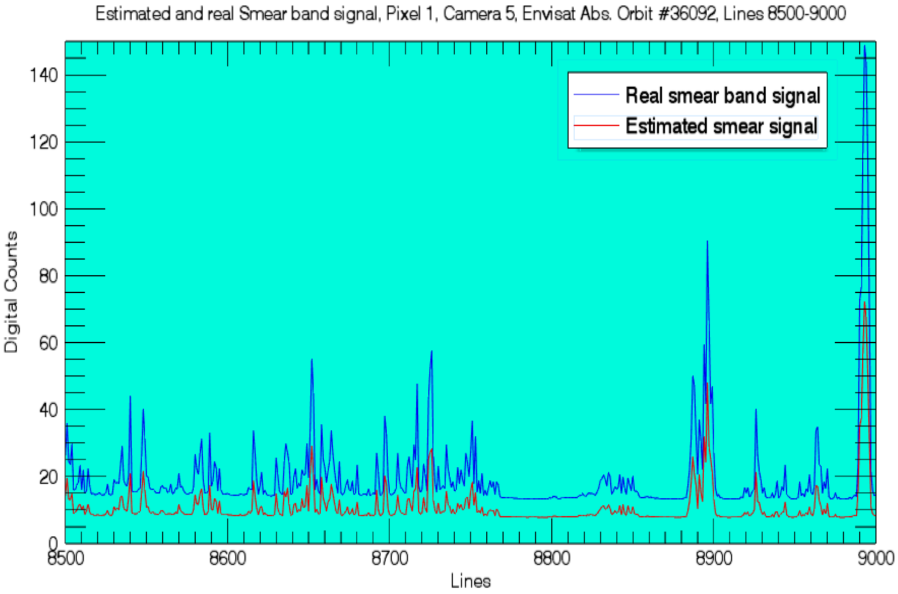

Figure 4.3.7. Real and estimated smear signal for the first spatial pixel of camera 5, absolute orbit number 36092, acquired from line 8500 to line 9000.

The previous plot demonstrates how the behavior of the reconstructed smear signal is proportional to the real smear signal read out from the file. The most evident difference between them is an amplitude offset. This happens because the reconstructed estimated smear signal doesn’t include the influence of the dark signal and the straylight.

The difference between the real signal *Sm* and the estimated one $\hat{S}$, was computed for the entire orbit, see Figure 4.3.8.It is directly related to the dark signal and to the straylight occurring in the cameras, as described by the radiometric model previously discussed.

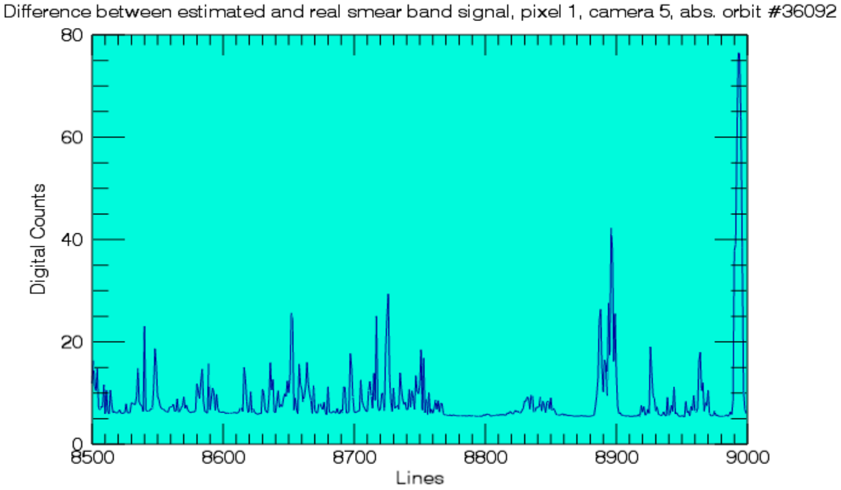

Figure 4.3.8. Difference between the reconstructed smear signal and the signal red out from MERIS Lo data

The correction seems to better work on homogeneous scenes. In fact the behavior of the curve representing the difference is flat for water pixels and it shows peaks over transition or cloud pixels (these peaks shouldn't be confused with the effect of a cosmic ray impact), as the spectrum may vary substantially before and after the integration time. This is not taken into account in the algorithm for reconstructing the dark signal as the spectrum considered for the reconstruction is supposed not to vary during the 44 ms.

At this point, two swaths observed by camera 5 were chosen: the first from line 9001 up to 10000 and the second from line 10001 up to 11000. In both cases, all the 185 RR across-track pixels were taken into account.

The histograms for those two regions (in Figure 4.3.9-4.3.10) were computed for band 13 in order to classify the water pixels (the ones not covered by clouds, as both swaths are acquired over ocean). The threshold value selected is 2000.

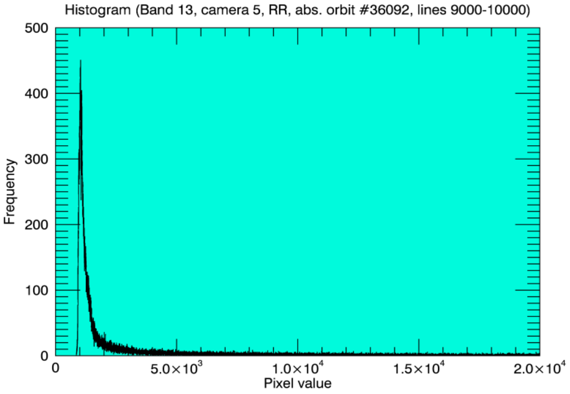

Figure 4.3.9. Histogram of MERIS band 13,

lines 9000-10000, Envisat orbit 36092, camera 5.

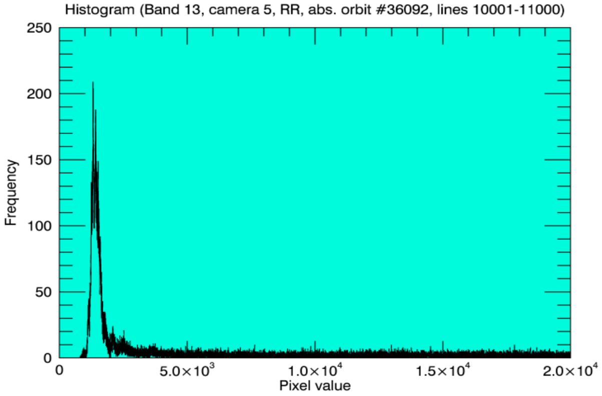

Figure 4.3.10. Histogram of MERIS band 13,

lines 10001-11000, Envisat orbit 36092, camera 5.

Assuming that all the pixels classified as cloud free, it the mean value and the standard deviation was retrieved for the difference signal *D* obtained at step *4)*.

Finally, those samples of signal *D* exceeding the mean value by more than 5 times the standard deviation were detected and it was possible to derive the percentage of occurrences of those anomalous values, as reported in Table 4.3.1.

ENVISAT ABSOLUTE ORBIT	CONSIDERED LINES (CAMERA 5, Smear Band)	THRESHOLD VALUE FOR WATER MASKING IN BAND 13	NUMBER OF DETECTED OCCURRENCES IN THE SMEAR BAND	NUMBER OF CONSIDERED WATER PIXELS	PERCENTAGE OF OCCURRENCES
36092 (15th Jan 2009)	LINES 9001-10000	2000	307	45667	0.67%
	LINES 10001-11000	2000	402	52587	0.76%

Table 4.3.1. Occurrences detected in the smear in camera 5

for two different MERIS swaths, year 2009.

The same procedure was applied for the remaining files related to six orbits crossing the SAA, from 2003 until 2008. The results are reported in Tables 4.3.2-4.3.7 (see Appendix A for the histograms of the swaths analyzed).

ENVISAT ABSOLUTE ORBIT 32041, 16th Apr 2008 CAMERA 5	CONSIDERED LINES	THRESHOLD VALUE FOR WATER MASKING FOR BAND 13	NUMBER OF DETECTED OCCURRENCES IN THE SMEAR BAND	NUMBER OF CONSIDERED WATER PIXELS	PERCENTAGE OF OCCURRENCES
OVER THE SAA	LINES 9001-10000	4750	117	58877	0.20%

Table 4.3.2. Occurrences detected in the smear in camera 5, year 2008.

ENVISAT ABSOLUTE ORBIT 25499, 15th Jan 2007 CAMERA 5	CONSIDERED LINES	THRESHOLD VALUE FOR WATER MASKING FOR BAND 2	NUMBER OF DETECTED OCCURRENCES IN THE SMEAR BAND	NUMBER OF CONSIDERED WATER PIXELS	PERCENTAGE OF OCCURRENCES
OVER THE SAA	LINES 9001-10000	2500	237	159676	0.15%

Table 4.3.3. Occurrences detected in the smear in camera 5 , year 2007.

ENVISAT ABSOLUTE ORBIT 21706, 25th Mar 2006 CAMERA 5	CONSIDERED LINES	THRESHOLD VALUE FOR WATER MASKING FOR BAND 2	NUMBER OF DETECTED OCCURRENCES IN THE SMEAR BAND	NUMBER OF CONSIDERED WATER PIXELS	PERCENTAGE OF OCCURRENCES
OVER THE SAA	LINES 9001-10000	7500	2802	113376	2.47%

Table 4.3.4. Occurrences detected in the smear in camera 5 , year 2006.

ENVISAT ABSOLUTE ORBIT 14878, 3rd Jan 2005 CAMERA 5	CONSIDERED LINES	THRESHOLD VALUE FOR WATER CLASSIFICATION IN BAND 13	NUMBER OF DETECTED OCCURRENCES IN THE SMEAR BAND	NUMBER OF CONSIDERED WATER PIXELS	PERCENTAGE OF OCCURRENCES
OVER THE SAA	LINES 9001-10000	3000	3	1308	0.23%

Table 4.3.5. Occurrences detected in the smear in camera 5 , year 2005.

ENVISAT ABSOLUTE ORBIT 13646, 9th Oct 2004 CAMERA 5	CONSIDERED LINES	THRESHOLD VALUE FOR WATER MASKING FOR BAND 2	NUMBER OF DETECTED OCCURRENCES IN THE SMEAR BAND	NUMBER OF CONSIDERED WATER PIXELS	PERCENTAGE OF OCCURRENCES
OVER THE SAA	LINES 9001-10000	3250	599	73736	0.40%

Table 4.3.6. Occurrences detected in the smear in camera 5 , year 2004.

ENVISAT ABSOLUTE ORBIT 9267, 8th Dec 2003 CAMERA 5	CONSIDERED LINES	THRESHOLD VALUE FOR WATER MASKING FOR BAND 2	NUMBER OF DETECTED OCCURRENCES IN THE SMEAR BAND	NUMBER OF CONSIDERED WATER PIXELS	PERCENTAGE OF OCCURRENCES
OVER THE SAA	LINES 9001-10000	7250	746	85322	0.87%

Table 4.3.7. Occurrences detected in the smear in camera 5 , year 2003.

For the developed procedure a analysis result over the duration 2002 – 2009 has been obtained. The result can be depicted from Figure 4.3.13. It shows the trend of the occurrences of PPEs for MERIS smear band in the SAA. The results obtained, apart from year 2006, are in line with the occurrence probability estimated in Chapter 3 that was in the order of 10^-3, thus corresponding to a percentage of 10^-1. A slightly deviating result was obtained for year 2006, maybe due to the Solar activity cycle, as the latter is decorrelated with the number of PPEs.

It needs to be noted that the retrieved results only represent a snapshot accuracies over the different years. Even though 10^3 to 10^5 pixels have been used, a more systematic analysis of annual data is needed to retrieve a final conclusion.

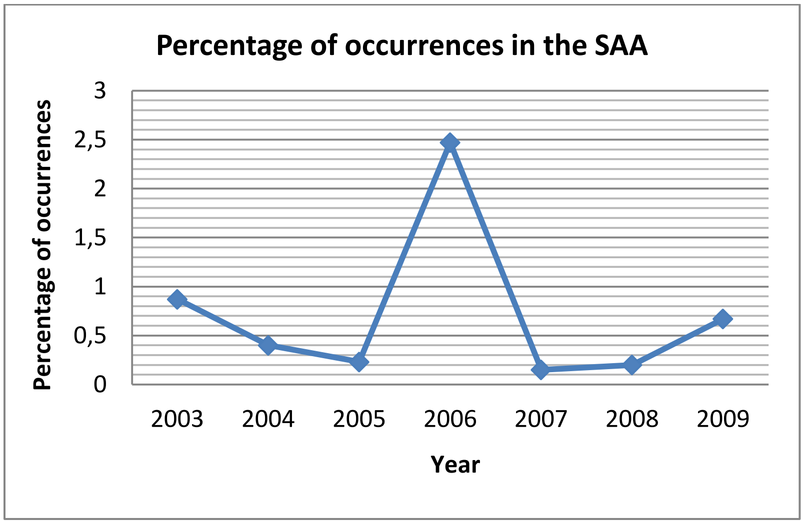

Figure 4.3.11. Trend of the occurrence percentage in the SAA, from 2003 until 2009.

Chapter 5. PPEs detection in Maximum Chlorophyll Index images

5.1 MCI algorithm

In order to analyze the influence of PPEs on Earth Observation user products a specific MERIS algorithm was selected which is making use of MERIS Top Of the Atmosphere (TOA) radiance/reflectance signal.

The Maximum Chlorophyll Index (MCI) algorithm exploits the height of the water-leaving radiance peak measurement in 9th MERIS spectral band (705 nm) above a baseline passing through two other spectral bands (see Table 5.1.1 below for all MERIS bands), the 8th (681 nm) and the 10th (753 nm). The MCI index is associated to the concentration of chlorophyll *a* on the surface of ocean, costal and lake waters [4].

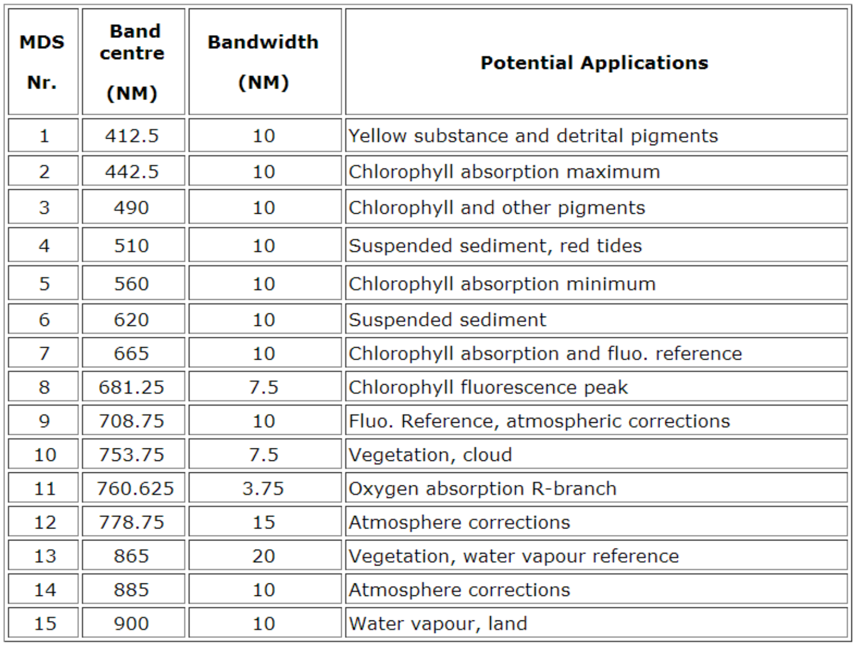

MDS Nr.	**Band centre (NM)**	**Bandwidth (NM)**	**Potential Applications**
1	412.5	10	Yellow substance and detrital pigments
2	442.5	10	Chlorophyll absorption maximum
3	490	10	Chlorophyll and other pigments
4	510	10	Suspended sediment, red tides
5	560	10	Chlorophyll absorption minimum
6	620	10	Suspended sediment
7	665	10	Chlorophyll absorption and fluo. reference
8	681.25	7.5	Chlorophyll fluorescence peak
9	708.75	10	Fluo. Reference, atmospheric corrections
10	753.75	7.5	Vegetation, cloud
11	760.625	3.75	Oxygen absorption R-branch
12	778.75	15	Atmosphere corrections
13	865	20	Vegetation, water vapour reference
14	885	10	Atmosphere corrections
15	900	10	Water vapour, land

Table 5.1.1. MERIS spectral bands and main potential applications.

MCI values are computed from level 1B (L1B) data, i.e., Top Of the Atmosphere (TOA) calibrated radiances, before atmospheric correction, since the events of interest give radiances outside the range that can be handled by correction algorithms.

The interpolated baseline is designed to represent the shape of the spectrum of "clear" water which does not show any peaks in nominal conditions.

The algorithm is the following:

$$MCI = L_9 - L_8 - (L_{10} - L_8) \cdot \frac{\lambda_9 - \lambda_8}{\lambda_{10} - \lambda_8}$$

where L_i indicates the water-leaving radiance for band *i,* centered at wavelength λ_i (*i*=8,9,10). The next Figure 5.1.1 remarks the peak exploited by the algorithm.

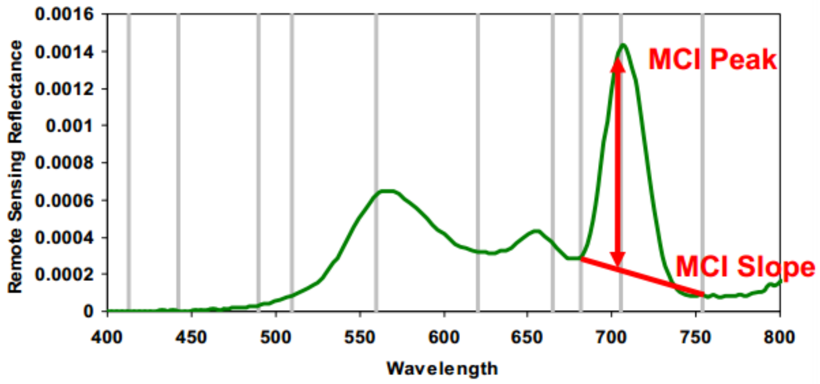

Figure 5.1.1. Example of chlorophyll peak at 708 nm [23].

As mentioned, the MCI index computed through the algorithm indicates the concentration of chlorophyll *a* against a scattering background. In particular, MCI values are high in evident "red tides" conditions, when intense and visible surface phytoplankton blooms appear.

Phytoplankton are photosynthesizing microscopic organism living in the lit surface of cold bodies of water. It is of high scientific interest to study with the use of satellite data the extent and concentration of phytoplankton or “primary production”. Phytoplankton obtains energy through the process of photosynthesis and because of this, when the concentration is significantly high, they may appear as a green discoloration of the water due to the presence of chlorophyll *a* within their cells or they may appear as “red tides” in the case of algal blooms.

In Figure 5.1.2 below three different curves are plotted. The clear-water water-leaving reflectance doesn’t show any peaks in the 681 nm, 708 nm and 753 nm bands. Green water shows a peak in correspondence of the 681 nm band, while red tides peak is really high in the 708 nm band.

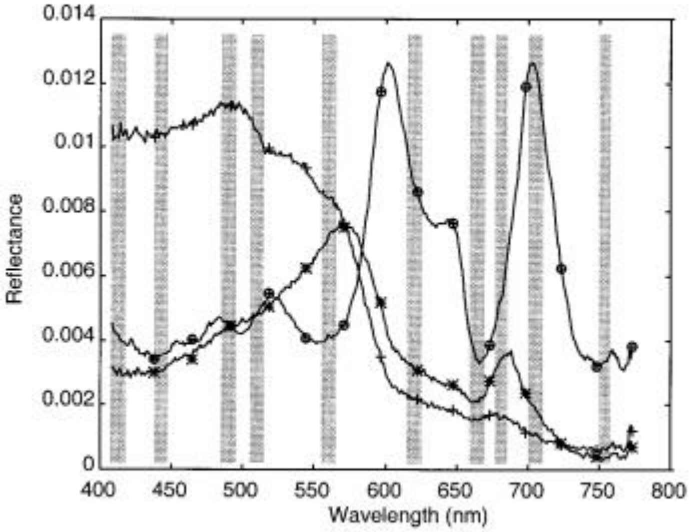

Figure 5.1.2. Measured reflectance spectra above the water in the northern North Sea from the research vessel Gauss. Spectra are corrected for reflected sky light: clear blue water (no peaks), green water (peak at 681 nm) and red tides (peak at 708 nm) are represented [24].

In Figure 5.1.3 the water-leaving reflectance spectrum is represented with different colors for different chlorophyll concentrations, from 0.1 mg/m^3 up to 30 mg/m^3.

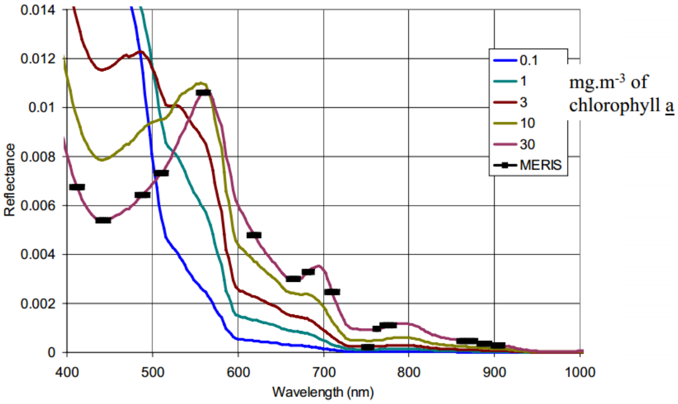

Figure 5.1.3. Water-leaving reflectance for different chlorophyll-a concentrations [25].

Among ocean color satellites sensors, the MCI index was unique to the MERIS/OLCI instruments, because the 708 nm band is not present on other optic sensors such as NASA's MODIS or SeaWiFS.

5.2 PPEs false alarms in MCI images

Cosmic rays are one of the sources of false alarms when MERIS MCI algorithm is used for retrieving phytoplankton blooms and other aquatic vegetation in ocean, sea, lake and other body of cold water.

Many sources of false alarms exist and need to be taken into account when analyzing MCI images in terms of phytoplankton blooms [26], such as for example benthic vegetation and coral reefs in shallow waters, or floating sargassum. Anyhow, the analysis will be focused in detecting false alarms in MCI images due to cosmic rays hitting on some elements of the CCD placed in the Focal Plain Assembly of the five cameras.

The global spatial distribution of single pixel events in the MCI image detected by MERIS makes possible to assert that most of these occur in the SAA and they are due to the impact of cosmic rays on the detectors of the instrument. Figure 5.2.1 was computed using all daily MCI composites for the month of July 2006. In other parts of the world, in the same figure, most events are due to water vegetation on isolated coral and other reefs. MCI values are computed only over cloud-free areas.

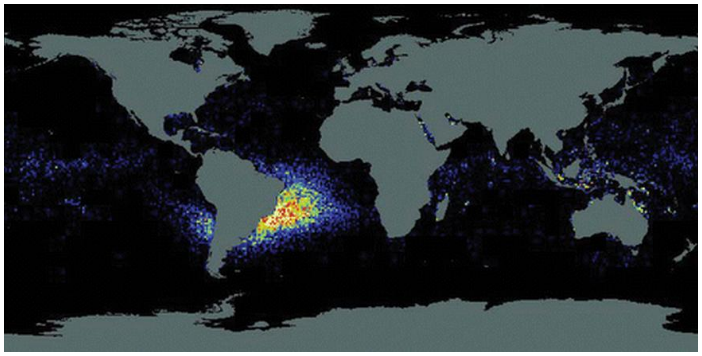

Figure 5.2.1. The global spatial distribution of single pixel events in the MCI image detected by MERIS revealing the typical pattern of the SAA. The image uses a color sequence according to which black indicates zero counts, and blue, green, yellow and red to white indicate 1 to 20 counts per pixel per month. Land is masked to grey [26].

The false alarms that occurred in the composite MCI image perfectly match with the region off Brazil where the Earth's magnetic field has its absolute minimum, see Figure 1.2.1.

5.3 Cosmic ray detection algorithm in MCI images

The objective of the following analysis is to develop an algorithm to detect pixels in open oceans (i.e. away from the coastal boundaries) which are affected by cosmic rays hitting on the relative elements of the CCD. In such a way it may be possible to distinguish high MCI value pixels which indicate a high presence of clorophyll *a* from those which represent a false alarm due to PPEs.

The algorithm revealing false alarms in retrieving chlorophyll surface blooms is applicable in that part of the water spectrum where the behaviour is "almost flat", so that the base line slope is low and the peak can easily come out. Thus, MERIS bands suitable for this purpose are those located from 680 nm up to 900 nm, that is from the 8th to the 15th. The same bands (with the addition of Oa 14, 15, 20 and 21) are foreseen also in Sentinel-3/OLCI, thus making the algorithm exploitable for the new upcoming ocean products.

The L1b data were processed making use of the *Beam* MCI L1B processor. MERIS bands number 8 (680 nm) and 10 (753 nm) were used as baseline and band 9 (708 nm) was used as the peak wavelength. The MCI algotithm (in nominal cases) gives high indexes when the radiance spectrum in the 9th band shows a high value of radiance due to the presence of a phytoplankton surface bloom.

All the pixels which can be considered as clouds, land, coast line or ''no data'' (cosmetic, duplicated, glint risk, suspect and invalid) were not taken into account making use of the appropriate flags[2]. For this, the "land/ocean", "bright" and "coastline" flags are direct inputs from Pixel Classification. The "duplicate" flag is a direct input of the Radiance Resampling. The "glint risk" flag is a direct input from geolocation. The "invalid" flag is a direct input, logically recombined with other flags, in order to gather all pixels satisfying any one of the following conditions : samples of all bands are saturated and/or out-of-swath product pixels and/or pixels added at the end of the product to reach the last tie frame and/or pixels added to fill a transmission gap of more than sixteen packets. The "cosmetic" flag coming from the processing chain is a per band flag ; the "suspect" flag is a new flag gathering pixels with diverse internal flags configurations. "Cosmetic" are those pixels for which at least one radiance sample has been replaced by interpolation from neighbors. “Suspect" are those pixels satisfying one of the following conditions : for any pixel, if it is flagged "stray light risk"; for a "clear sky" and "ocean" pixel, at least one of the radiance samples is "saturated" or "dubious" ; for a "clear sky" and "land" pixel, at least one of the radiance samples of the bands dedicated to "land" is "saturated" or "dubious" [21].

In order to establish if the MCI value associated to a pixel may be real or a false alarm, the 3x3 pixel area around the central pixel under investigation was analyzed. Among the eight edge pixels surrounding the one under test, just the ones with “valid”MCI value were used for the statistics.

Case 1

The central pixel value was considered as a false alarm due to cosmic rays when both of the following conditions were verified [4]:

a) The center MCI value exceeds the average of the edge pixels by more than 0.3 mW/(m^2*sr*nm);

b) The edge pixels standard deviation is lower than 0.05 mW/(m^2*sr*nm).

---

[2] The product data convention contained in the file name are explained in MERIS product handbook (see http://earth.esa.int/).

Case 2

If the previous two conditions are partially satisfied, that is condition *a)* is satisfied and condition *b)* is not, the pixel under test still needs to be considered a false alarm if its MCI value is greater than the threshold MCI_{th}, where the latter is equal to the mean value μ plus three times the standard deviation σ ($MCI_{value} > \mathrm{MCI}_{\mathrm{th}} = \mu + 3\sigma$) of the "valid" MCI data set under inspection.

In *case 1*, condition *a)* points out the higher value that the cosmic ray impact produces for the central affected pixel, while condition *b)* indicates that the pixel values around the one under test are uniform (and low, if condition *a)* is valid).

In some less probable cases, the cosmic ray may affect more adjacent pixels. Thus, even having condition *a)* satisfied, condition *b)* may not be true. This is the reason why it was introduced *case 2*. The choice of the threshold was made by inspection of the histograms of several swaths located in the SAA (at same coordinates) acquired by MERIS in different years. Focusing on the right tale of the histogram, different outliers were coming out.

5.4 Analysis and results

Seven Envisat MERIS Reduced resolution (RR) level 1B (L1B) images acquired during the period from 2003 to 2009 over the SAA were downloaded from MERCI (MERIS Catalogue and Inventory) database and were processed making use of the open source user-friendly BEAM VISAT software [27]. One criterion for the selection was a minimal presence of clouds as possible in the observed scene.

The following files related to the SAA were analyzed:

-MER_RR__1PRBCM20031208_121250_000002902022_00195_09267_0002.N1 ;

-MER_RR__1PRBCM20041009_115541_000002932031_00066_13647_0002.N1 ;

-MER_RR__1PRBCM20050103_115243_000002932033_00295_14878_0003.N1 ;

-MER_RR__1PRBCM20060425_120114_000002962047_00109_21706_0001.N1 ;

-MER_RR__1PNBCM20070115_113251_000002762054_00395_25499_0004.N1 ;

-MER_RR__1PRBCM20080416_120942_000002902067_00424_32041_0003.N1 ;

-MER_RR__1PRBCM20090124_121524_000002842075_00467_36092_0006.N1 ;

The instrument cross-track FOV of 68 degrees produces an image swath width of approximately 1150 km. The swath is comprised of 5 imaging spectrometer modules (5 cameras). For FR (Full Resolution) each pixel has an IFOV (Instantaneous Field Of View) of 0.019 degrees, with a nadir spatial sampling of 260 m across track by 290 m along track. Accordingly in a RR image a pixel represents an area of 1040 m across track × 1160 m along track. For oceans, the only MERIS L1B data available are in Reduced Resolution mode. The scene width is of 1121 (horizonthal) x 1665 (vertical) pixels.

In the following the analysis is summarized for the first file:

-MER_RR__1PRBCM20031208_121250_000002902022_00195_09267_0002.N1

The file refers to Envisat absolute orbit number 9267, relative orbit 195, sensing start on December 8th 2003 at 12:12:50 and sensing stop at 12:17:40.

In Figures 5.4.1 the swath of interest is shown on the world map and in Figure 4.4.2 it has been imaged the same swath in RGB mode making use of MERIS bands number 13 (R), 4 (G) and 2 (B).

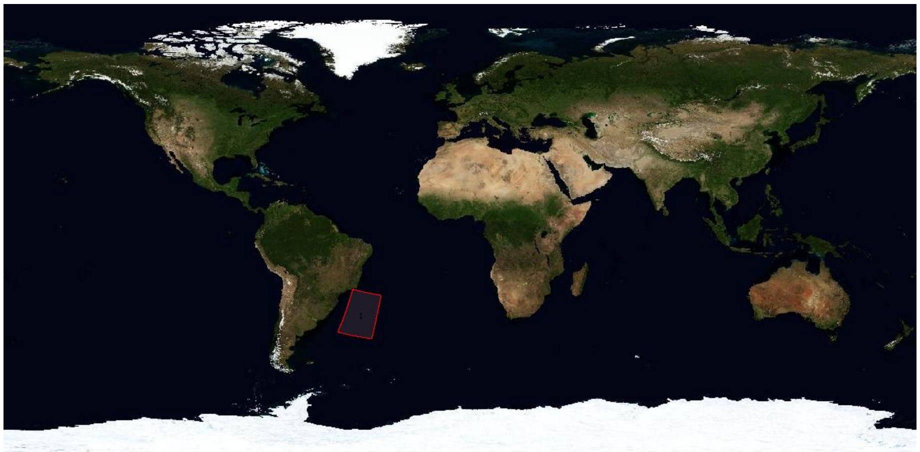

Figure 5.4.1. World map with the region of interest delimited by the red line.

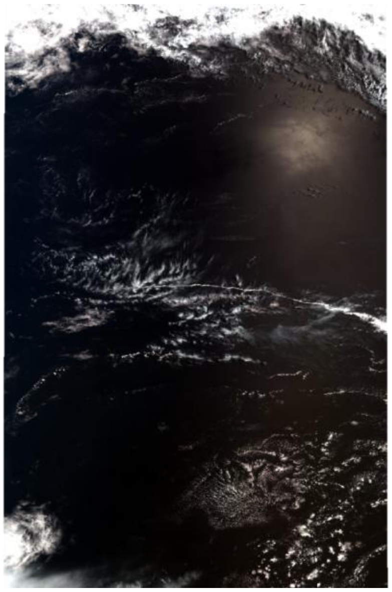

Figure 5.4.2. The region of interest shown in a RGB image.

The MCI image was computed processing MERIS L1b radiance data making use of the Beam MCI L1B processor. The next Figure 5.4.3 shows the MCI image of the swath under investigation.

Figure 5.4.3. MCI image of the region of interest.

The attention was focused on those pixels whose value was exceeding the threshold MCI_{th}. Among these, as shown below, it was possible to detect both false alarms belonging to *case 1* and *case 2*.

The MCI value histogram (see Figure 5.4.4 and 5.4.5) was studied in order to retrieve the threshold. This is equal to the mean value μ plus three times the standard deviation σ of all the valid data set.

As illustrated in Table 5.4.1, the following threshold value resulted:

$$MCI_{th} = -0.59784 + 3*0.391115 = 0.575505.$$

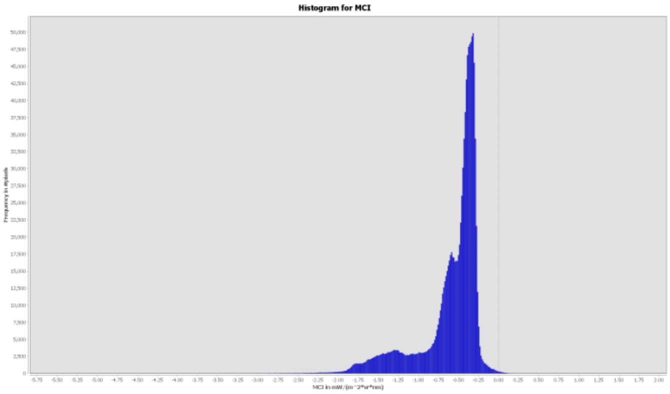

Figure 5.4.4. Histogram of the image obtained only using MCI valid values.

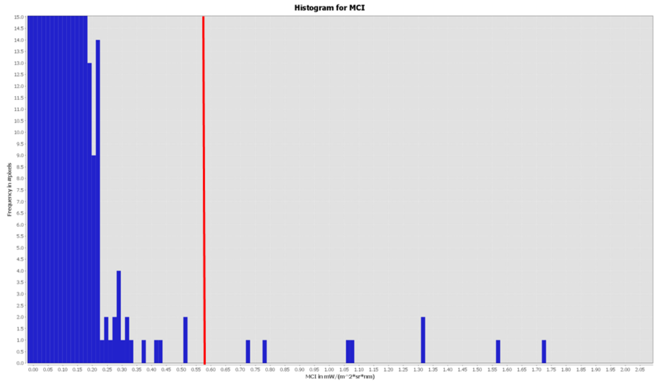

Figure 5.4.5. Ouliers pixels can be seen making a zoom on the right tale of the histogram. The red line indicates the threshold.

ROI-mask name	Only water
Number of pixels total	1848529
Number of considered pixels	1141364
Ratio of considered pixels	61.74445 %
Minimum	-5.47664 mW/(m^2*sr*nm)
Maximum	1.7318 mW/(m^2*sr*nm)
Mean μ	-0.59784 mW/(m^2*sr*nm)
Standard deviation σ	0.391115 mW/(m^2*sr*nm)
Coefficient of variation	-0.65421
Median	-0.45236 mW/(m^2*sr*nm)
P90 threshold	-0.30819 mW/(m^2*sr*nm)
P95 threshold	-0.27935 mW/(m^2*sr*nm)
Threshold MCI_{th} ($\mu + 3\sigma$)	0.575505 mW/(m^2*sr*nm)

Table 5.4.1. Main statistical values of the valid MCI image.

The pixels which exceed the threshold were indicated in the image with some pins and are just a small part of the population of false alarms in retrieving high values of chlorophyll, see Figure 5.4.6.

Eight outliers exceeding were detected in the MCI image and their MCI values and MCI slopes are expressed in Table 5.4.2 together with other parameters such as the latitude and longitude of the pixels to which the pins refer to, the sun zenith and azimuth angles and the sensorzenith and azimuth view.

The following Tables 5.4.3-5.4.10 sumarize the main statistics computed for the mask made of the edge pixels surrounding the one under inspection. Just “valid pixels” were taken into account. Below each table, it is shown the zoomed MCI image in grey scale where it is clearly recognizable the bright pixel (indicated with a pin) caracterized by a high (false) MCI value (the yellow pixels refer to duplicated pixel values).

Figure 5.4.6. MCI image with the pins indicating those pixels over the threshold. In red the pixels flagged as "bright" (clouds) and in yellow the ones "duplicated".

Pin number	Longitude	Latitude	MCI Value	MCI Slope	Sun Zenit	Sun Azimuth	View Zenit	View Azimuth
1	-39,14	-25,46	1,566315	-0,06	30,84	92,08	14,01	103,75
2	-42,43	-25,98	1,311013	-0,06	33,71	92,47	34,94	105,17
3	-38,85	-27,6	0,730349	-0,05	30,46	88,29	7,46	103,54
4	-39,47	-33,05	1,311344	-0,07	31,26	79,35	0,67	51,72
5	-41,82	-33,83	1,077425	-0,05	33,26	79,93	15,79	104,74
6	-32,73	-29,12	0,775869	-0,1	25,21	81,58	37,66	280,59
7	-38,24	-29,34	1,7318	-0,05	29,93	84,88	0,84	310,41
8	-37,52	-29,61	1,068616	-0,06	29,33	83,95	6,87	282,79

Table 5.4.2. Main characteristics of the outlier pins.

- *Pin 1*

ROI-mask name	Around pin 1	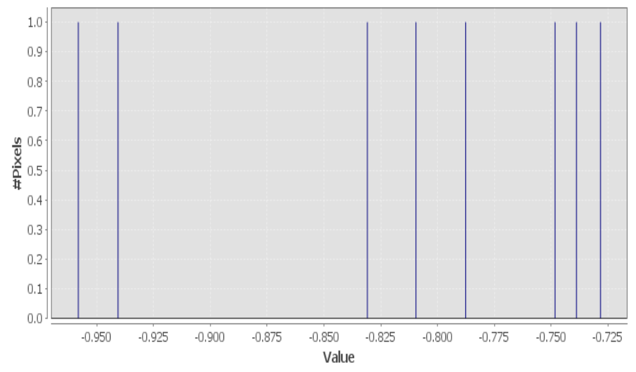
Number of considered pixels	8	
Minimum	-0.95836	
Maximum	-0.72821	
Mean	-0.81785	
Standard deviation	0.088721	
Median	-0.79864	

Table 5.4.3 . Pin 1 surrounding mask description.

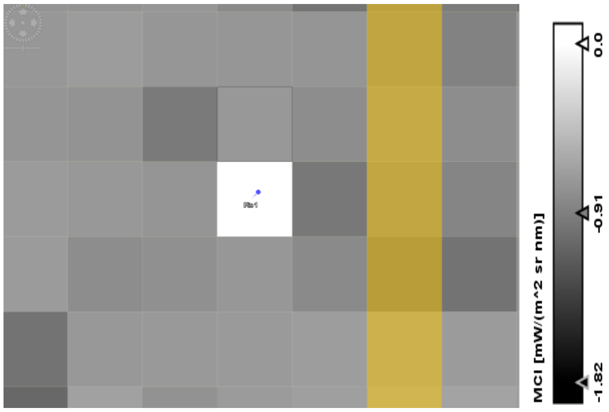

Figure 5.4.7. Grey-scale MCI image obtained zooming in the area around pin 1

(the yellow pixels refer to duplicated pixel values).

- *Pin 2*

ROI-mask name	Around pin 2	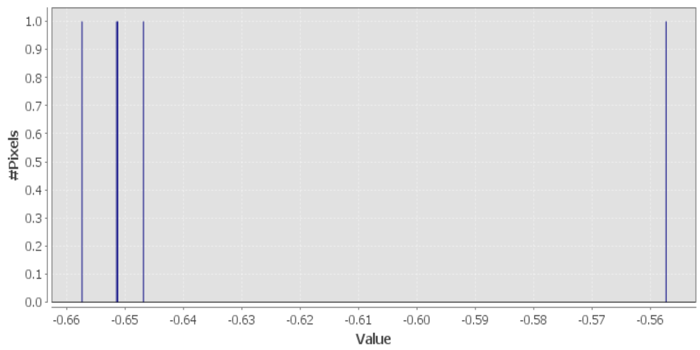
Number of considered pixels	5	
Minimum	-0.65753	
Maximum	-0.55723	
Mean	-0.63292	
Standard deviation	0.042478	
Median	-0.65136	

Table 5.4.4 . Pin 2 surrounding mask description.

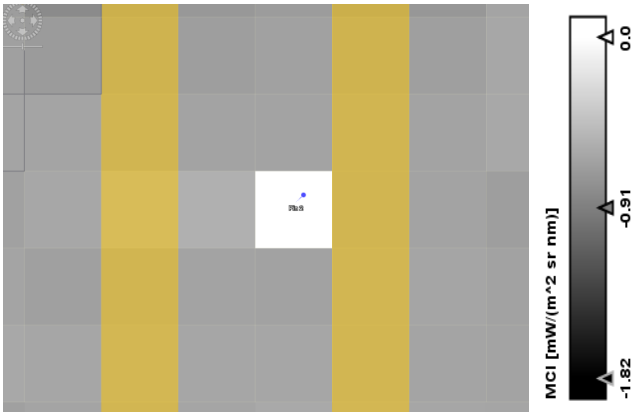

Figure 5.4.8. Grey-scale MCI image obtained zooming in the area around pin 2

(the yellow pixels refer to duplicated pixel values).

- *Pin 3*

ROI-mask name	Around pin 3	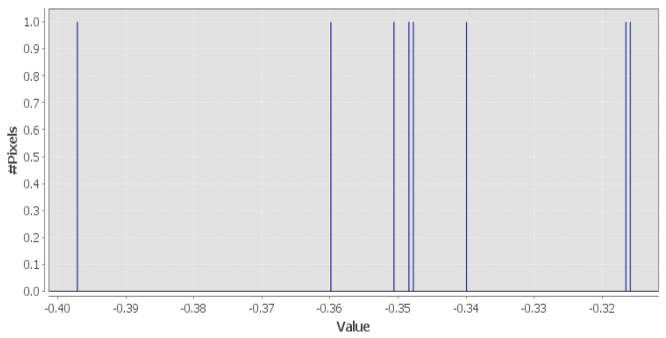
Number of considered pixels	8	
Minimum	-0.39718	
Maximum	-0.31586	
Mean	-0.34703	
Standard deviation	0.025767	
Median	-0.3481	

Table 5.4.5 . Pin 3 surrounding mask description.

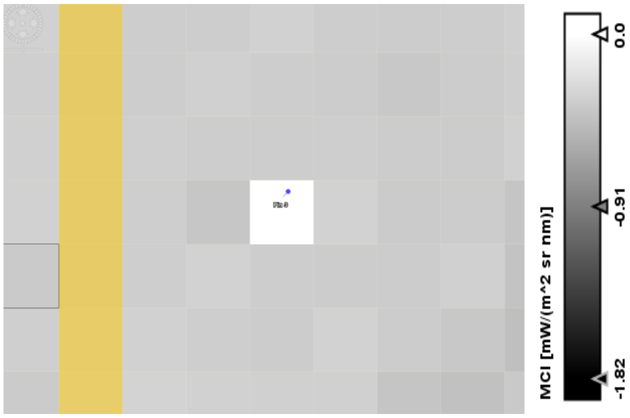

Figure 5.4.9. Grey-scale MCI image obtained zooming in the area around pin 3

(the yellow pixels refer to duplicated pixel values) .

- *Pin 4*

ROI-mask name	Around pin 4	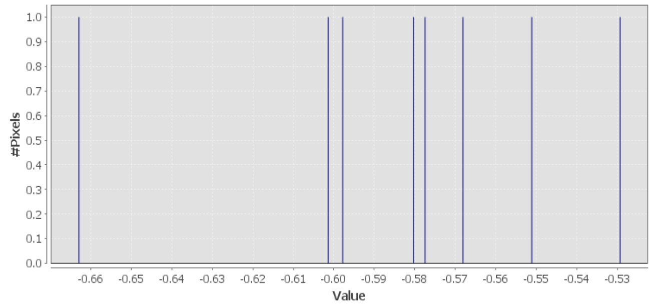
Number of considered pixels	8	
Minimum	-0.66306	
Maximum	-0.52926	
Mean	-0.58358	
Standard deviation	0.039874	
Median	-0.5789	

Table 5.4.6 . Pin 4 surrounding mask description.

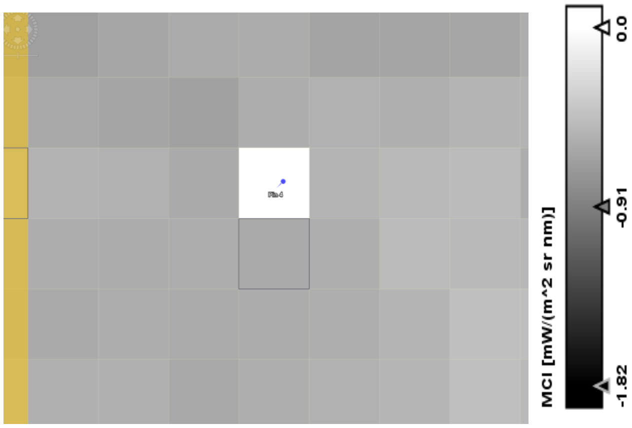

Figure 5.4.10. Grey-scale MCI image obtained zooming in the area around pin 4

(the yellow pixels refer to duplicated pixel values) .

- *Pin 5*

ROI-mask name	Around pin 5	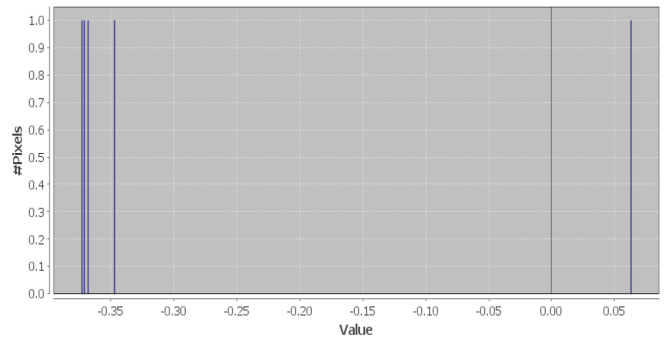
Number of considered pixels	5	
Minimum	-0.37296	
Maximum	0.062998	
Mean	-0.27917	
Standard deviation	0.19156	
Median	-0.36794	

Table 5.4.7 . Pin 5 surrounding mask description.

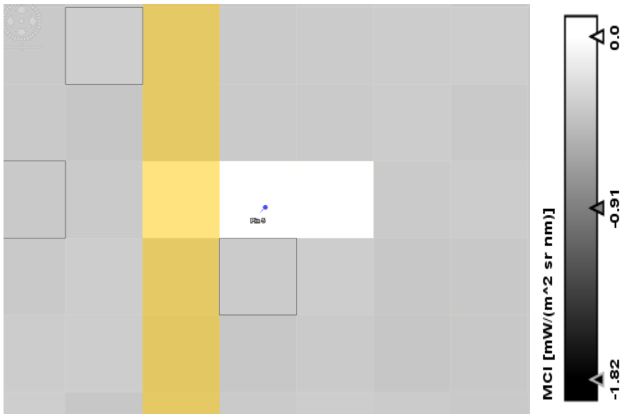

Figure 5.4.11. Grey-scale MCI image obtained zooming in the area around pin 5

(the yellow pixels refer to duplicated pixel values) .

- *Pin 6*

ROI-mask name	Around pin 6
Number of considered pixels	5
Ratio of considered pixels	2.70E-04
Minimum	-1.15717
Maximum	-1.07457
Mean	-1.10118
Standard deviation	0.035061
Median	-1.08288

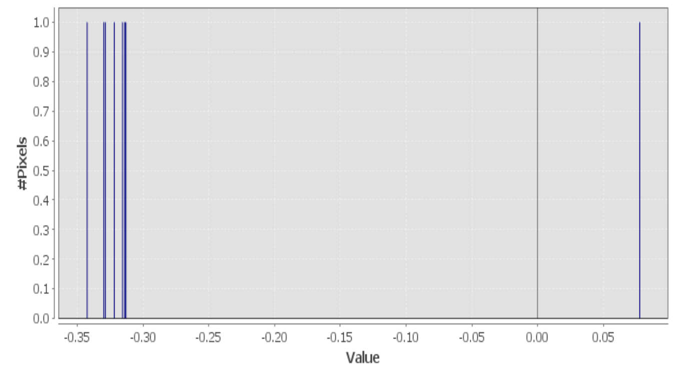

Table 5.4.8 . Pin 6 surrounding mask description.

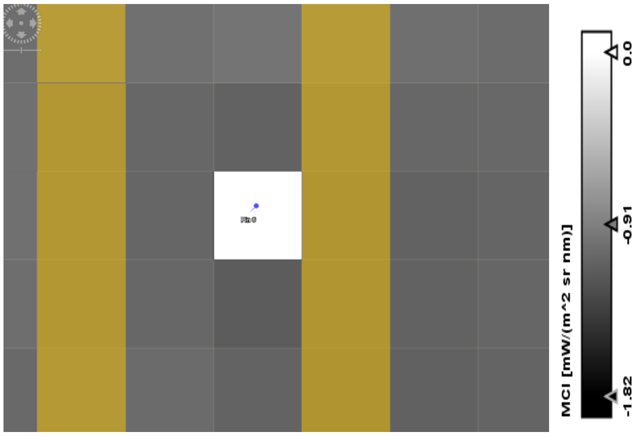

Figure 5.4.12. Grey-scale MCI image obtained zooming in the area around pin 6

(the yellow pixels refer to duplicated pixel values) .

- *Pin 7*

ROI-mask name	Around pin 7	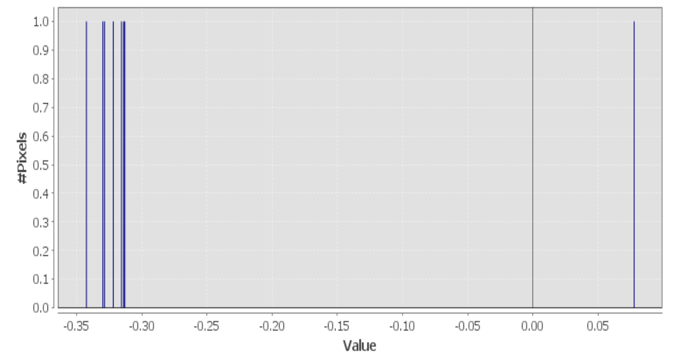
Number of considered pixels	8	
Minimum	-0.34286	
Maximum	0.077691	
Mean	-0.27368	
Standard deviation	0.142327	
Median	-0.31889	

Table 5.4.9 . Pin 7 surrounding mask description.

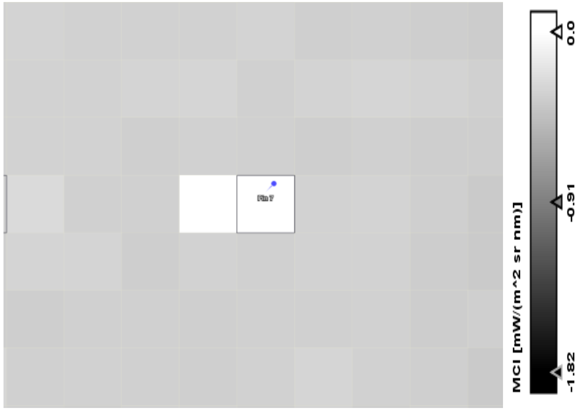

Figure 5.4.13. Grey-scale MCI image obtained zooming in the area around pin 7

(the yellow pixels refer to duplicated pixel values) .

- *<u>Pin 8</u>*

ROI-mask name	Around pin 8
Number of considered pixels	8
Minimum	-0.56883
Maximum	0.189368
Mean	-0.44817
Standard deviation	0.258089
Median	-0.53395

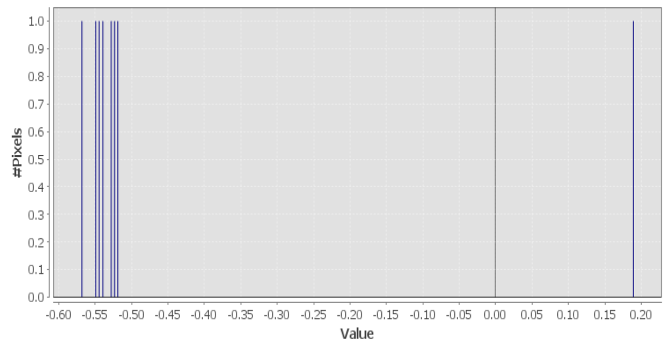

Table 5.4.10 . Pin 8 surrounding mask description.

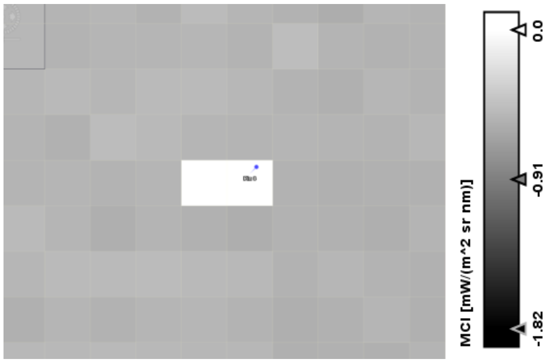

Figure 5.4.14. Grey-scale MCI image obtained zooming in the area around pin 8

(the yellow pixels refer to duplicated pixel values).

Pins number 2, 3, 4, 6, and 7 indicate pixels (just a small part of the entire popultion) whose MCI value was affected by PPE on the corresponding 9th band CCD element, according to *case 1*. It is possible to assert this because the MCI value under test exceeds the mean of the surrounding pixels by more than 0.3 mW/(m^2*sr*nm) and the standard deviation of the same sourrounding pixels is lower than 0.05.

Pins number 1, 5 and 8 indicate three false alarms generated by PPEs according to *case 2*.

The impact of the high energy particle may be observed also analyzing (see Figure *5.4.15*) the TOA radiance spectrum of the pixel under investigation in comparison with the average of the TOA radiance spectrums of the four adjacent pixels (the ones north, south, east and west located in respect to pin 1, for example). The center of the adjacent selected pixels on ground is about 1.2 km far from the center of the considered pixel; the relative distance on the Charged Coupled Device is 4 x 22.5 µm.

As an example, it is shown the spectrum curve of pixel 1 slightly lying below the curve of the edge mean values for all MERIS bands except for band number 9 (708 nm). This is more evident studying the difference between spectrums for pin number 1 TOA radiance and the adjacent pixels mean radiance. The plot in Figure 4.4.16 clearly shows this peak at 708 nm measuring a positive difference of 0.5 mW/(m^2*sr*nm), while for the other wavelengths the same difference is negative.

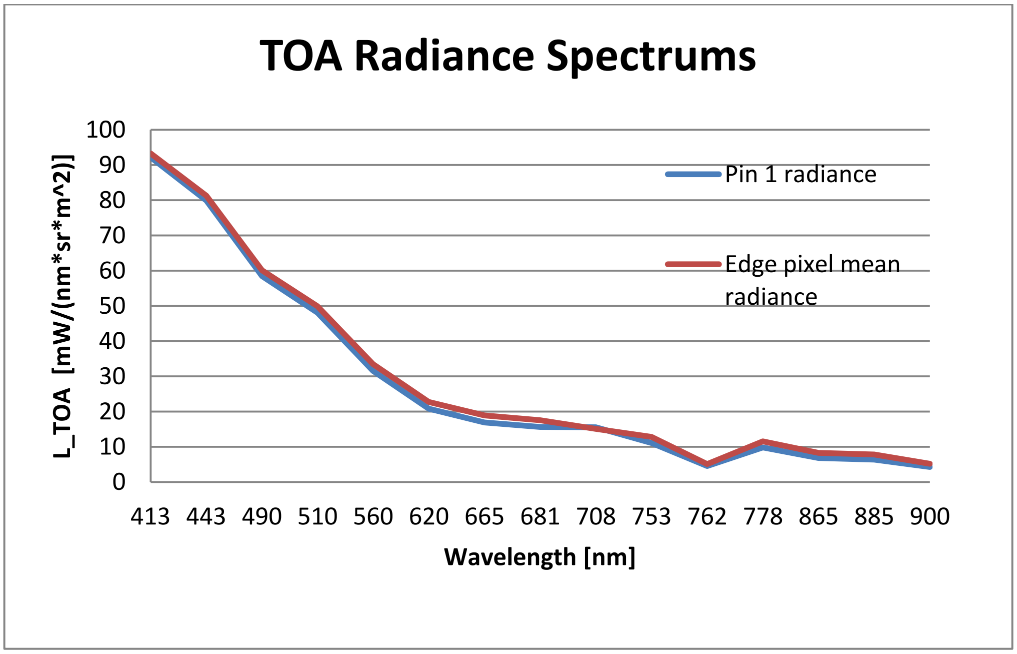

Figure 5.4.15. TOA radiance spectrums for pixel 1 and the mean TOA radiance spectrum of the surrounding adjacent pixels for the 15 MERIS bands.

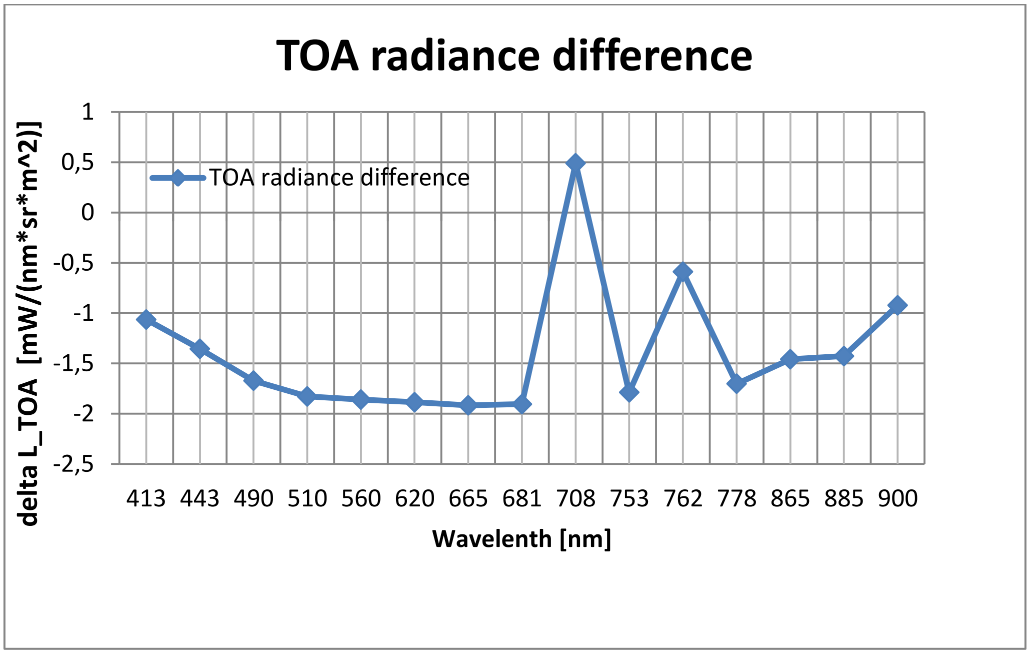

Figure 4.4.16. Difference between the curves plotted in the previous figure (5.4.15), i.e., the TOA radiance of pixel 1 minus the mean TOA radiance spectrum of the surrounding adjacent pixels.

5.5 Validation

In order to validate the above MERIS data retrieved analysis results, data from the MODIS (Moderate Resolution Imaging Spectroradiometer) [28] were used. For this obersation data using the same swaths and days in which MERIS acquired the data previously processed with the MCI algorithm were used to validate the results reported in the previous paragraph for *case 2*.

MODIS is on board of NASA’s AQUA and TERRA satellites. Level 2 MODIS data contain estimates of chlorophyll *a* concentration obtained through the application of a standard algorithm, the so-called OC3M [29]. The algorithm is an empirical equation relating remote sensing water leaving reflectances, R_{rs}, to chlorophyll *a* concentration.

The relation between chlorophyll *a* (C_a) and the water leaving reflectance (R_{3m}) is expressed as follows:

$$C_a = 10^{(0.2830 - 2.753 R_{3M} + 1.457 R_{3M}^2 + 0.659 R_{3M}^3 - 1.403 R_{3M}^4)},$$

where $R_{3M} = max\left\{log_{10}\left(R_{550}^{443}\right),\ log_{10}\left(R_{550}^{490}\right)\right\}$ and $R_{\lambda\,\mathrm{i}}^{\lambda\,\mathrm{j}} = \frac{R(\lambda\,\mathrm{i})}{R(\lambda\,\mathrm{j})}$.

MODIS bands centered at 443 nm, 490 nm and 550 nm are respectively MODIS bands number 9, 10 and 12, as shown in the Table 5.5.1 below. The spatial resolution for MODIS bands number 9, 10 and 12 is 1000 m.

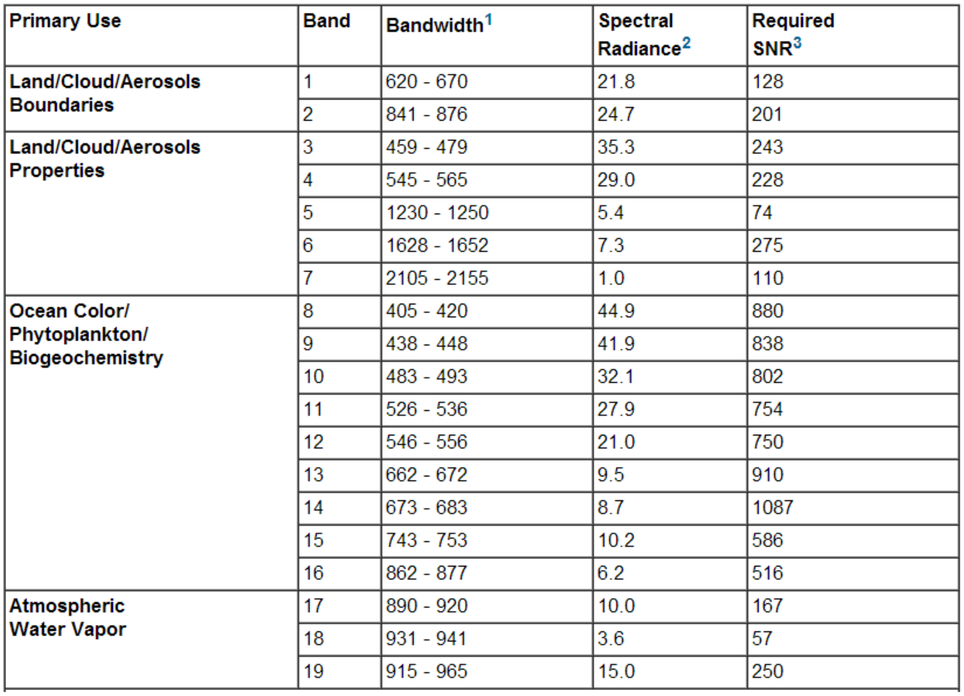

Primary Use	Band	Bandwidth[1]	Spectral Radiance[2]	Required SNR[3]
Land/Cloud/Aerosols Boundaries	1	620 - 670	21.8	128
	2	841 - 876	24.7	201
Land/Cloud/Aerosols Properties	3	459 - 479	35.3	243
	4	545 - 565	29.0	228
	5	1230 - 1250	5.4	74
	6	1628 - 1652	7.3	275
	7	2105 - 2155	1.0	110
Ocean Color/ Phytoplankton/ Biogeochemistry	8	405 - 420	44.9	880
	9	438 - 448	41.9	838
	10	483 - 493	32.1	802
	11	526 - 536	27.9	754
	12	546 - 556	21.0	750
	13	662 - 672	9.5	910
	14	673 - 683	8.7	1087
	15	743 - 753	10.2	586
	16	862 - 877	6.2	516
Atmospheric Water Vapor	17	890 - 920	10.0	167
	18	931 - 941	3.6	57
	19	915 - 965	15.0	250

*Table 5.5.1. MODIS bands in the Visible and Near InfraRed. [1]The bandwidth is expressed in nm. [2]The spectral radiance is expressed in mW/(sr*m^2*nm). [3]SNR stands for Signal to Noise Ratio [30].*

It needs to be mentioned that MODIS-OC3M algorithm makes use of different spectral bands, when compared to the MERIS-MCI algorithm. MCI uses the spectral band centered at 708 nm over a baseline passing through the two bands centered at 680 and 750 nm. Indeed the MCI index was used to detect cosmic rays hitting the CCD on MERIS band number 9 (708 nm). None of the MODIS bands used for OC3M match with those used for MERIS MCI.

The MODIS L2 data were downloaded from *oceancolor.gsfc.nasa.go/cgi/browse.pl* website, red and processed with the open source SeaDAS (Sea WiFS Data Analysis Software, later adapted in version 7.0.2 also for reading and processing MODIS data).

The files inspected are listed below:

- *A2003342161500.L2_LAC_OC;*
- *A2004283160500.L2_LAC_OC;*
- *A2005032163500.L2_LAC_OC;*
- *A2006115163500.L2_LAC_OC;*
- *A2007015163000.L2_LAC_OC;*
- *A2008107162500.L2_LAC_OC;*
- *A2009024161000.L2_LAC_OC.*

Next, it is shown all the false alarms associated to those MCI pixel values detected according to *case 2* (i.e. those respecting condition *a)* of *case 1* and having an MCI value greater than the aforementioned MCI_{th}) in the first MERIS inspected file (ME*R_RR__ 1PRBCM20031208_ 121250_ 000002902022_ 00195_ 09267_ 0002.N1*) to the chlorophyll *a* values contained in MODIS L2 data related to the same sensing day. This was possible wherever MODIS pixels on ground were not coverd by clouds.

The first inspected MODIS file is the follwing:

- *2003342161500.L2_LAC_OC.*

MERIS start sensing time: 08 December 2003, 12:12:50.

MODIS start sensing time: 08 December 2003, 16:40:00.

At next stage, MODIS products are compared to the respective MERIS products, for pixels 1, 5 and 8.

- *Pixel 1*

Pixel 1 informations (MERIS)							
Longitude	Latitude	MCI Value	DEM altitude	Sun zenith	Sun azimuth	View zenith	View azimuth
-39,14	-25,46	1,566	-3885	30,8	92,1	14,0	103,8

Table 5.5.2. MERIS pixel 1 main informations.

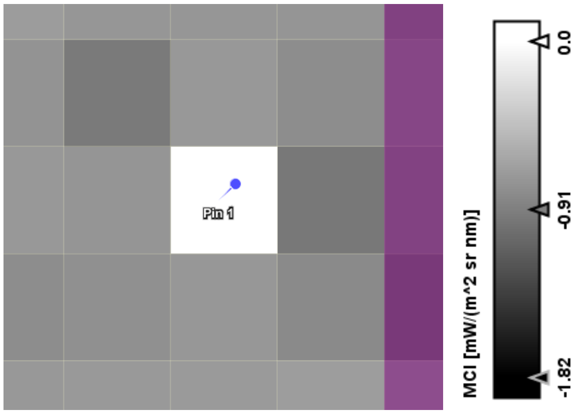

Figure 5.5.1. MERIS MCI image of pixel 1 and surrounding ones

(in purple duplicated values).

Mask surrounding outlier pixel 1 (MERIS)	
Number of considered edge pixels	8
Minimum [mW/(m^2*sr*nm)]	-0,95836
Maximum [mW/(m^2*sr*nm)]	-0,72821
Mean [mW/(m^2*sr*nm)]	-0,81785
Standard deviation [mW/(m^2*sr*nm)]	0,088721

Table 5.5.3. *Surrounding MERIS pixel 1 mask statistics.*

Pixel 1 informations (MODIS)	
Product	2003A2013342164000
Longitude	39°06'49" W
Latitude	25°27'44" S
Rrs@443 nm [sr^-1]	0,011396 sr^-1
Rrs@488 m [sr^-1]	0,007284 sr^-1
Rrs@547 nm [sr^-1]	0,001856 sr^-1
Chlor *a* [mg m^-3]	0,053 mg m^-3

Table 5.5.4. *MODIS pixel 1 main informations.*

Surrounding pixel 1 chlorophyll *a* pixel values (MODIS)	
Adjacent pixel location	Chlorophyll a concentration [mg m^-3]
North	0.059128
Nort-East	0.058864
East	0.05331
South-East	0.047123
South	0.059128
South-West	0.061329
West	0.052799
North-West	0.064615

Table 5.5.5*. Surrounding pixel 1 chlorophyll a values (MODIS).*

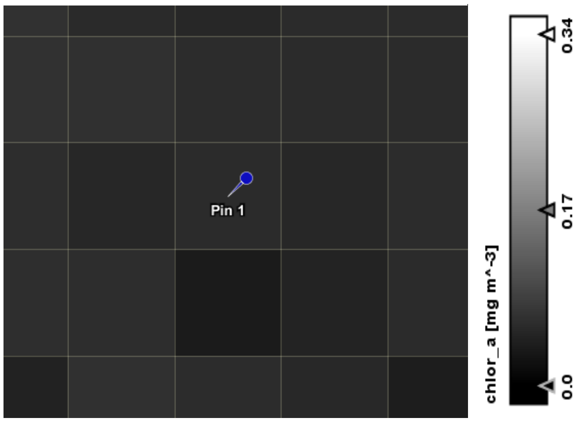

Figure 5.5.2 *MODIS chl-a image in grey-scale* *zooming in the area around pixel 1.*

- *<u>Pixel 5</u>*

Pixel 5 informations (MERIS)							
Longitude	Latitude	MCI Value	DEM altitude	Sun zenith	Sun azimuth	View zenith	View azimuth
-41.83	-33.84	1.077	-4580	33.27	79.94	15.79	104.74

Table 5.5.6. *MERIS pixel 5 main informations.*

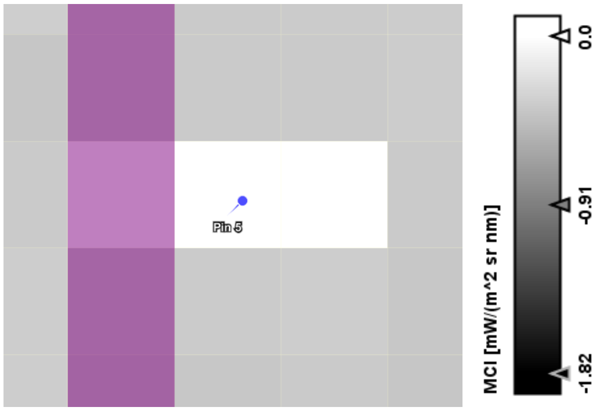

Figure 5.5.3. MERIS MCI image of pixel 5 and surrounding ones

(in purple duplicated values).

Mask surrounding pixel 5 (MERIS)	
Number of considered edge pixels	5
Minimum [mW/(m^2*sr*nm)]	-0.3729
Maximum [mW/(m^2*sr*nm)]	0.0629
Mean [mW/(m^2*sr*nm)]	-0.2792
Standard deviation [mW/(m^2*sr*nm)]	0.19156

Table 5.5.7. Surrounding MERIS pixel 5 mask statistics.

Pixel 5 informations (MODIS)	
Product	2003A2013342164000
Longitude	-41.49
Latitude	-33.49
Rrs@443 nm [sr^-1]	0.00668
Rrs@488 m [sr^-1]	0.00504
Rrs@547 nm [sr^-1]	0.00113
Chlor *a* [mg m^-3]	0.058988

Table 5.5.8. MODIS pixel 5 main informations.

Surrounding pixel 5 chlorophyll *a* values (MODIS)	
Adjacent pixel location	Chlorophyll a concentration [mg m^-3]
North	0.077804
Nort-East	0.069507
East	0.061631
South-East	0.046669
South	0.046605
South-West	0.047082
West	0.071513
North-West	Not valid value

Table 5.5.9. Surrounding pixel 5 chlorophyll a values (MODIS).

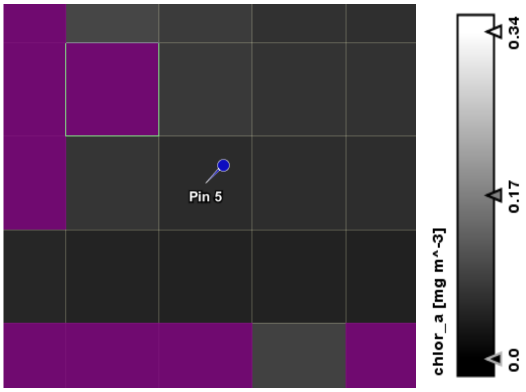

Figure 5.5.4. *MODIS chl-a image in grey-scale zooming in the area around pixel 5 (in purple high or saturating TOA radiance).*

- *Pin 8*

Pixel 8 informations (MERIS)							
Longitude	Latitude	MCI Value	DEM altitude	Sun zenith	Sun azimuth	View zenith	View azimuth
-38,24	-29,34	1,7318	-0,05	29,93	84,88	0,84	310,41

Table 5.5.10. MERIS pixel 8 main informations.

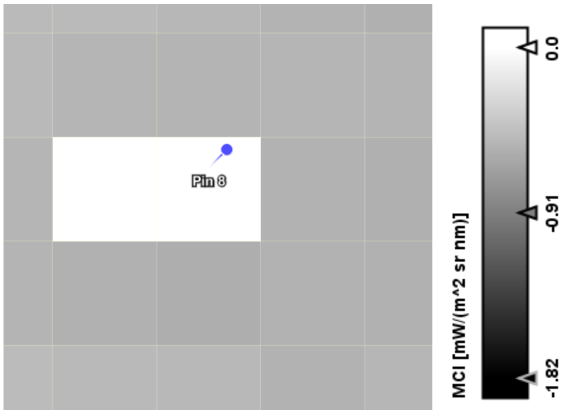

Figure 5.5.5. MERIS MCI image of pixel 8 and surrounding ones

(in purple duplicated values).

Mask surrounding pixel 8 (MERIS)	
Number of considered edge pixels:	8
Minimum: [mW/(m^2*sr*nm)]	-0,5688
Maximum: [mW/(m^2*sr*nm)]	0,1894
Mean: [mW/(m^2*sr*nm)]	-0,4482
Standard deviation: [mW/(m^2*sr*nm)]	0,2581

Table 5.5.11. *Surrounding pixel 8 mask statistics.*

Pixel 8 informations (MODIS)	
Product	2003A2013342164000
Longitude	37°31'38" W
Latitude	29°36'55" S
Rrs@443 nm [sr^-1]	0.0096
Rrs@488 m [sr^-1]	0.0062
Rrs@547 nm [sr^-1]	0.0014
Chlor *a* [mg m^-3]	0.0436

Table 5.5.12. Surrounding MERIS pixel 8 mask statistics.

Surrounding pixel 8 chlorophyll *a* values (MODIS)	
Adjacent pixel location	Chlorophyll a concentration [mg m^-3]
North	0.05307421
Nort-East	0.06052298
East	0.04354695
South-East	0.058265936
South	0.0784116
South-West	0.06443726
West	0.06076408
North-West	0.053416647

Table 5.5.13. Surrounding pixel 8 chlorophyll a values (MODIS).

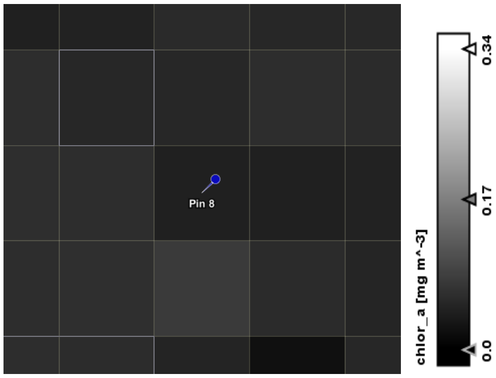

Figure 5.5.6. *MODIS chl-a image in grey-scale zooming in the area around pixel 5.*

The same kind of analysis was done for all the aforementioned MODIS files (page 111) to and similar results were obtained, confirming the validity of the algorithm to detect PPEs false alarms pixels in MCI images.

In all the analyzed cases, according to MODIS OC3M algorithm, the central pixel does not show a concentration value of chlorophyll *a* significantly higher than the surrounding ones. Furthermore, all *chl a* values estimated by MODIS, including the central pixel, are in line with the values estimated by MERIS for the surrounding pixels, except, whenever found, the brighter ones, which most likely feel the effect of the same PPE causing the false alarm in the central pixel. This event corrupts the adjacent across-track pixel, as explained in Chapter 2, thus, when these brighter pixels appear, they lie on the right or left to the detected false alarm.

Chapter 6. Assessment of PPEs during OLCI preflight testing and prediction of OLCI in-flight sensitivity

In this chapter an analysis of test measurement data acquired during the OLCI on-ground test campaign related to the occurrence of PPEs will be provided. For this, the OLCI dark signal measurements and the occurrence of PPEs are analyzed in function of surface and time. This will help to predict the effects of such radiation on the CCD once in orbit in terms of pixel sensitivity. Later in the chapter, it will be given a prediction of OLCI in-flight sensitivity to PPE occurrences.

6.1 OLCI Test configuration for camera 1 – 5

In order to analyze the influence of cosmic rays on the dark signal read out at the VAM output the following approach was used.

Dark signal data provided by Thales Alenia Space and acquired by the five S3/OLCI cameras during AIT (Assembly, Integration and Test) activities in 2013 and 2014 in Cannes [31-35] were used. The impact of energetic particles was studied in order to understand their effects on ground on the whole video chain and to compare these results with previous and future models' results and with the previous analysis done for Envisat/MERIS once in space (approx. 790 km).

All five cameras are composed of the Camera Optical Sub Assembly (COSA) equipped with the Focal Plane Assembly (FPA), coupled to the Video Acquisition Module (VAM).

For the darkness measurements, 1000 non-averaged frames were collected. Minimum, medium and maximum gains were applied for each microband (see Table 6.1.1 for the description of all gains G0, G4 and G7). As band setting the AIT band configuration and related micro-bands were used as listed in Table 6.1.2.

FM typical gain	G0	G1	G2	G3	G4	G5	G6	G7
[V/V]	1.4763	1.77156	2.12587	2.55105	3.06126	3.67351	4.40821	5.28985

Table 6.1.1. *Flight model typical gains. It is basically the G0 value times 1.2 = G1, G1*1.2=G2 and so on [36].*

For each camera and for each gain, the dark mean value and the dark standard deviation were computed over 33.93e6 samples (754 spatial pixels, 45 microbands and 1000 frames). The OLCI acquisition microbands are numbered from 1 to 46 in the decreasing order of the center wavelength (check Table 6.1.2). Microband number 1 corresponds to the last smear micro band (Table 6.1.2). The reverse order comes from the projection of spectral bands on the CCD: the highest spectral band is read first by the VAM.

In order to detect the occurrences related to energetic particles striking on the CCD surface, a threshold was chosen. To be in line with previous analysis, the selected threshold is equal to the dark signal microband mean value plus 5 times the dark standard deviation. In this way it was possible to determine the maximum and the mean LSB value of the affected samples rays and the percentage of occurrences. This was done for all five cameras depending on the three different gains (except for camera 1 where the file referring to Gain 0 was missing).

The test conditions are described in Appendix B for each camera module and dark signal main statistics, number of occurrences and affected pixels are reported in detail per each camera and gain.

The results are expressed in terms of LSBs. As already mentioned, in contrast to MERIS, OLCI uses a 14-bit ADC (instead of 12).

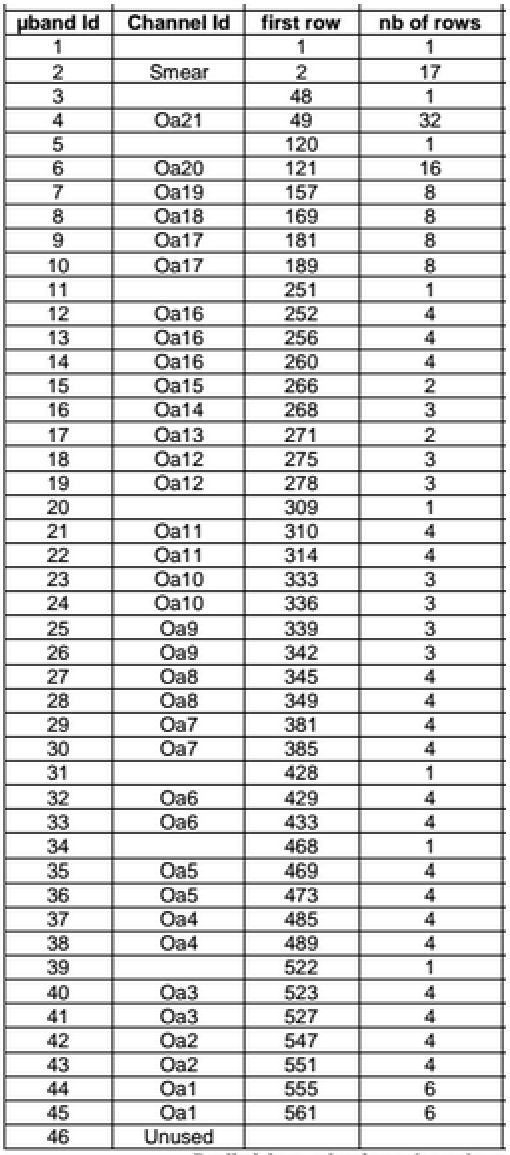

µband Id	Channel Id	first row	nb of rows
1		1	1
2	Smear	2	17
3		48	1
4	Oa21	49	32
5		120	1
6	Oa20	121	16
7	Oa19	157	8
8	Oa18	169	8
9	Oa17	181	8
10	Oa17	189	8
11		251	1
12	Oa16	252	4
13	Oa16	256	4
14	Oa16	260	4
15	Oa15	266	2
16	Oa14	268	3
17	Oa13	271	2
18	Oa12	275	3
19	Oa12	278	3
20		309	1
21	Oa11	310	4
22	Oa11	314	4
23	Oa10	333	3
24	Oa10	336	3
25	Oa9	339	3
26	Oa9	342	3
27	Oa8	345	4
28	Oa8	349	4
29	Oa7	381	4
30	Oa7	385	4
31		428	1
32	Oa6	429	4
33	Oa6	433	4
34		468	1
35	Oa5	469	4
36	Oa5	473	4
37	Oa4	485	4
38	Oa4	489	4
39		522	1
40	Oa3	523	4
41	Oa3	527	4
42	Oa2	547	4
43	Oa2	551	4
44	Oa1	555	6
45	Oa1	561	6
46	Unused		

Table 6.1.2. Sentinel-3/OLCI spectral band description [37].

For all OLCI cameras 1-5 the dark signal mean value recorded at the VAM output for each gain and camera varies in a range between 37.7 and 39.9 LSBs. The mean value was computed over all the pixels, including those with defects, i.e. cold and hot pixels, and those whose value was influenced by an energetic particle striking on the CCD under test.

Using a threshold equal to the dark microband mean value plus 5 times the standard deviation, as expected, several spikes due to prompt particle events were detected. They appear only in 1 frame from the 1000 acquired per each pixel. In ambient pressure (CCD temperature regulated at +17°C), on average, pixels affected by cosmic rays may vary from 50 LSBs (camera PFM2, Gain 0) up to 85 LSBs (camera PFM2, Gain 7). In vacuum (CCD temperature regulated at -22.5°C), on average, the affected pixels may vary from 55 LSBs (camera PFM2, Gain 0) up to 104 LSBs (camera PFM2, Gain 7).

The results are summarized in Figures 6.1.1-6.1.5. In those figures, also the maximum value referred to a spike for each gain is provided.

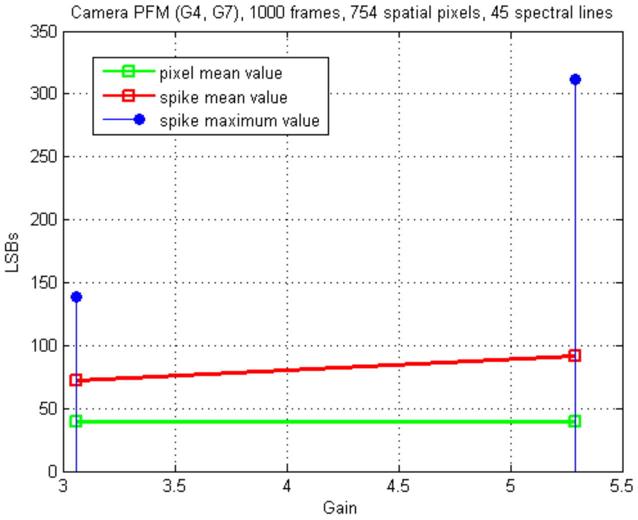

Figure 6.1.1. Pixel mean value, spike mean value and spike maximum value

for Camera PFM during OLCI ground tests.

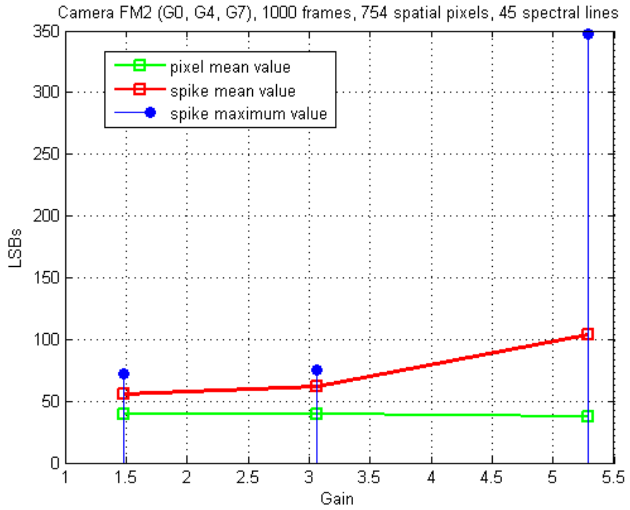

Figure 6.1.2. Pixel mean value, spike mean value and spike maximum value for Camera FM2 during OLCI ground tests.

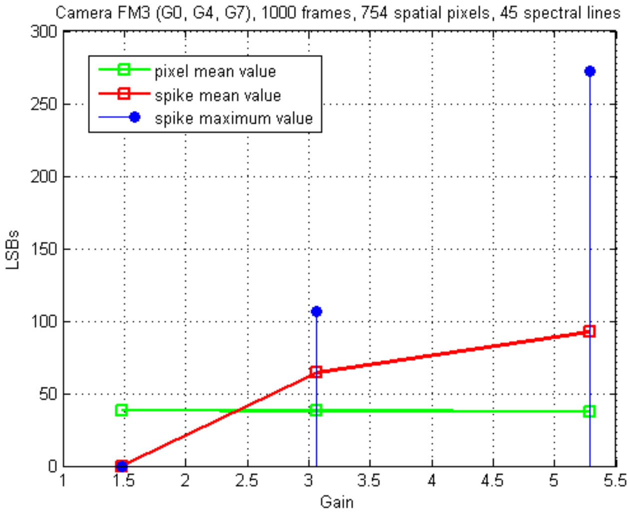

Figure 6.1.3. Pixel mean value, spike mean value and spike maximum value for Camera FM3 during OLCI ground tests.

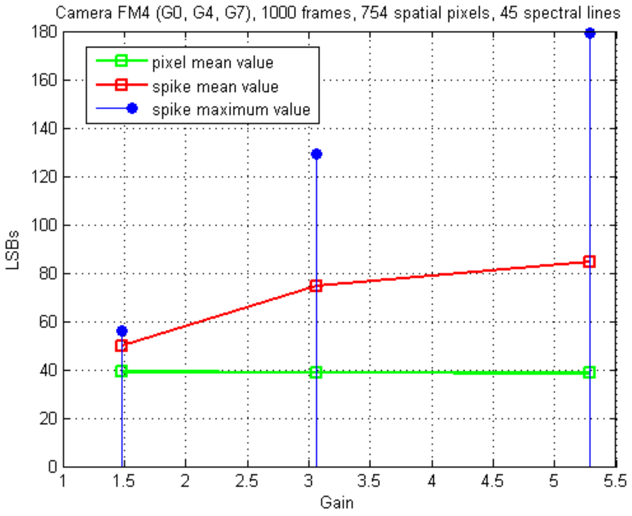

Figure 6.1.4. Pixel mean value, spike mean value and spike maximum value for Camera FM4 during OLCI ground tests.

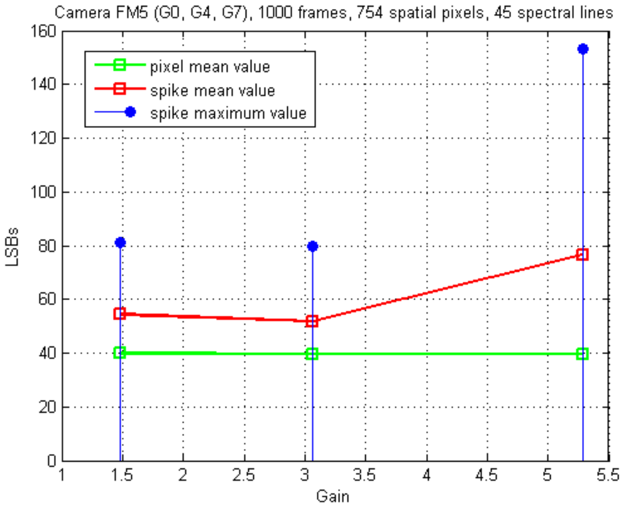

Figure 6.1.5. Pixel mean value, spike mean value and spike maximum value for Camera F5M during OLCI ground tests.

6.2 OLCI camera 1 – 5 on-ground PPE occurrence analysis

In order to further analyze the AIT measurement data, the mean pixel level signal was subtracted from the mean spike level for all OLCI cameras (1 – 5). This was done for all the cameras and for the three different gains, whenever the occurrence of spikes was detected. Taking into account the five cameras, for G0 such difference was less or equal than 15 LSBs for G0, 36 for G4 and 66 LSBs for G7, see Figure 6.2.1.

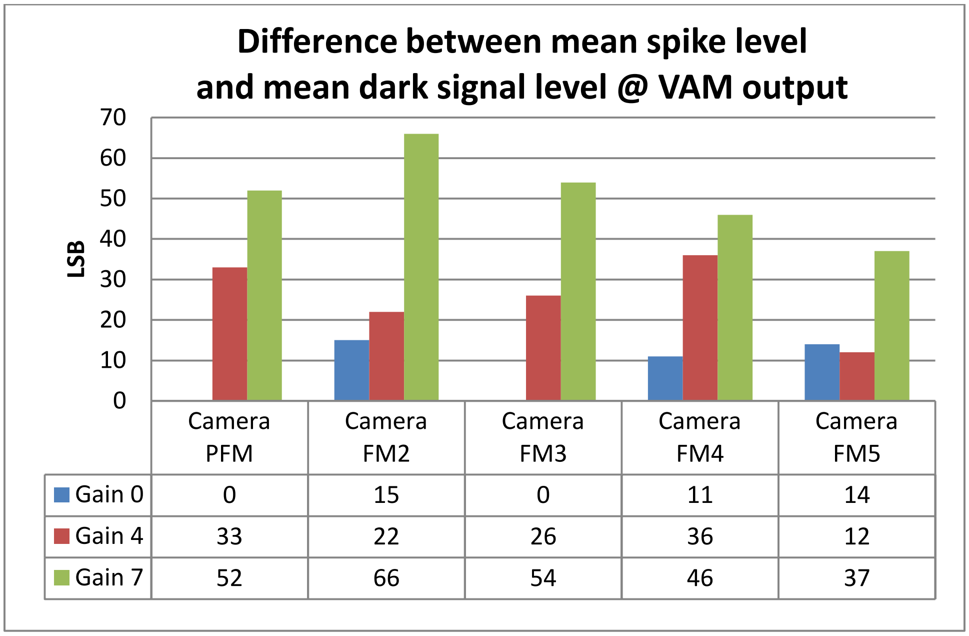

	Camera PFM	Camera FM2	Camera FM3	Camera FM4	Camera FM5
🟦 Gain 0	0	15	0	11	14
🟥 Gain 4	33	22	26	36	12
🟩 Gain 7	52	66	54	46	37

Figure 6.2.1. Difference between mean spike level and mean dark signal level at VAM output during OLCI on-ground tests.

Afterward, the difference between the maximum spike and the mean pixel value was computed for the three gains and the five cameras. Such difference reaches 41 LSBs for G0, 100 for G4 and 309 for G7, see Figure 6.2.2.

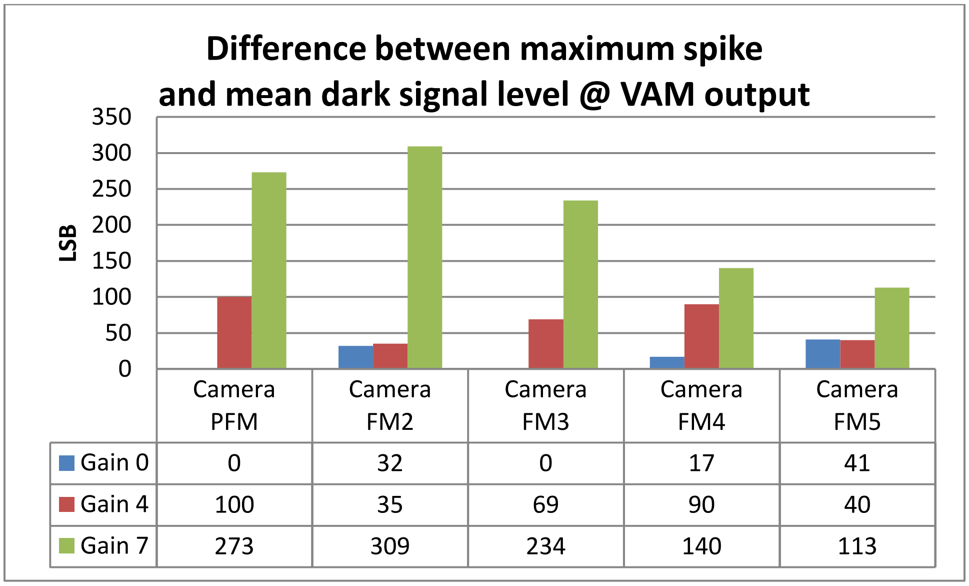

	Camera PFM	Camera FM2	Camera FM3	Camera FM4	Camera FM5
🟦 Gain 0	0	32	0	17	41
🟥 Gain 4	100	35	69	90	40
🟩 Gain 7	273	309	234	140	113

Figure 6.2.2. Difference between maximum spike and mean dark signal level at VAM output during OLCI on-ground tests.

The analysis allowed to make an estimation of the on-ground per-microband element occurrence probability (the location where the test was executed is approximately 43.3°N and 7.0°E). This is in the order of 10^-7. The results are presented in Figure 6.2.3.

Considering the total surface of the CCD occupied by the 45 microbands (218 elementary spectral lines x 754 horizontal pixels x 22.5^2 μm^2 pixel surface), it is possible to estimate the number of energetic particles striking on ground per cm^2 per second. This was done in the case of Gain 0 (averaging the number of PPEs detected for cameras FM2, FM3, FM4 and FM5 over 1000 frames, that is 4 PPEs per camera module over 1000 acquisition frames). Whenever in the same frame and microband two adjacent pixels were both exceeding the threshold, the double occurrence was considered caused by a single PPE. Thus, the number amounts to 1.09 PPEs per cm^2 per second (that is 4 PPEs / CCD surface / (integration time * 1000 frames), corresponding to 6.64 x 10^-9 cosmic rays per elementary CCD pixel element per integration time.

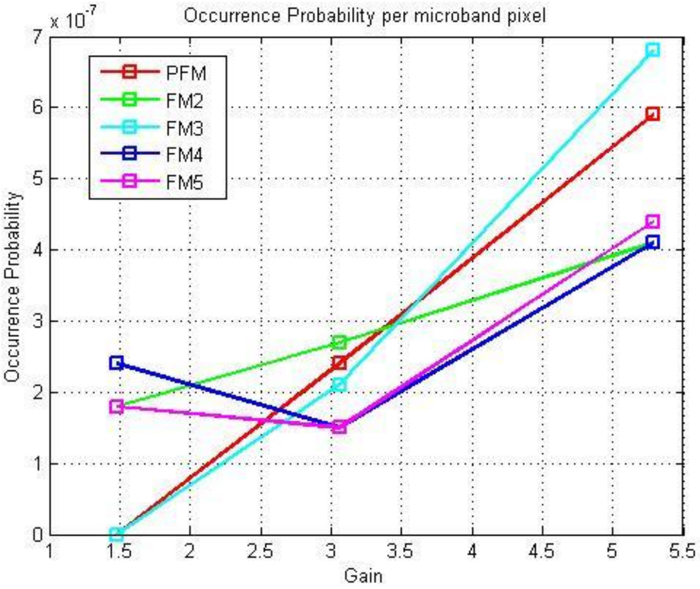

Figure 6.2.3. Estimation of the occurrence probability per microband pixel

for the five cameras obtained using OLCI on-ground test data.

6.3 Prediction of OLCI in-flight sensitivity to PPEs

A prediction of OLCI in-flight sensitivity will allow to retrieve an estimate about how many, how much and how often pixels are affected due to PPEs striking the camera's CCD during the operational phase. This will then allow to understand the influence on top-of-the-atmosphere radiance in level 1B Sentinel-3/OLCI product which then can be an important input to analyze the noise generated in higher-level products through PPEs.

A simplified model was set up to make use of the analysis results of MERIS L0 data acquired during Envisat commissioning phase (see chapter 3).

It needs to be reminded that OLCI, in respect to MERIS, will always operate in full spatial resolution over both land and water (at later stages, from level-1B on, OLCI products will be also at reduced resolution averaging the signal of 16 FR pixels, that is four adjacent pixels across track for four successive lines along track) thus suffering more from PPEs.

The two input values of the prediction model are the mean MERIS LSB value of the RR pixels affected by PPEs (171.2 LSBs) and the mean signal value (151.5 LSBs) of MERIS observation bands, according to the results obtained in Chapter 3 (Figure 3.4.1).

Using this difference in LSBs, the additional number of electrons ΔN^e generated through a PPE in the corrupt RR pixel of the CCD can be calculated.

This will allow to calculate the spectral irradiance $\Delta E^{det}(\lambda)$ at the detector surface. The assumption here is the fact that a PPE is generating for all spectral wavelength the same energy on the CCD (since the PPE will not strike through the optics the CCD). The corresponding TOA radiance mean error ε_L is retrieved for a FR pixel for three particular wavelengths because the energy equal to one PPE is slightly different to the same energy retrieved through the nominal TOA signal (here the signal is created through the Earth scene's photons passing the optics).

Since it can be assumed that OLCI and MERIS CCDs (equal design, e.g., silicon depletion layer thickness) are of same material, the energy generated on CCD level for a single PPE can be also regarded as similar.

The difference ΔLSB^{RR} between the mean level of the affected pixels and the mean pixel level is calculated (19.7 LSBs).

Considering MERIS instrument specifications (12 bits quantization, 4096 steps and shift register capacity of 2.5M electrons), the single quantization step (i.e. 1 LSB) capacity reaches 600 electrons. So, it is possible to derive the corresponding mean number of electrons ΔN^e generated on the related CCD surface by the PPE as expressed in the next equation:

$$\Delta N^e = 600\,\Delta LSB^{RR}$$

Knowing ΔN^e, it is possible to calculate the corresponding spectral irradiance at the RR detector surface $\Delta E^{det}(\lambda)$, making use of the following formula:

$$\Delta E^{det}(\lambda) = \frac{h\,c}{\lambda}\frac{\Delta N^e}{QE^{det}(\lambda)\;A^{det}\,T_{int}\,\Delta\lambda}$$

where QE^{det} represents the quantum efficiency of the detector at the specific central wavelength λ, A^{det} the surface occupied by the RR pixel under question, T_{int} the integration time, $\Delta\lambda$ the spectral bandwidth, *h* the Planck's constant and *c* the velocity of light.

Then, the mean TOA radiance error $\varepsilon_L(\lambda)$ occurring in the affected RR pixels by a PPE can be calculated as follows:

$$\varepsilon_L(\lambda) = \frac{\pi}{4}\,\Delta E^{det}(\lambda)\,T^{objective}(\lambda)\,T^{grating}(\lambda)F\#^2$$

being $T^{objective}$ the transmission coefficient of the camera objective, $T^{grating}$ the grating efficiency and $F\#$ the inverse of MERIS *f*-number.

In the prediction model, three different quantities that depend on the wavelength appear: these are the quantum efficiency, the transmission coefficient and the grating. Three different values per each quantity were used sampling the three curves (plotted in Figure 6.3.1) 412 nm, 510 nm and 778.5 nm (corresponding to three typical OLCI spectral bands, the blue, the green and the red, i.e. Oa2, Oa5 and Oa16).

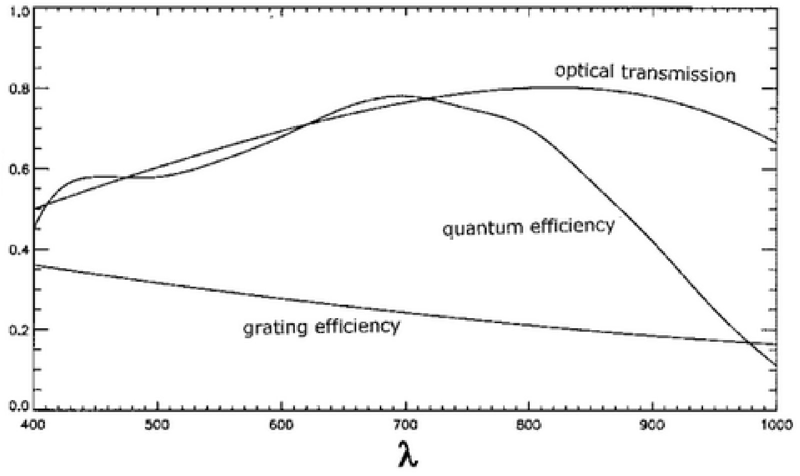

Figure 6.3.1 Quantum efficiency, transmission coefficient

and grating efficiency curves.

Three different results of $\varepsilon_{\mathrm{L_{TOA}}}(\lambda)$ were obtained (see Table 6.3.1), making use of a 10 nm large bandwidth and knowing that the integration time T_{int} equals 44 ms, the *f*-number 10, the detector surface A^{det} 8.1 x 10^-9 m^2.

λ [nm]	$\mathrm{T}^{\mathrm{grating}}$	$\mathrm{T}^{\mathrm{objective}}$	$\mathrm{QE}^{\mathrm{det}}$	$\varepsilon_{L_{TOA}}(\lambda)$ [mW/(nm*sr*m^2)]
412.5 (Oa2)	0.35	0.50	0.50	2.32
510 (Oa5)	0.30	0.60	0.60	1.52
778.75 (Oa16)	0.20	0.75	0.45	1.60

Table 6.3.1. Mean TOA radiance errors $\varepsilon_{L_{TOA}}(\lambda)$ for affected FR pixels for three different OLCI spectral bands.

At this point, an important assumption needed to be done: if a certain FR pixel is corrupted by a prompt-particle-event at frame *n*, the probability that the same across-track pixel is corrupted again before frame *n+4,* (i.e. within the next 3 x 44 ms) by another PPE may be considered null. In other words, among the four consecutive along-track FR pixels having the same across-track pixel index, just one may be considered affected. The justification of the previous assumption derives from the analysis of MERIS L0 RR data acquired during Envisat orbit 292 revealing that the same across-track pixel value was exceeding the threshold at most 4 times over 14809 frames (along-track lines) and such values were never in succession. Thus, according to the previous assumption, among the 16 FR pixels forming the RR one, at most, just 4 of them may be corrupted (maximum one per along-track line). In the most probable case, only 1 over 4x4 FR pixel may be considered affected. The reason of this may be found comparing the number of times two or more adjacent affected pixels were detected over the total number of considered samples with the estimated occurrence probability (see Chapter 3, paragraph 5).

Thus, the average of the three TOA radiance values previously retrieved (that is 1.81 mW/nm/sr/m^2) may be used as a prediction of the mean radiance created as error for OLCI L1B FR data by a single PPE.

Furthermore, using the results obtained in Chapter 3 (paragraph 3.4, page 61) about the conditional probability density function approximating the normalized histogram of L0 affected data and considering the linear relation between level 0 counts and the L1B data, the TOA radiance error $\varepsilon_L(\lambda)$ affecting corrupted FR pixels may be defined as an exponential random variable, with mean value equal to 1.81 mW/nm/sr/m^2. Thus, it may be defined a shifted conditional exponential density probability function $p(\varepsilon)$ of parameter η (equal to 1/(1.81-0.81)=1, where 0.81 is the minimum expected TOA radiance PPE-induced error), shown in Figure 6.3.2 and expressed as follows (u is the step function):

$$p(\varepsilon|corrrupt\ pixel) = \eta\ exp[-\eta\ (\varepsilon - \varepsilon_{min})]\ u(\varepsilon - \varepsilon_{min})$$

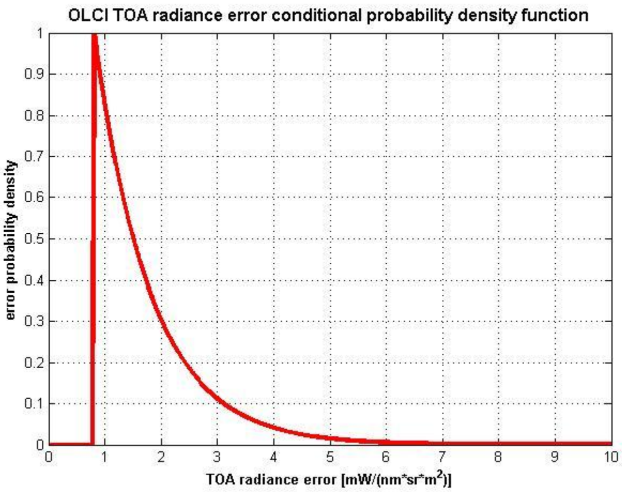

Figure 6.3.2. TOA radiance error conditional probability density functionfor Sentinel-3/OLCI.

Chapter 7 Conclusions and way forward

7.1 Summary of the study results

The thesis is providing the first time in-depth analysis of Prompt-particle-events occurring during ESA's Envisat/MERIS in-orbit observation and Sentinel-3/OLCI on-ground data. For this MERIS space observation data (Level 0 and Level 1) and OLCI ground test (raw) data were processed and analyzed. The retrieved results are provided in the various chapters of the thesis and briefly summarized in the following:

1) The analysis of MERIS dark signal acquired during Envisat's commissioning phase (see chapter 3) along one specific orbit (orbit number: 292) crossing the SAA (South-Atlantic-Anomaly) confirmed the occurrence of spikes due to PPEs striking the CCD. Inside the SAA, the occurrence probability per reduced resolution pixel was estimated to be in the order of 10^-3 for all 15 observation bands (10^-2 for the smear) while outside the SAA, for almost all MERIS bands the occurrence probability is in the order of 10^-6 (for the 13th, the 15th and the smear it is of the order of 10^-5). The smear band is in general the most affected due to its wider surface (31 elementary spectral lines binned together). As another reason the increase of the frequency (and the intensity) of the radiation on the CCD may also be induced by the presence of the aluminum layer shielding the smear band. Most of the detected spikes are in the range of 163-188 LSBs for the observation bands (the difference between the mean spike level and dark mean level is on average 19 LSBs over 12 bits of quantization) and the amplitude doesn't vary with the orbit latitude. Approximately once every ten PPE strikes, one or more consecutive RR pixels are affected along the same across-track spatial line. In order to approximate the occurrence amplitude probability density, a shifted exponential function of known parameter λ is proposed in chapter 3.

In chapter 4 a strategy to detect PPE-affected pixels in the smear signal was developed making use of MERIS L0 reduced resolution operational data of all bands over open ocean. Different data sets were compared covering a time span of seven years. The data of the 15 MERIS observation bands were processed in order to make an estimation of the smear signal that was later subtracted from the smear digital counts as recorded by the sensor and read out from the inspected file. In this chapter 4, a specific threshold is proposed (after having classified the water pixels using MERIS band number 13) in order to detect the affected water pixels. By analysis L0 data covering the time frame from 2002 until 2009, the percentage trend of PPE occurrences (in the order of 0.1%) are in line with the occurrence probability estimated in chapter 3. It is also shown that the occurrence probability is relatively stable globally and over the 7 years. Only the data set from the year 2006 retrieved slightly higher percentage of occurrences (anyways, these are known to be decorrelated with the solar cycle).

The "impact" of PPEs on a particular level 2 user product, the MERIS Maximum Chlorophyll Index (PI: Gower et al. (1999)), was investigated in chapter 5. MERIS level 1B data were processed to obtain the MCI image of seven scenes acquired over the SAA from 2003 to 2009, one per year. The thesis proposes an additional step to be included in the MCI algorithm according to which additional pixels exhibiting high MCI values may be classified as false alarms due to PPEs. These pixels may be flagged by ground processors or filtered using a 2D moving average window (or even compared with the same pixel values of previous or successive acquisitions).

In chapter 6 the number of energetic particles striking on ground per cm^2 per second was determined making use of Sentinel-3/OLCI dark signal data acquired during on-ground instrument testing. The number amounts to 1.09 PPEs per cm^2 per second, corresponding to 6.64 x 10^-9 cosmic rays per elementary CCD pixel element (22.5^2 µm^2) per 44 ms integration time. This estimate was then used in a simplified prediction model to find which could be the mean in-flight TOA radiance error measured by OLCI induced by PPEs: the impact of one PPE corresponds to about 1.81 $mW/nm/sr/m^2$ (for all OLCI spectral bands). Furthermore, for pixels affected by an energetic particle, an exponential model of probability density function for the TOA radiance error is proposed in chapter 6.

7.2 Recommendations for Sentinel-3/OLCI

In the thesis the noise contribution of PPEs retrieved from ENVISAT/MERIS *in-flight* and Sentinel-3/OLCI *on-ground* data were analyzed. Due to the fact that both instruments are flown on similar low-earth orbits and that OLCI and MERIS CCD detectors can be considered as identical in construction (the OLCI CCD55-20 is a slightly updated version of the MERIS CCD25-20) it is expected that OLCI *in-flight* performance will be affected by noise spikes caused by prompt-particle-events (PPEs). The effect will occur in both modes, Earth Observation and Calibration modes and is provided as part of the thesis, i.e., in chapter 3 for the PPE occurrence probability and in chapter 5 for the impact of a single PPE in terms of TOA radiance.

a) Effect on OLCI data

The estimation of the occurrence probability of affected FR pixels depends on the particular latitude and longitude that the instrument observes. Outside the South Atlantic Anomaly (SAA), the probability is usually in the order of 10^-6 for all those observation bands composed by less than 16 spectral lines and far from the aluminum shield; for the spectral band Oa17 (where 16 spectral lines are spectrally binned together), Oa21 (far 720 µm from the adjacent shielded smear band) and the smear band, the occurrence probability may reach the order of 10^-5. In the South Atlantic Anomaly (SAA) the occurrence probability may vary in the order of 10^-3 for all observation bands, reaching 10^-2 in the case of the smear band. Furthermore, the presence of two or more consecutive affected pixels caused by a single PPE along the same across-track line was observed in more than one MERIS band: this event approximately occurred with a frequency of 10^-7 and may affect OLCI in the same order of magnitude.

Due to the linear relation between level 0 and level 1B data, the top-of-the-atmosphere radiance error for OLCI affected pixels may be characterized as a random shifted exponential variable of parameter η=1/(1.81-0.81)=1 and mean value equal to 1.81 mW/(nm*se*m^2).

Even if the effect of high energy particles striking on the CCD may be considered to a first approximation irrelevant (at least outside the SAA) for level 0 and level 1B OLCI products, it could be a cause of corrupted values by retrieving level 2 scientific products, as it was demonstrated for the case of Maximum Chlorophyll Index (MCI) images (see chapter 5). Thus, the influence on L2 products needs to be addressed in more detail.

b) Further Level 2 product assessment using simulated data set

It is proposed to perform a further analysis making use of the results reported above. For this a specific simulated data set would be needed to be simulated: first, two identical L1B top-of-the-atmosphere radiance datasets (a cube of 21 bands composed of N pixels per dataset in full resolution with different ground target (e.g., clouds, ocean, land)) are created. Then, one of the two datasets is “artificial” degraded with noise injected according to the following strategy:

- pixels are degraded with a probability in the order of 10^-6 (10^-3 if simulating an SAA scenario): thus, having every pixel its identification index number, from 0 to N-1 and using a random uniform variable generator, the affected pixels may be identified;
- among these degraded pixels, in the percentage of ten percent, some will be followed (on the right, on the left or both) by one or more (up to a total of 9) corrupted FR pixels along the same across-track spatial line (the number among 1 to 10 may be chosen using a uniform random variable generator);
- each corrupted sample should exceed the correct one by a random quantity generated according to the above mentioned shifted exponential probability density of parameter η=1, with mean value equal to 1.81 mW/(nm*se*m^2) and minimum value equal to 0.81 mW/(nm*se*m^2).

In this way, two L1B top-of-the-atmosphere radiance datasets are created, one with and the other without the influence PPSs. Thereinafter, L2 algorithms and there retrieved products can be assessed after comparing the processed correct L1B data with the corresponding equally processed corrupt L1B data.

c) Potential mitigation strategy

In order to mitigate the influence of PPE-affected pixels with unexpected high value, those pixels can be flagged in level 1 processing and these flags can be used on level 2.

In any case, two main strategies of potential mitigation via ground processing were identified whenever a corrupt pixel is detected. First, the affected pixel may be compared with surrounding pixels and its value may be substituted by a 2-dimensional moving average filtering of the adjacent values (as for the case of false alarms in MCI images). Second, the pixel value under question may be compared with the same pixel value acquired by OLCI in a different (previous or next) temporal acquisition.

The same algorithms used to detect the occurrences in MERIS level 0 data may be used to monitor the occurrence of PPEs affecting OLCI CCDs during Sentinel-3 commissioning phase and during nominal space operations. One additional way to monitor the occurrences of PPEs and their impact on the signal at the VEU (Video Electronic Unit) output may be obtained checking the behavior of the blank pixels, i.e. those shielded pixels located at the sides of the imaging zone of the CCD.

Appendix A

The histograms of the Level 0 data sets analyzed in Chapter 4 are plotted in Figures A.1-A.6. The data sets refer to six swaths all located in the South Atlantic Anomaly and acquired by MERIS from 2003 to 2008 in different months at the same time (the order in which the figures appear starts from 2008 down to 2003).

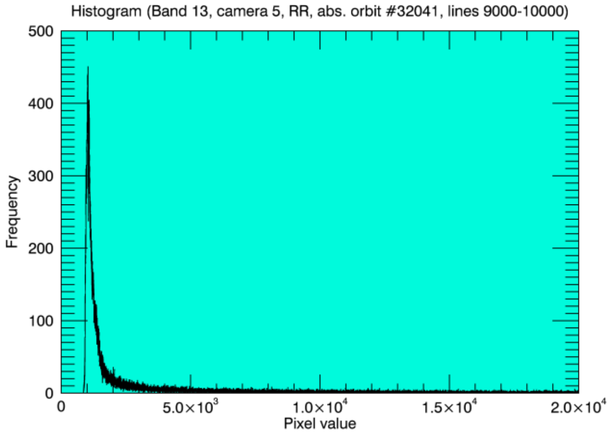

Figure A.1. MERIS level 0 data histogram
(band 13, camera 5, orbit 32041, AT lines 9000-10000).

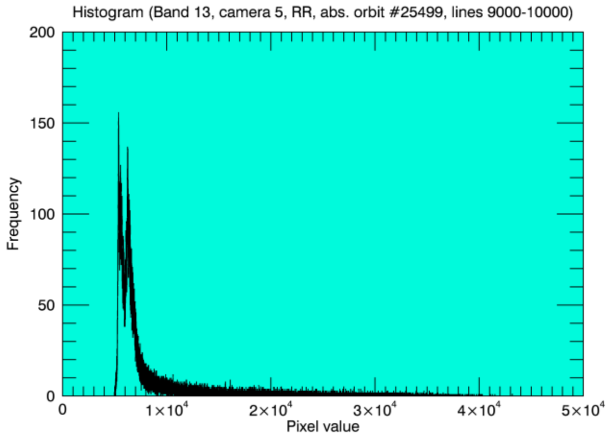

Figure A.2. MERIS level 0 data histogram
(band 13, camera 5, orbit 25499, AT lines 9000-10000).

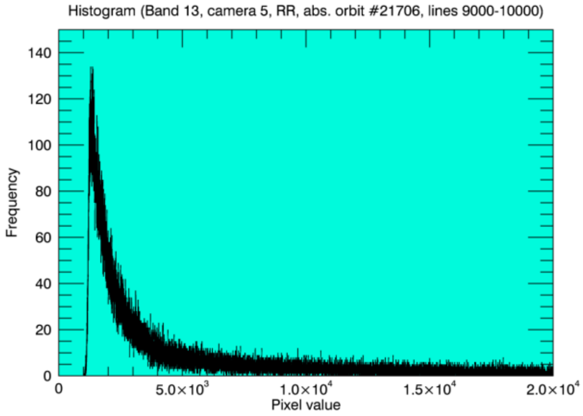

Figure A.3. MERIS level 0 data histogram
(band 13, camera 5, orbit 21706, AT lines 9000-10000).

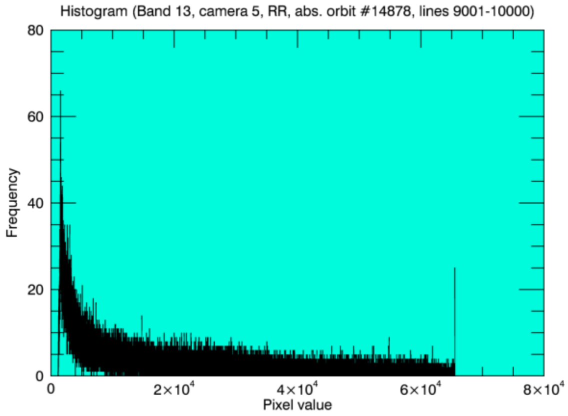

Figure A.4. MERIS level 0 data histogram
(band 13, camera 5, orbit 14878, AT lines 9000-10000).

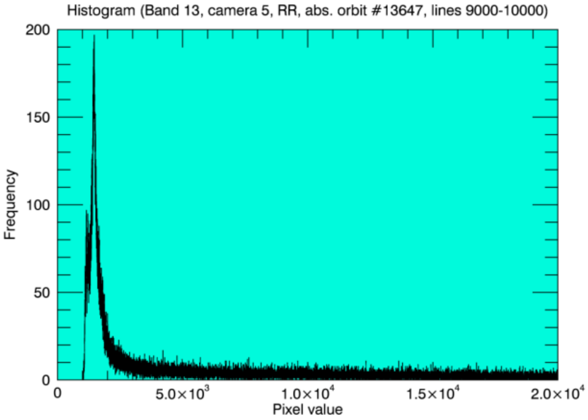

Figure A.5. MERIS level 0 data histogram
(band 13, camera 5, orbit 13647, AT lines 9000-10000).

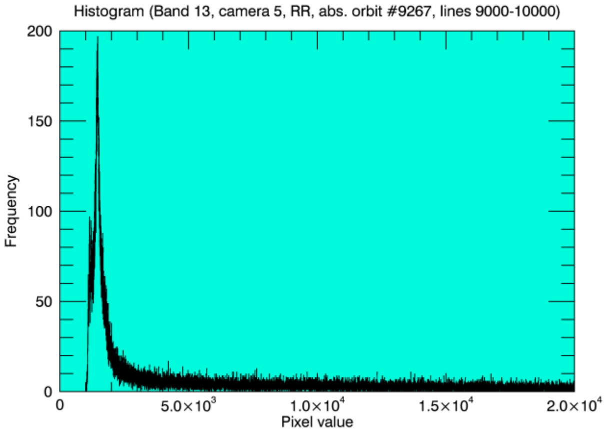

Figure A.6. MERIS level 0 data histogram
(band 13, camera 5, orbit 9267, AT lines 9000-10000).

Appendix B

Following the AIT (Assembly Integration Test) test conditions are described per each camera module and the main results of the analysis of PPE-induced noise are shown in Tables B.1-B.41. Per each camera (except for camera 1) three different gain values were applied (G0, G4 and G7, see Table 6.1.1). The test took place in Thales Alenia Space, Cannes (France) in 2013 and 2014.

- *<u>Camera 1</u>*

The camera 1 is composed of the COSA PFM equipped with the FPA PFM, coupled to the VAM FM2.

The test was performed on 10/04/2013 with the following conditions [31]:

- Ambient pressure;
- CCD temperature regulated at +17°C (above dew point);
- VAM temperature was neither regulated nor monitored;
- medium and maximum gains: G4 and G7 for each microband;
- nominal configuration of bands and microbands;
- Sampling Interval parameters as used in “Test 7” according to RD-11;
- Offset Compensation Loop has been operated as expected in flight conditions

  - *Camera 1, Gain 4*

The following acquisition file was analyzed:

- *Adressing_G4_acq_20130712134730.cuo*

The main results of the analysis are shown in Tables B.1-B.3.

Dark signal main statistics (Camera 1, Gain 4)				
Dark Measurements Mean LSB Value (DMV)	Dark Measurements Standard Deviation	Occurrence Max LSB Value	Occurrence Mean LSB Value (OMV)	OMV-DMV
39.2	1.4	139	72	32.8

Table B.1. Main statistics of dark samples and occurrences during OLCI on ground dark tests (camera 1, gain 4).

Occurrences (Camera 1, Gain 4)		
Number of detected occurrences	Number of considered samples	Probability of occurrence
8	33930000	2.4*10^-7

Table B.2. Percentage of occurrences during OLCI on ground dark tests (camera 1, gain 4).

Affected pixels (Camera 1, Gain 4)		
Spatial pixel number	Microband number	Frame number
1	1	1
4	3	502
53	8	880
69	13	140
225	20	642
363	21	801
704	25	636
284	37	833

Table B.3. Affected pixels during OLCI on ground dark tests (camera 1, gain 4).

- *Camera 1, Gain 7*

The following acquisition file was analyzed:

- Adressing_G7_acq_20130712135055.cuo

The main results of the analysis are shown in Tables B.4-B.6.

Dark signal main statistics (Camera 1, Gain 7)				
Dark Measurements Mean LSB Value (DMV)	Dark Measurements Standard Deviation	Occurrence Max LSB Value	Occurrence Mean LSB Value (OMV)	OMV-DMV
38.9	2.2	312	91.1	52.2

Table B.4. Main statistics of dark samples and occurrences during OLCI on ground dark tests (camera 1, gain 7).

Occurrences (Camera 1, Gain 7)		
Number of detected occurrences	Number of considered samples	Probability of occurrence
18	33930000	5.9*10^-7

Table B.5. Percentage of occurrences during OLCI on ground dark tests (camera 1, gain 7).

Affected pixels (Camera 1, Gain 7)		
Spatial pixel number	Microband number	Frame number
1	4	1
1	5	1
1	6	1
1	7	1
185	10	521
186	10	521
424	15	36
264	16	48
12	19	504
13	19	139
478	22	139
256	25	139
695	29	985
564	36	307
701	41	295
702	41	307
665	45	307
666	45	406

Table B.6. Affected pixels during OLCI on ground dark tests (camera 1, gain 7).

- ***Camera 2***

The camera 2 is composed of the COSA FM2 equipped with the FPA FM2, coupled to the VAM FM2.

The test was performed on 10/04/2013 with the following conditions [32]:

- Ambient pressure;
- CCD temperature regulated at +17°C (above dew point);
- VAM temperature was neither regulated nor monitored;
- Minimum, medium and maximum gains: G0, G4 and G7 for each microband;

- nominal configuration of bands and microbands;
- Sampling Interval parameters as used in “Test 7” according to RD-11;
- Offset Compensation Loop has been operated as expected in flight conditions

- *Camera 2, Gain 0*

The following acquisition file was analyzed:

- *Dsm_G0_Adressing_acq_20130410171526.cuo*

The main results of the analysis are shown in Tables B.7-B.9.

Dark signal main statistics (Camera 2, Gain 0)				
Dark Measurements Mean LSB Value (DMV)	Dark Measurements Standard Deviation	Occurrence Max LSB Value	Occurrence Mean LSB Value (OMV)	OMV-DMV
39.6	0.8	72	55.3	15.7

Table B.7. Main statistics of dark samples and occurrences during

OLCI on ground dark tests (camera 2, gain 0).

Occurrences (Camera 2, Gain 0)		
Number of detected occurrences	Number of considered samples	Probability of occurrence
6	33930000	1.8*10^-7

Table B.8. Percentage of occurrences during OLCI on ground dark tests (camera 2, gain 0).

Affected pixels (Camera 2, Gain 0)		
Spatial pixel number	Microband number	Frame number
581	2	339
503	9	171
504	9	171
669	11	711
678	16	89
609	35	39

Table B.9. Affected pixels during OLCI on ground dark tests (camera 2, gain 0).

- *Camera 2, Gain 4*

The following acquisition file was analyzed:

- *Dsm_G4_Adressing_acq_20130410171846.cuo*

The main results of the analysis are shown in Tables B.10-B.12.

Dark signal main statistics (Camera 2, Gain 4)				
Dark Measurements Mean LSB Value (DMV)	Dark Measurements Standard Deviation	Occurrence Max LSB Value	Occurrence Mean LSB Value (OMV)	OMV-DMV
39.6	1.3	75	61.7	22.1

Table B.10. Main statistics of dark samples and occurrences during OLCI on ground dark tests (camera 2, gain 4).

Occurrences (Camera 2, Gain 4)		
Number of detected occurrences	Number of considered samples	Probability of occurrence
9	33930000	2.7*10^-7

Table B.11. Percentage of occurrences during OLCI on ground dark tests (camera 2, gain 4).

Affected pixels (Camera 2, Gain 4)		
Spatial pixel number	Microband number	Frame number
85	2	977
188	3	86
342	7	132
316	7	200
405	8	200
406	8	200
698	17	218
354	38	127
353	41	654

Table B.12. Affected pixels during OLCI on ground dark tests (camera 2, gain 4).

- *Camera 2, Gain 7*

The following acquisition file was analyzed:

- *Dsm_G7_Adressing_acq_20130410172539.cuo*

The main results of the analysis are shown in Tables B.13-B.15.

Dark signal main statistics (Camera 2, Gain 7)				
Dark Measurements Mean LSB Value (DMV)	Dark Measurements Standard Deviation	Occurrence Max LSB Value	Occurrence Mean LSB Value (OMV)	OMV-DMV
37.8	2.1	347	103.8	66.0

Table B.13. Main statistics of dark samples and occurrences during

OLCI on ground dark tests (camera 2, gain 7).

Occurrences (Camera 2, Gain 7)		
Number of detected occurrences	Number of considered samples	Probability of occurrence
14	33930000	4.1*10^-7

Table B.14. Percentage of occurrences during OLCI on ground dark tests (camera 2, gain 7).

Affected pixels (Camera 2, Gain 7)		
Spatial pixel number	Microband number	Frame number
85	2	977
188	3	86
342	7	132
316	7	200
405	8	200
406	8	200
698	17	218
354	38	127
353	41	654

Table B.15. Affected pixels during OLCI on ground dark tests (camera 2, gain 7).

- ***Camera 3***

The camera 3 is composed of the COSA FM3 equipped with the FPA FM3, coupled to the VAM PFM (before its refurbishment).

The test was performed on 01/03/2013 with the following conditions [33]:

- Ambient pressure;
- CCD temperature regulated at +17°C (above dew point);
- VAM temperature was neither regulated nor monitored;
- Minimum, medium and maximum gains: G0, G4 and G7 for each microband;
- nominal configuration of bands and microbands;
- Sampling Interval parameters as used in “Test 7” according to RD-11;
- Offset Compensation Loop has been operated as expected in flight conditions

○ *Camera 3, Gain 0*

The following acquisition file was analyzed:

- *Adressing_G0_acq_20130301073247.cuo*

The main results of the analysis are shown in Tables B.16-B.17.

Dark signal main statistics (Camera 3, Gain 0)			
Dark Measurements Mean LSB Value (DMV)	Dark Measurements Standard Deviation	Occurrence Max LSB Value	Occurrence Mean LSB Value (OMV)
38.3	2.1	-	-

Table B.16. Main statistics of dark samples and occurrences during OLCI on ground dark tests (camera 3, gain 0).

Occurrences (Camera 3, Gain 0)		
Number of detected occurrences	Number of considered samples	Probability of occurrence
0	33930000	0.0

Table B.17. Percentage of occurrences during OLCI on ground dark tests (camera 3, gain 0).

- *Camera 3, Gain 4*

The following acquisition file was analyzed:

- *Adressing_G4_acq_20130301073606.cuo*

The main results of the analysis are shown in Tables B.18-B.20.

Dark signal main statistics (Camera 3, Gain 4)				
Dark Measurements Mean LSB Value (DMV)	Dark Measurements Standard Deviation	Occurrence Max LSB Value	Occurrence Mean LSB Value (OMV)	OMV-DMV
37.9	2.2	107	64.4	26.5

Table B.18. Main statistics of dark samples and occurrences during OLCI on ground dark tests (camera 3, gain 4).

Occurrences (Camera 3, Gain 4)		
Number of detected occurrences	Number of considered samples	Probability of occurrence
7	33930000	2.1*10^-7

Table B.19. Percentage of occurrences during OLCI on ground dark tests (camera 3, gain 4).

Affected pixels (Camera 3, Gain 4)		
Spatial pixel number	Microband number	Frame number
37	10	39
309	19	398
522	24	324
498	25	324
97	27	444
391	34	483
210	37	793

Table B.20. Affected pixels during OLCI on ground dark tests (camera 3, gain 4).

- *Camera 3, Gain 7*

The following acquisition file was analyzed:

- *Adressing_G7_acq_20130301073941.cuo*

The main results of the analysis are shown in Tables B.21-B.23.

Dark signal main statistics (Camera 3, Gain 7)				
Dark Measurements Mean LSB Value (DMV)	Dark Measurements Standard Deviation	Occurrence Max LSB Value	Occurrence Mean LSB Value (OMV)	OMV-DMV
37.7	2.6	272	92.2	54.5

Table B.21. Main statistics of dark samples and occurrences during OLCI on ground dark tests (camera 3, gain 7).

Occurrences (Camera 3, Gain 7)		
Number of detected occurrences	Number of considered samples	Probability of occurrence
23	33930000	6.8*10^-7

Table B.22. Percentage of occurrences during OLCI on ground dark tests (camera 3, gain 7).

Affected pixels (Camera 3, Gain 7)		
Spatial pixel number	Microband number	Frame number
9	3	835
63	3	940
64	3	940
65	3	940
97	5	400
98	5	400
99	5	400
113	5	400
572	5	710
113	6	400
114	6	400
122	6	400
734	7	804
271	9	271
272	9	271
566	20	447
567	20	447
488	33	527
132	36	520
133	36	520
616	36	877
617	36	877
619	36	877

Table B.23. Affected pixels during OLCI on ground dark tests (camera 3, gain 7).

- ***<u>Camera 4</u>***

The camera 4 is composed of the COSA FM4 equipped with the FPA FM4, coupled to the VAM FM2.

The test was performed on 27/06/2013 with the following conditions [34]:

- Vacuum pressure ;

- CCD temperature regulated at -22.5°C ;
- VAM temperature regulated at +10°C;
- Minimum, medium and maximum gains: G0, G4 and G7 for each microband;
- nominal configuration of bands and microbands;
- Sampling Interval parameters as used in “Test 7” according to RD-11;
- Offset Compensation Loop has been operated as expected in flight conditions

- *Camera 4, Gain 0*

The following acquisition file was analyzed:

- *Dsm_G0_Adressing_acq_20130627101035.cuo*

The main results of the analysis are shown in Tables B.24-B.26.

Dark signal main statistics (Camera 4, Gain 0)				
Dark Measurements Mean LSB Value (DMV)	Dark Measurements Standard Deviation	Occurrence Max LSB Value	Occurrence Mean LSB Value (OMV)	OMV-DMV
39.1	1.3	56	49.8	10.7

Table B.24. Main statistics of dark samples and occurrences during OLCI on ground dark tests (camera 4, gain 0).

Occurrences (Camera 4, Gain 0)		
Number of detected occurrences	Number of considered samples	Probability of occurrence
8	33930000	2.4*10^-7

Table B.25. Percentage of occurrences during OLCI on ground dark tests (camera 4, gain 0).

Affected pixels (Camera 4, Gain 0)		
Spatial pixel number	Microband number	Frame number
107	5	525
108	5	525
645	12	450
626	14	413
627	14	413
306	17	450
745	22	247
745	29	580

Table B.26. Affected pixels during OLCI on ground dark tests (camera 4, gain 0).

- *Camera 4, Gain 4*

The following acquisition file was analyzed:

- *Dsm_G4_Adressing_acq_20130627101456.cuo*

The main results of the analysis are shown in Tables B.27-B.29.

Dark signal main statistics (Camera 4, Gain 4)				
Dark Measurements Mean LSB Value (DMV)	Dark Measurements Standard Deviation	Occurrence Max LSB Value	Occurrence Mean LSB Value (OMV)	OMV-DMV
38.8	1.8	129	74.6	35.8

Table B.27. Main statistics of dark samples and occurrences during OLCI on ground dark tests (camera 4, gain 4).

Occurrences (Camera 4, Gain 4)		
Number of detected occurrences	Number of considered samples	Probability of occurrence
5	33930000	1.5*10^-7

Table B.28. Percentage of occurrences during OLCI on ground dark tests (camera 4, gain 4).

Affected pixels, (Camera 4, Gain 4)		
Spatial pixel number	Microband number	Frame number
225	8	470
226	8	470
179	23	909
13	28	560
428	38	521

Table B.29. Affected pixels during OLCI on ground dark tests (camera 4, gain 4).

- *Camera 4, Gain 7*

The following acquisition file was analyzed:

- *Dsm_G7_Adressing_acq_20130627101919.cuo*

The main results of the analysis are shown in Tables *B.30-B.32*.

Dark signal main statistics (Camera 4, Gain 7)				
Dark Measurements Mean LSB Value (DMV)	Dark Measurements Standard Deviation	Occurrence Max LSB Value	Occurrence Mean LSB Value (OMV)	OMV-DMV
38.6	2.3	179	84.7	46.1

Table B.30. Main statistics of dark samples and occurrences during

OLCI on ground dark tests (camera 4, gain 7).

Occurrences (Camera 4, Gain 7)		
Number of detected occurrences	Number of considered samples	Probability of occurrence
14	33930000	4.1*10^-7

Table B.31. Percentage of occurrences during OLCI on ground dark tests

(camera 4, gain 7).

Affected pixels (Camera 4, Gain 7)		
Spatial pixel number	Microband number	Frame number
393	2	98
394	2	98
396	2	98
397	2	98
311	3	572
312	3	572
62	3	780
380	24	630
379	25	630
380	25	630
14	34	474
15	34	474
28	36	474
720	37	745

Table B.32. Affected pixels during OLCI on ground dark tests (camera 4, gain 7).

- ***Camera 5***

The camera 5 is composed of the COSA FM4 equipped with the FPA FM4, coupled to the VAM FM2.

The test was performed on 24/08/2013 with the following conditions [35]:

- Vacuum pressure ;
- CCD temperature regulated at -22.5°C ;
- VAM temperature regulated at +10°C;
- Minimum, medium and maximum gains: G0, G4 and G7 for each microband;
- nominal configuration of bands and microbands;
- Sampling Interval parameters as used in "Test 7" according to RD-11;
- Offset Compensation Loop has been operated as expected in flight conditions

- *Camera 5, Gain 0*

The following acquisition file was analyzed:

- *Adressing_G0_acq_20130824162219.cuo*

The main results of the analysis are shown in Tables *B.33-B.35*.

Dark signal main statistics (Camera 5, Gain 0)				
Dark Measurements Mean LSB Value (DMV)	Dark Measurements Standard Deviation	Occurrence Max LSB Value	Occurrence Mean LSB Value (OMV)	OMV-DMV
39.9	1.1	81	54.3	14.4

Table B.33. Main statistics of dark samples and occurrences during OLCI on ground dark tests (camera 5, gain 0).

Occurrences (Camera 5, Gain 0)		
Number of detected occurrences	Number of considered samples	Probability of occurrence
6	33930000	1.8*10^-7

Table B.34. Percentage of occurrences during OLCI on ground dark tests (camera 5, gain 0).

Affected pixels (Camera 5, Gain 0)		
Spatial pixel number	Microband number	Frame number
574	4	781
87	4	985
88	4	985
85	6	985
94	20	256
706	27	738

Table B.35. Affected pixels during OLCI on ground dark tests (camera 5, gain 0).

- *Camera 5, Gain 4*

The following acquisition file was analyzed:

- *Adressing_G4_acq_20130824162504.cuo*

The main results of the analysis are shown in Tables *B.36-B.38*.

Dark signal main statistics (Camera 5, Gain 4)				
Dark Measurements Mean LSB Value (DMV)	Dark Measurements Standard Deviation	Occurrence Max LSB Value	Occurrence Mean LSB Value (OMV)	OMV-DMV
39.7	1.3	80	51.8	12.1

Table B.36. Main statistics of dark samples and occurrences during OLCI on ground dark tests (camera 5, gain 4).

Occurrences (Camera 5, Gain 4)		
Number of detected occurrences	Number of considered samples	Probability of occurrence
5	33930000	1.5*10^-7

Table B.37. Percentage of occurrences during OLCI on ground dark tests (camera 5, gain 4).

Affected pixels (Camera 5, Gain 4)		
Spatial pixel number	Microband number	Frame number
309	2	905
680	4	776
14	10	255
89	12	34
250	33	560

Table B.38. Affected pixels during OLCI on ground dark tests (camera 5, gain 4).

- *Camera 5, Gain 7*

The following acquisition file was analyzed:

- *Adressing_G7_acq_20130824162731.cuo Gain G7*

The main results of the analysis are shown in Tables *B.39-B.41*

Dark signal main statistics (Camera 5, Gain 7)				
Dark Measurements Mean LSB Value (DMV)	Dark Measurements Standard Deviation	Occurrence Max LSB Value	Occurrence Mean LSB Value (OMV)	OMV-DMV
39.6	1.7	153	76.7	37.1

Table B.39. Main statistics of dark samples and occurrences during

OLCI on ground dark tests (camera 5, gain 7).

Occurrences (Camera 5, Gain 7)		
Number of detected occurrences	Number of considered samples	Probability of occurrence
15	33930000	4.4*10^-7

Table B.40. Percentage of occurrences during OLCI on ground dark tests (camera 5, gain 7).

Affected pixels (Camera 5, Gain 7)		
Spatial pixel number	Microband number	Frame number
408	2	797
426	1	658
51	16	365
52	16	365
48	17	365
49	17	365
50	17	365
277	24	426
378	25	658
36	33	538
37	33	538
139	33	759
550	34	41
550	35	41
524	38	201

Table B.41. Affected pixels during OLCI on ground dark tests (camera 5, gain 7).

References

1. J.R. Janesick, *“Scientific Charge-Coupled Devices” SPIE Press Monograph Vol. PM83,* 2001.

2. M. Dobber, R. Dirksen, P. Levelt, B. van den Oord, R. Voors, Q. Kleipool, *“EOS-Aura Ozone Monitoring Instrument: Scientific Results Of Nearly Two Years Successful Operation And In-Flight Calibration And Performance”,* 2006.

3. M. Rast, J.L. Bezy, S. Bruzzi, *“The ESA Medium Resolution Imaging Spectrometer MERIS – a review of the instrument and its mission”,* 1999.

4. J.Gower, Stephanie King and Pedro Gonçalves., *“A Global Survey Of Intense Surface Plankton Blooms And Floating Vegetation Using MERIS MCI”,* 2007.

5. R. Sanchez-Labrador et al., *“Sentinel-3, OLCI Detection Chain EM Noise Spikes, IN-16”*, 2012.

6. J.R. Heirtzler, *“The future of the South Atlantic anomaly and implications for radiation damage in space”, Journal of Atmospheric and Solar-Terrestrial Physics, Vol. 64.* 2002.

7. *https://directory.eoportal.org/web/eoportal/satellite-missions/content/-/article/nanosatc-br1, 20/03/2014.*

8. J. Gower, S.King, G. Borstad, L. Brown, "*Detection of intense plankton blooms using the MERIS optical imager on Envisat",* 2004.

9. P.A. Dubock et al. , *“The Envisat Satellite and Its Integration, ESA Bulletin 106”,* 2001.

10. B.Berruti et al., "*The Copernicus Sentinel-3 Mission and Oceanography: Overview and current status",* 2014.

11. www.copernicus.eu, 01/01/2014.

12. J.-L. Bézy et al.., *"MERIS, the ocean colour instrument on board ENVISAT",* 2013.

13. J. Nieke, C. Mavrocordatos, C. Donlon, B. Berruti, "*The Sentinel-3 Ocean and Land Colour Imager",* 2015.

14. M.A.Cutter, P.Pool, D.Burt, "*Development of a back thinned CCD for the Medium Resolution Imaging Spectrometer",* Image sensors Workshop*,* 1993

15. G. Levrini, E. Attema, *"The Commissioning Phase and the Calibration/Validation Activities", ESA bullettin 106,* 2001.

16. G. R. Hopkinson, T.M. Goodman, S. R. Prince, "*A Guide to the Use and Calibration of Detector Array Equipment", SPIE Press Monograph Vol. PM142,* 2004.

17. J.L. Bezy, "*Addendum to the Characterization Data Base", PO-TN-ESA_ME_01029v1,* 2000.

18. L. Bourg, S.Delwart, *MERIS instrument calibration",* 2006.

19. J. Nieke, M.Solbrig, A. Neumann, "*Noise contribution for imaging spectrometers",* 1999.

20. R. Doerffer et al.,"*Atmosphere and Glint Correction Processor",* 2010.

21. M. Cardacci, L.Bourg, "*Envisat-1 Product Specifications" (Vol. 11),* 2011.

22. M. Cardacci, L.Bourg, "*Envisat-1 Product Specification" (Vol. 6),* 2011.

23. C.Binding et al., "*Monitoring algal blooms using the MERIS Maxmum Chlorophyll Index",* 2012.

24. *www.brockmann-consult.de/beam/doc/help/flh_mci/FlhMciAlgorithmSpecification.html, 30/01/2014.*

25. J. Gower, S.King, "*New results from a global survey using MERIS MCI",* 2008.

26. J.Gower et al., "*Global monitoring of plankton blooms using MERIS MCI",* 2008.

27. *http://www.brockmann-consult.de/cms/web/beam/, 15/01/2014.*

28. W. E. Esaias et al., "*An overview of MODIS capabilities for ocean science observations", IEEE Transactions on Geoscience and Remote Sensing, 36, 1250-1265,* 1998.

29. J. E. O'Really et al., "*SeaWiFS Postlaunch Calibration and Validation Analyses", Part 3,* 2000.

30. *http://modis.gsfc.nasa.gov/about/specifications.php, 15/04/2014.*

31. R.Sanchez-Labrador, "*Sentinel-3-OLCi analysis of the Dark Signal test of Camera PFM + VAM FM2", S3-TN-TAF-OL-02651, Thales Alenia Space,* 2013.

32. R.Sanchez-Labrador, "*Sentinel-3-OLCI: analysis of dark signal test of camera FM2", S3-TN-TAF-OL-02539, Thales Alenia Space,* 2014.

33. R.Sanchez-Labrador, "*Sentinel-3-OLCI Analysis of the Initial Dark Signal Test of Camera FM3 + VAM PFM", S3-TN-TAF-OL-02662, Thales Alenia Space,* 2014.

34. R.Sanchez-Labrador, *Sentinel-3-OLCI Analysis of Dark Signal test of Camera FM4 + VAM FM2 in flight conditions, S3-TN-TAF-OL-02764, Thales Alenia Space,* 2014.

35. R.Sanchez-Labrador, "*Sentinel-3-OLCI Analysis of the Camera FM5 + VAM Dark Signal test of FM3 in flight conditions", S3-TN-TAF-OL-02830, Thales Alenia Space,* 2014.

36. J.B. Riti, "*Sentinel 3 OLCI Measurement Data Definition document", S3-DD-TAF-OL-00836, Thales Alenia Space,* 2014.

37. T. Garnier, "*OLCI PFM Instrument: analysis of radiometric accuracy test", S3-TN-TAF-OL-02965, Thales Alenia Space,* 2014.

Acknowledgments

I would like to express my gratitude to my supervisors Prof. G.Corsini (University of Pisa), Prof. M.Diani (University of Pisa) and J.Nieke (ESA/ESTEC) for having supported me during my thesis work.

My sincere thanks also goes to L. Bourg (ACRI) and P.Goryl (ESA/ESRIN) for having made easily available Envisat/MERIS Level 0 data, J.L. Bezy (ESA/ESTEC) for its technical support in the analysis of MERIS data, J.B. Riti, T. Garnier, R. Sánchez-Labrador (Thales Alenia Space, France, Cannes) for providing Sentinel-3/OLCI AIT data and J.Gower (Institute of Ocean Science, Canada) for our opinion exchange about false alarms in MCI images.

Last, but not the least, a special thank goes to the Sentinel-3 team for having given to me the opportunity to be part of their team during seven intense months.